



FACULDADE DE
CIÊNCIAS E TECNOLOGIA
UNIVERSIDADE NOVA DE LISBOA

DEPARTAMENTO DE FÍSICA

Sensitivity correction of images obtained with the prototype Clear-PEM in pre-clinical environment

Ana Cristina da Fonseca Teixeira

Dissertation presented at *Faculdade de Ciências e Tecnologia
Universidade Nova de Lisboa* to obtain a Master Degree in Biomedical
Engineering

Advisors: Professor Dr. Pedro Almeida
Professor Dr. Nuno Matela

Lisboa
2009

To my parents and my grandparents.

Acknowledgments

This work was carried out at *Instituto de Biofísica e Engenharia Biomédica da Faculdade de Ciências da Universidade de Lisboa* (IBEB). I would like to express my sincere gratitude to those who have supported me and contributed to this thesis.

First and foremost, I would like to thank my advisor, Professor Pedro Almeida, for the opportunity he gave me to choose my own work and join his Molecular Imaging research group, despite being a student at a different university.

I would also like to make a special reference to my other advisor, Professor Nuno Matela. Thank you, not only for your constant assistance and guidance in this study but also for all the support, patience and friendship! It has been great working with you.

To Nuno Oliveira, I would like to show my gratitude for all the work developed in the creation and maintenance of Quasimanager, for it sure made my work a lot easier.

For the most cheering and enthusiastic person at IBEb, Professor Ducla-Soares, I want to thank for all the encouragement and kind words. You make us all want to “grow up” to be like you.

To all my colleagues and friends at IBEb, for all the laughter and the good times at our “i-events”, but also for the help, the advice and the encouraging, a huge thank you. Especially to Pedro, my editor, for all your kind words of friendship and support; to Miguel, even with all the kicking under the table, it was great working with you on this adventure outside “their” FCT; to Liliana, your strength and will to keep everything moving forward is unbelievable, thank you for your inspiration. But also to Ricardo, Henrique, Beatriz, and everybody else at IBEb.

Considering that this work was the end of a cycle, I would really like to mention my truest friends, who kept me going in this last five years, even during some hard times... A big thank you to Kiko, Joana, Miguel Abreu, Ana Patrícia, João and Miguel Gonçalves, for your friendship and for everything we have been through, together!

To João, first for convincing me to go on that long, crazy trip and letting me get to know you, and now for your friendship and for all the late hours you kept me company, when everybody else was already asleep.

To Inês, my sister, my beloved best friend who has been there for me for all these years, cheering me up and giving me strength to carry on. Thank you for all the good times (and after 18 years, there are a lot) for all your friendship and all your love.

Also to our Gang: girls, thank you for being there, even after all these years.

I would also like to thank the most important people in my life: my parents. For everything you have ever done for me, for all your love, all the support and encouragement and for teaching me to always have a thirst for knowledge: Thank you!

To my grandparents, Maria e António, I want to thank for always believing in me and putting me first, and for your unconditional love.

Last, but definitely not least, to Kiko. For all the unnecessary worrying, the friendship, the company, the talks, the love... You are truly my best friend, and for that I thank you!

To everybody who was involved with this work, directly or not, and made it possible: Thank you!

Abstract

Nuclear medicine has, when compared to anatomical imaging techniques, the great advantage of identifying the metabolic activity of the cells, hence becoming a great option for tumour identification.

A new technology in this area is Positron Emission Mammography (PEM) that follows the same physical basics of Positron Emission Tomography (PET). The Clear-PEM project, a Portuguese research project, uses this technology and, in alternative to the whole-body exam, only the breast is examined, using two detector plates that rotate around the breast to detect radiation. The prototype has the ability to perform a complementary exam of the axillary region. This scanner is designed to detect small lesions or tumours in early stages, with high resolution and high sensitivity.

After the acquisition, the data undergoes a process of reconstruction and corrections. It is our job to study which parameters should be adjusted in order to get the best contrast between lesions and the breast background, as well as meeting the high resolution standards we set to achieve.

This work consisted in the correction of some characteristics that might influence image quality. The first correction made was the elimination of the presence of the gaps between the detector crystals' effects, resulting in the enhancement of the image Signal-to-Noise Ratio (SNR).

By varying the energy window of the image acquisitions, it was possible to minimize the effect of scattered photons, and varying the timing window minimized the effect of random coincidences.

Keywords: Positron Emission Mammography (PEM); Sensitivity correction; Random correction; Scattered correction.

Resumo

A medicina nuclear tem, sobre as técnicas de imagem anatómica, a grande vantagem de mostrar a actividade metabólica das células, característica esta que é uma mais-valia para a identificação de tumores.

Uma nova tecnologia nesta área é a Mamografia por Emissão de Positrões, que segue os princípios físicos de um exame de Tomografia por Emissão de Positrões. O projecto Clear-PEM, fruto de investigação portuguesa, adopta esta tecnologia e, em alternativa ao exame de corpo inteiro, efectua um exame apenas à mama, recorrendo a dois detectores planares, que rodam em torno da mesma. O protótipo tem também a possibilidade de fazer exames à axila. Pretende-se que, em ambiente clínico, venha a apresentar uma alta resolução, alta sensibilidade e que seja capaz de detectar pequenas lesões e tumores em baixos estágios de desenvolvimento.

Após a aquisição, os dados terão de ser reconstruídos e corrigidos para que se obtenha uma imagem. Este trabalho consiste em estudar quais as características a ajustar de forma a conseguir o melhor contraste entre possíveis lesões e o fundo da mama, bem como garantir que vamos de encontro aos padrões de alta resolução propostos.

O trabalho consistiu na correcção de vários parâmetros que influenciam a qualidade da imagem obtida. A primeira correcção efectuada foi a eliminação de artefactos resultantes da presença de *gaps* entre os cristais, resultando numa melhoria da Razão Sinal-Ruído da imagem.

Fazendo variar a janela de energia da aquisição das imagens, foi possível minimizar o efeito dos fotões Compton, e fazendo variar a janela de tempo minimizou-se o efeito de coincidências aleatórias.

Palavras-chave: Mamografia por Emissão de Positrões; correcção de sensibilidade; correcção de *randoms*; correcção de fotões dispersos.

Acronyms and abbreviations

APD	Avalanche Photodiode
ART	Algebraic Reconstruction Technique
CT	Computed Tomography
DOI	Depth of Interaction
FOV	Field of View
FBP	Filtered Backprojection
FWHM	Full Width at Half Maximum
LOR	Line of Response
ML-EM	Maximum Likelihood - Expectation Maximization
MRI	Magnetic Resonance Imaging
OS-EM	Ordered Subsets - Expectation Maximization
PEM	Positron Emission Mammography
PET	Positron Emission Tomography
ROI	Region of Interest
SNR	Signal to Noise Ratio
SPECT	Single Photon Emission Computed Tomography
TOR	Tube of Response

Contents

Acknowledgments	vii
Abstract	ix
Resumo	xi
Acronyms and abbreviations	xiii
Contents	xv
List of Figures	xvii
List of Tables	xxi
Chapter 1. Introduction	1
Chapter 2. Positron Emission Tomography	5
2.1. Nuclear Medicine	5
2.2. Physical basis.....	5
2.2.1. Positron Emission.....	6
2.2.2. Annihilation.....	7
2.3. Interactions with matter	9
2.3.1. Photoelectric Effect	9
2.3.2. Compton Scattering	10
2.3.3. Photon Attenuation	11
2.4. Positron Emission Mammography	12
Chapter 3. The Clear-PEM Scanner	15
3.1. The scanner	15
3.2. Radiation Detectors.....	16
3.2.1. Scintillators and Avalanche Photodiodes	16
3.2.2. Coincidence Detection	17
Chapter 4. Data Acquisition and Image Reconstruction	19
4.1. Organization of Acquired Data	19
4.1.1. Data Rebinning.....	20
4.1.2. Linograms.....	21
4.2. Image Reconstruction	23
4.3. Analytic Image Reconstruction	24
4.4. Iterative Image Reconstruction.....	24
4.4.1. System Matrix Calculation	26

4.4.1.1. The Pixel-Driven Method	26
4.4.1.2. The Ray-Driven Method	27
4.4.1.3. The Tube-Driven Method	27
4.4.2. The Algebraic Reconstruction Technique (ART)	29
4.4.3. The Maximum Likelihood - Expectation Maximization (ML-EM)	30
4.4.4. The Ordered Subsets - Expectation Maximization (OS-EM)	30
Chapter 5. Sensitivity Correction	33
5.1. Sensitivity and Detector Gaps	33
5.2. Correction Based on the Planar Source Acquisition	35
5.2.1. The Phantoms used	35
5.2.1.1. Planar Source	35
5.2.1.2. Cylindrical phantom	36
5.2.2. Threshold Definition	36
5.2.3. Studies in the Cylindrical Phantom	38
5.2.3.1. Reconstruction Assessment	38
5.2.3.2. Linogram Assessment	42
5.2.4. Validation with Clinical Data	47
5.2.4.1. Image Noise	48
5.2.4.2. Presence of High Intensity Pixels	50
5.2.5. Discussion	53
5.3. System Matrix Correction	53
5.3.1. Analytical Linogram	54
5.3.2. Validation with Planar Source	56
5.3.3. Incorporation on the System Matrix Calculation	57
Chapter 6. Random Correction	61
6.1. Timing Window	61
6.2. Random Correction	62
6.2.1. Image Contrast	64
6.2.2. Image Noise	70
6.2.3. Presence of High Intensity Pixels	72
6.2.4. Discussion	73
Chapter 7. Scattered Correction	75
7.1. Energy Window	75
7.2. Scattered Correction	76
7.2.1. Image Contrast	76
7.2.2. Image Noise	77
7.2.3. Spatial Resolution Studies	79
7.2.2.1. Point Source Phantom	79
7.2.2.2. FWHM	80
7.2.4. Discussion	83
Chapter 8. Main Discussion and Conclusions	85
Bibliography	87
Appendix	91

List of Figures

Figure 2.1: Positron decay [17].....	6
Figure 2.2: Annihilation reaction [17].....	8
Figure 2.3: Photoelectric effect [17].....	9
Figure 2.4: Predominant type of interaction for various combinations of incident photons and absorber atomic numbers [17].	10
Figure 2.5: Compton scattering [17].....	10
Figure 3.1: Clear-PEM breast acquisition [21].	15
Figure 3.2: Clear-PEM axillary region acquisition [21].	15
Figure 3.3: Schematic drawing of the Clear-PEM scanner [18].....	17
Figure 3.4: Types of coincidences detected in a PET imaging system: (a) Scattered coincidences; (b) Random coincidences; (c) True coincidences. Figure adapted from [23].	17
Figure 4.1: Single Slice Rebinning.	21
Figure 4.2: Definition of linogram coordinates. Figure adapted from [28].....	22
Figure 4.3: Linogram example. Figure adapted from [28].....	22
Figure 4.4: (a) Detectable LORs with $v=0$; (b) Detectable LORs with $v=v_{min}$ and $v=v_{max}$; (c) Detectable LORs with $u=u_{min}$ and $u=u_{max}$; (d) Detectable region of a linogram. Figure adapted from [28].	23
Figure 4.5: Backprojection. The image reconstruction quality increases with the number of projections [23].....	24
Figure 4.6: Iterative reconstruction process. Figure adapted from [23].....	25
Figure 4.7: Possible intersections between a TOR and a pixel: (a) a trapezium, (b) the entire pixel except one or two triangles, or (c) one triangle.	28
Figure 4.8: Variables used to calculate the area of intersection between the TOR and the pixel.	29
Figure 5.1: Representation of four Clear-PEM modules, with emphasis on the gaps between the crystals.	34

Figure 5.2: Different number of LORs is detected, depending on the position of the event.....	34
Figure 5.3: Picture of the planar source during its acquisition in the Clear-PEM prototype.....	35
Figure 5.4: (a) ^{68}Ge cylindrical phantom. (b) Picture of the phantom inside the support used for the acquisition.....	36
Figure 5.5: Image reconstruction of the cylindrical phantom without sensitivity corrections in the (a) yz and (b) xy planes.....	36
Figure 5.6: Representation of the ROIs used in the study for (a) yz , (b) xz and (c) xy views.	39
Figure 5.7: SNR values obtained for the 50 th slice of the xz, yz and xy plane of the cylindrical phantom, with a 0.001 threshold, during 10 iterations.....	40
Figure 5.8: Images reconstructed with OS-EM 2D from the 1 st to the 10 th iteration, with the same sensitivity correction threshold.	40
Figure 5.9: SNR values obtained for the 50 th slice of the xy plane of the cylindrical phantom after 3 iterations.	41
Figure 5.10: SNR values obtained for the 50 th slice of the xz plane of the cylindrical phantom after 3 iterations.	41
Figure 5.11: SNR values obtained for the 50 th slice of the yz plane of the cylindrical phantom after 3 iterations.	41
Figure 5.12: SNR values obtained for the 72 nd slice of the xy plane of the cylindrical phantom after 3 iterations.	42
Figure 5.13: Linograms of the cylindrical phantom acquisition without sensitivity corrections for (a) yz , (b) xz and (c) xy planes.	42
Figure 5.14: Representation of the ROI drawn in the linograms.....	43
Figure 5.15: SNR values obtained for a ROI of the xy plane of the cylindrical phantom linogram.....	43
Figure 5.16: Representation of a profile analysis in an uncorrected linogram.	44
Figure 5.17: Representation of a profile analysis in a corrected linogram with a 0.002 threshold.....	44
Figure 5.18: SNR values obtained for a profile of the xy plane of the cylindrical phantom linogram.....	45
Figure 5.19: SNR values obtained for a profile of the xy plane of the cylindrical phantom linogram.....	46
Figure 5.20: Image reconstruction of the first clinical case in the (a) yz, (b) xz and (c) xy planes, without sensitivity correction (reverse grey scale).....	47

Figure 5.21: Reconstructed images of 4 of the first clinical cases with sensitivity correction (reverse grey scale).....	48
Figure 5.22: Central ROI marked on clinical cases 1 a 3.	48
Figure 5.23: SNR values obtained with a central ROI for slice 44 of clinical case 1.	49
Figure 5.24: SNR values obtained with a central ROI for slice 53 of clinical case 1.	49
Figure 5.25: SNR values obtained with a central ROI for slice 41 of clinical case 3.	49
Figure 5.26: SNR values obtained with a central ROI for slice 52 of clinical case 3.	50
Figure 5.27: Image reconstruction of the same slice corrected with different thresholds.	51
Figure 5.28: Rectangular ROI marked on clinical cases 1 a 3.	51
Figure 5.29: Maximum values obtained with a bottom rectangular ROI for clinical case 1.	52
Figure 5.30: Maximum values obtained with a bottom rectangular ROI for clinical case 3.	52
Figure 5.31: Variables definition for lengths of the LORs in a linogram.	54
Figure 5.32: Representation of the analytic linogram created.	56
Figure 5.33: Result of difference (c) between the analytic linogram (a) and the planar source acquisition (b).	57
Figure 5.34: Cylinder reconstruction with (a) analytic linogram and (b) the planar source acquisition with a 0.005 threshold.....	58
Figure 5.35: Image reconstruction of clinical 1 with (a) analytic linogram and (b) the planar source acquisition with a 0.005 threshold.....	58
Figure 5.36: Image reconstruction of clinical 3 with (a) analytic linogram and (b) the planar source acquisition with a 0.005 threshold.....	59
Figure 6.1: Result of difference (c) between the regular reconstruction (a) and the reconstruction of the random corrected data (b) with an 8 ns timing window.....	63
Figure 6.2: Circular ROIs marked on clinical cases 1, 3, 4 and 5.....	65
Figure 6.3: Rectangular ROIs marked on clinical cases 1, 3, 4 and 5.....	65
Figure 6.4: Contrast values obtained for Clinical 1 with a circular ROI.	66
Figure 6.5: Detail of the contrast values obtained for Clinical 1 with a circular ROI.	66
Figure 6.6: Contrast values obtained for Clinical 3 with a circular ROI.	66
Figure 6.7: Detail of the contrast values obtained for Clinical 3 with a circular ROI.	67
Figure 6.8: Contrast values obtained for Clinical 5 with a circular ROI.	67
Figure 6.9: Detail of the contrast values obtained for Clinical 5 with a circular ROI.	67
Figure 6.10: Contrast values obtained for Clinical 1 with a rectangular ROI.	68
Figure 6.11: Contrast values obtained for Clinical 3 with a rectangular ROI.	69
Figure 6.12: Detail of the contrast values obtained for Clinical 3 with a rectangular ROI.....	69
Figure 6.13: Contrast values obtained for Clinical 5 with a rectangular ROI.	69
Figure 6.14: Detail of the contrast values obtained for Clinical 5 with a rectangular ROI.....	70
Figure 6.15: SNR values obtained with a circular ROI for clinical case 1.....	71

Figure 6.16: SNR values obtained with a circular ROI for clinical case 3.	71
Figure 6.17: SNR values obtained with a circular ROI for clinical case 5.	71
Figure 6.18: Maximum values obtained with a bottom rectangular ROI for clinical case 1. ...	72
Figure 6.19: Maximum values obtained with a bottom rectangular ROI for clinical case 3. ...	72
Figure 6.20: Maximum values obtained with a bottom rectangular ROI for clinical case 5. ...	73
Figure 7.1: Contrast values obtained for Clinical 1 with a circular ROI.	76
Figure 7.2: Contrast values obtained for Clinical 3 with a circular ROI.	77
Figure 7.3: Contrast values obtained for Clinical 5 with a circular ROI.	77
Figure 7.4: SNR values obtained with a circular ROI for clinical case 1.	78
Figure 7.5: SNR values obtained with a circular ROI for clinical case 3.	78
Figure 7.6: SNR values obtained with a circular ROI for clinical case 5.	78
Figure 7.7: Image detail of the reconstruction of the point source phantom without corrections in the (a) yz, (b) xz and (c) xy planes.	80
Figure 7.8: Profile (a) and Gaussian curve fit (b) for the yz plane of the point source.....	81
Figure 7.9: Profile (a) and Gaussian curve fit (b) for the xz plane of the point source.....	81
Figure 7.10: Profile (a) and Gaussian curve fit (b) for the xy plane of the point source.	81
Figure 7.11: FWHM values for the point source phantom in plane yz.	82
Figure 7.12: FWHM values for the point source phantom in plane xz.	82
Figure 7.13: FWHM values for the point source phantom in plane xy.....	82

List of Tables

Table 2.1: Mass and Charge Properties of Nucleons, Electrons and Positrons [15].	6
Table 2.2: Some commonly used radioisotopes.	12
Table 5.1: Comparison between the SNR values obtained with the analytic linogram and the planar source acquisition with a 0.005 threshold.	59
Table 6.1: Relationship between the total and the random count numbers.	64
Table 7.1: Total count numbers with the variation of energy window.....	79
Table 7.2: Number of counts per acquisition position of the point source phantom.	80

Chapter 1.

Introduction

Cancer is the leading cause of death worldwide, and one of the main causes of death in Portugal, second only to cardiovascular diseases. It affects millions of people of every age, both male and female. Furthermore, breast cancer is the second leading cause of cancer deaths in women today (after lung cancer) and it is the most common cancer among women, excluding nonmelanoma skin cancers [1, 2]. A third of these cancers could be cured if detected early and treated adequately, so it is only natural that efforts are being taken in order to discover new, and more accurate, imaging techniques that enable the possibility of finding breast cancer in early stages [1-3].

There are several possible clinical imaging techniques from which one can choose for studying the breast. They are divided in two main categories: anatomical and functional. Imaging modalities predominantly anatomical, for example x-ray mammography, magnetic resonance imaging (MRI) or ultrasound, are used for imaging the structure or anatomical changes associated with an underlying pathology, whereas functional imaging, such as positron emission tomography (PET) or single photon emission computed tomography (SPECT), captures the physiology of the body or functional and metabolic changes associated with the pathology [4].

Most of the times, conventional x-ray mammography is chosen as a screening and diagnostic tool: it is not expensive, provides very high-resolution and it is easy to evaluate. Still, it holds a rather low specificity, which reflects as a large number of unnecessary biopsies [5]. The need to be replaced by other techniques presents itself regularly. When the breast tissue is denser than average, the sensitivity of the image is compromised and it is common to turn to ultrasound, and when it is necessary to assess the extent of the lesion (any abnormality or pathological change in the breast tissue), for its high sensitivity it is usual to prefer MRI [6]. However, none of these techniques has the ability to distinguish the biochemical characteristics and metabolic rate of the tissue. After the injection of a suitable tracer, nuclear medicine techniques can help to differentiate tissues with different metabolic rates [7]. Although PET was previously considered to be an expensive imaging modality, now there are some evidences that prove that it has a good cost/effect ratio, being the method of choice in functional medical imaging [8].

In order to improve the quality of these exams, smaller and organ-oriented scanners have been developed. One of the several research projects under development right now is the Clear-PEM project - a scanner that follows the same basic physical principals as PET, but that is completely focused on breast cancer detection. This new technique is called Positron Emission Mammography, or PEM.

This scanner is designed to detect small lesions or tumours in early stages, with high resolution and high sensitivity. It is composed by two detector plates that rotate around the breast to detect radiation and, in addition, it has the ability to perform a complementary exam of the axillary region.

At this stage, the prototype was assembled at the *Instituto Português de Oncologia do Porto* (IPO - Porto) and running on pre-clinical environment.

The purpose of this work is to improve the image quality by correcting the sensitivity of the images obtained, correcting the bias that is created by several elements, such as the gaps between the detector crystals.

The main goal now is to prepare the scanner for clinical validation, still the work developed in this thesis will not be directly applied in the clinical studies. A different study is being developed with that goal. In [9], the normalization model currently accounts for intrinsic and geometric efficiencies using new methods specially developed for this purpose, with the intent of correcting any sampling deficiency that might exist. Nevertheless, the need for more immediate methods led us to the development of this work.

After the acquisition, the data undergoes a process of reconstruction and corrections, and it is important to study which parameters should be adjusted in order to get the best contrast between lesions and the breast background, as well as meeting the high resolution standards we set to achieve. All the approaches followed, tests performed and results obtained will be presented.

This thesis is divided into eight chapters. We begin by providing some background theory in the first four chapters. **Chapter 1** is composed of the present **Introduction**, where previous work is presented, along with motivations and the objective of this work. In **Chapter 2**, a description of **Positron Emission Tomography** and all its basic physics are reviewed, from the moment the patient is injected with the radiopharmaceutical, until the radiation is emitted.

Chapter 3 introduces the imaging technique studied during this work, the **Positron Emission Mammography**. Not only is the prototype described, but the main differences compared to a whole-body PET scanner, how the radiation is detected, how the image is acquired, and what are the main characteristics and problems of the images, are thoroughly discussed.

Finally, the mathematical description of the data's pathway from acquisition to its final stage as an image is presented in **Chapter 4 – Data Acquisition and Image Reconstruction**.

The following three chapters, **Chapter 5**, **Chapter 6** and **Chapter 7**, describe the approaches used for **Sensitivity**, **Random** and **Scattered Correction**, respectively. All three have the same structure: they start with a small introduction to the subject, followed by the description of the methods used for the different studies, closing with a complete description of the results obtained and their discussion.

In **Chapter 8 – Main Conclusions and Future Work**, a comparison between all the results will be established, and the final conclusions and future work will be presented.

Chapter 2.

Positron Emission Tomography

2.1. Nuclear Medicine

In nuclear medicine, clinical information is derived from observing the distribution of a pharmaceutical administered to the patient. By marking the pharmaceutical with a radionuclide, it becomes possible to measure the distribution of this radiopharmaceutical by observing the amount of radioactivity present. Therefore, nuclear medicine is intrinsically a group of imaging techniques to analyze the body's biochemistry, with the results depending on the chosen radiopharmaceutical. The diagnostic information is provided by the action of the pharmaceutical; the role of the radioactivity is purely a passive one, enabling the radiopharmaceutical to be localized. For this reason the potential hazard to the patient can be kept to a minimum [3].

There are several different nuclear medicine techniques. The most commonly used are Positron Emission Tomography (PET), Single Photon Emission Computed Tomography (SPECT) [10] and planar scintigraphy [11, 12]. By now, it has become evident that tomographic techniques are substantially superior to the conventional planar imaging approach. Moreover, SPECT suffers from poor spatial, contrast and temporal resolutions compared with PET and, therefore, smaller lesions with low concentration of radiotracer can be readily missed [13]. PET can be used to measure tumour metabolism, assess blood flow and quantify oestrogen and progesterone receptor density. Although it might be the best choice in nuclear medicine to detect primary breast cancers, it is not superior in sensitivity or spatial resolution in comparison with conventional imaging methods (mammography, ultrasound and MRI). However, its major advantage is in providing images that show physiological function, and this is the reason that has attracted researchers to PET in an attempt to gain greater insight into in vivo tumour cell metabolism, growth and response to cytotoxic therapy [14].

2.2. Physical basis

In Nuclear Medicine techniques, as a result of the radiopharmaceutical administered to the patient, the labelled molecules will have nuclei with either an excess number of

protons or neutrons, and, therefore, will become unstable and prone to radioactive decay, leading to a change in the number of protons and neutrons in the nucleus and to a more stable configuration. Nuclei that decay in this manner are known as radionuclides. These radionuclides are produced in a cyclotron and are then used to label compounds of biological interest. The labelled compound (typically $10^{13} - 10^{15}$ labelled molecules) is introduced into the body, usually by intravenous injection, and is distributed in the tissues accordingly with its biochemical properties [15].

2.2.1. POSITRON EMISSION

The basic principle on which Positron Emission Tomography relies is positron decay (also known as β^+ decay). This happens when a radionuclide (or isotope) is proton-rich: the proton can be converted into a neutron and a positron (β^+ particle) along with a neutrino (ν) (Figure 2.1). A positron is the antiparticle of the electron: it has the same mass but opposite electric charge (see Table 2.1). Unlike the electron, the positron itself survives only briefly. It quickly encounters an electron, which are plentiful in matter, and both are annihilated [16, 17].

Essentially, the extra proton in the nucleus of an atom X will be converted to a neutron, releasing the extra positive charge with the positron, hence achieving stability:

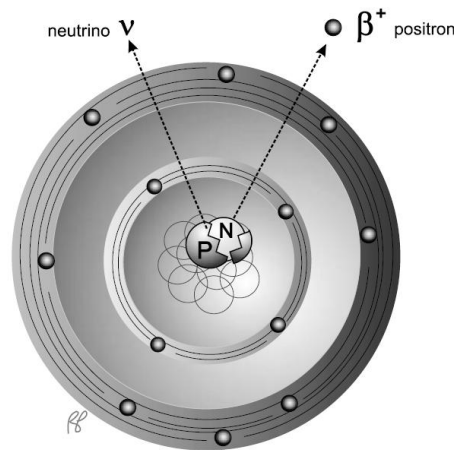


Figure 2.1: Positron decay [17].

Table 2.1: Mass and Charge Properties of Nucleons, Electrons and Positrons [15].

	<i>Proton (p)</i>	<i>Neutron (n)</i>	<i>Electron (e⁻)</i>	<i>Positron (e⁺)</i>
Mass	1.67×10^{-27} kg	1.67×10^{-27} kg	9.1×10^{-31} kg	9.1×10^{-31} kg
Charge	$+ 1.6 \times 10^{-19}$ C	0	$- 1.6 \times 10^{-19}$ C	$+ 1.6 \times 10^{-19}$ C

Proton-rich radionuclides can also decay by a process known as electron capture. Here, the nucleus captures an orbital electron and converts a proton into a neutron, thus decreasing the atomic number Z by one. Once again, a neutrino is released. These emissions may also be used for in vivo imaging (for instance, radiography) but do not share the unique properties of decay by positron emission. Radionuclides that decay predominantly by positron emission are the basis for PET imaging [15, 18].

2.2.2. ANNIHILATION

As positrons travel through human tissue, they give up their kinetic energy due to interactions with electrons, resulting in a very short lifetime. Once most of its energy is dissipated, it will combine with an electron and form a hydrogen-like state known as positronium. Establishing a comparison to hydrogen, we can say that in the positronium the proton that forms the nucleus is substituted by a positron. Given its instability, almost instantly after its formation, a process known as annihilation occurs, where the mass of the electron and positron is converted into electromagnetic energy. Because the positron and electron are almost at rest when this occurs, the energy released comes largely from the mass of the particles and can be calculated from Einstein's mass-energy equivalence as:

$$E = mc^2 = m_e c^2 + m_p c^2 \quad \text{Eq. 2.2}$$

where m_e is the mass of the electron, m_p is the mass of the positron, and c is the speed of light ($3 \times 10^8 \text{ ms}^{-1}$). Replacing the values from Table 2.1 in Eq. 2.2, and knowing that $1 \text{ eV} = 1.6 \times 10^{-19} \text{ J}$, we find that the energy released is, approximately, 1.022 MeV .

This energy is released in the form of high-energy photons. Once again, because the positron and electron are almost at rest, the momentum is close to zero. To respect physical laws, momentum, as well as energy, must be conserved, therefore it is not, in general, possible for the whole energy to be released by the emission of only one photon – a momentum would occur in the direction of that photon. To prevent that, the 1.022 MeV are divided into two photons of 511 keV emitted simultaneously in opposite directions (180° apart). This process is schematized in Figure 2.2. However, it is possible that the energy is split in more than two photons. This only occurs in about 0.003% of the annihilations. In less than 2% of the times, it also happens that the annihilation occurs without forming the positronium. Unless this threshold energy (1.022 MeV) is achieved, there will be insufficient energy available for positron emission [8, 15]. PET is based on the principle of coincidence detection of the two 511 keV photons.

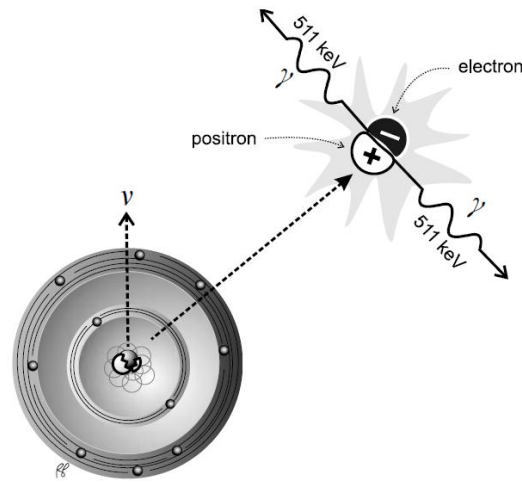


Figure 2.2: Annihilation reaction [17].

Usually, associated with the emission of a β particle is the emission of gamma rays, i.e., electromagnetic radiation is emitted from the nucleus after a spontaneous nuclear decay. Even though the annihilation photons fall in the gamma-ray region of the electromagnetic spectrum, the terms photons and gamma-rays are often used interchangeably when referring to the annihilation photons. That is incorrect. Although the properties of these photons are absolutely identical to a 511 keV gamma-ray, their origin reflects on the terminology. “Annihilation photons” is technically the correct term because the radiation does not arise directly from the nucleus.

The annihilation process is of extreme importance for the concept of PET, thanks to a number of properties. First, the photons that result from the annihilation are highly energetic (equivalent to gamma-rays), which means that, unlike x-rays, they have a good chance of escaping the body and hence being detected. For this reason, it is not the positrons (because they are absorbed locally) but the photons that are detected. Plus, the precise geometric relationship between the photons emitted, enables the drawing of a line, joining the two points at which the photons hit the detector, which passes directly through the point of annihilation. The line is known as Line of Response (LOR). Recall that the point of positron emission is not exactly the same as the annihilation point, but it is quite close, giving a good indication of where the radioactive atom was in the body. Finally, no matter what is the element involved, or the energy of the emitted positrons, all positron-emitting radionuclides ultimately lead to the emission of two back-to-back 511 keV photons. Consequently, all PET scanners can be designed and optimized for imaging all positron-emitting radionuclides at this single energy. However, this characteristic makes it impossible to perform dual-radionuclide studies with PET and distinguish between the radionuclides based on the energy of the emissions [15].

2.3. Interactions with matter

There are several types of radiations and each one has distinctive interactions with matter. This study will focus on the interaction of the 511 *keV* photons with matter.

After comprehending the whole process of how these photons are emitted, it is important to understand how they interact with matter, whether it is with the tissue surrounding them, the detector material of the PET scanner, or with possible shielding materials such as lead and tungsten.

As was explained before, these high-energetic photons have the same behaviour as gamma-rays, hence they will interact with matter by two major mechanisms: photoelectric effect and Compton scattering. There is also another very common mechanism for electromagnetic radiation – pair production. However, it only takes place when the photon's energy is higher than 1.022 *MeV*, thus it is outside our scope and will not be analysed.

2.3.1. PHOTOELECTRIC EFFECT

The photoelectric effect, schematized in Figure 2.3, is an interaction of photons with the orbital electrons of an atom. The photon transfers its entire energy to an inner shell electron, provoking its ejection. As for the photon, it is completely absorbed by the surrounding tissue. The ejected electron, known as photoelectron, will have energy equal to $E_p - E_B$, where E_p is the energy of the photon (supposedly, 511 *keV*), and E_B is the binding energy of the electron in the shell. In solids and liquids, the photoelectron is quickly absorbed. The vacancy left in the shell is filled in by the transmission of an electron from the upper shell, which is followed by the emission of the energy difference between the two shells as characteristic x-rays. Alternately, instead of emitting an x-ray, the atom may emit a second electron to remove the energy, the Auger electron.

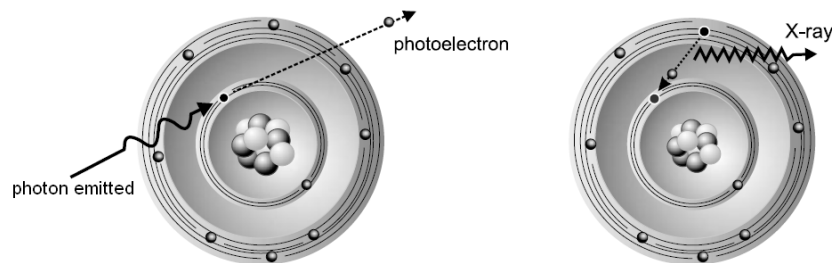


Figure 2.3: Photoelectric effect [17].

The photoelectric effect is dominant in human tissue at energies below 100 *keV* (Figure 2.4). Hence, it is important for x-ray imaging, and for imaging with low-energy radionuclides. It has little impact on PET itself, but with the development of combined PET/CT [19] systems it assumes a more important role [8, 15, 16].

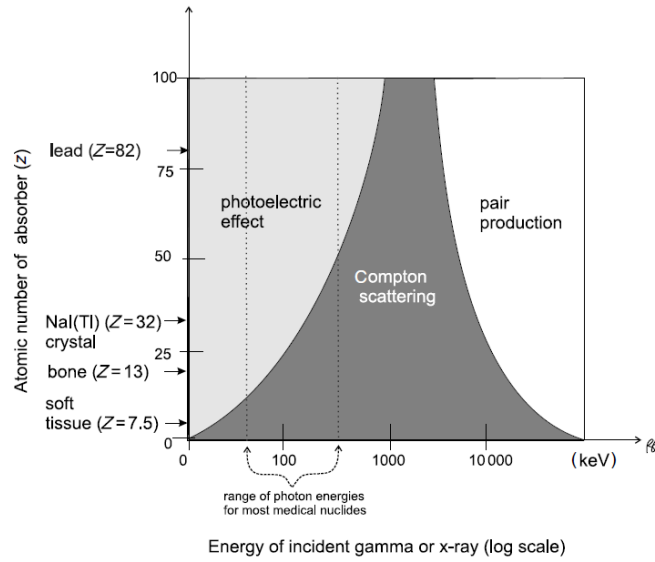


Figure 2.4: Predominant type of interaction for various combinations of incident photons and absorber atomic numbers [17].

2.3.2. COMPTON SCATTERING

In a Compton scattering process (Figure 2.5), the incident photon interacts with an outer shell loosely bound (essentially free) electron of the absorber atom, transferring only part of its energy to the electron, hence ejecting it and changing direction in the process.

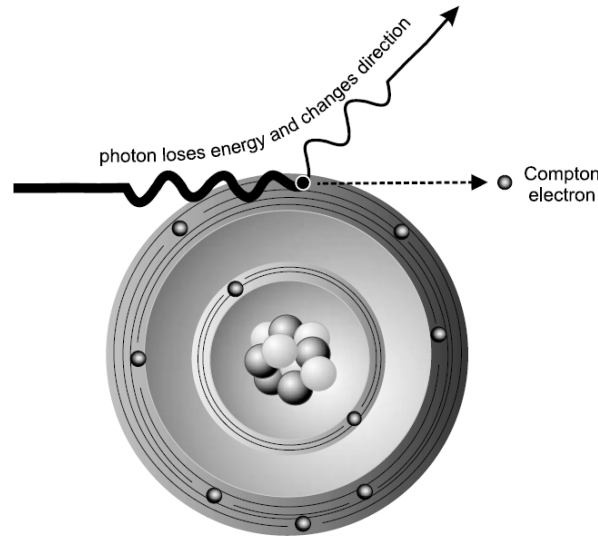


Figure 2.5: Compton scattering [17].

The ejected electron is called Compton electron. Imposed conservation of momentum and energy leads to a simple relationship between the energy of the original photon (E), the energy of the scattered photon (E_{sc}) and the angle through which it is scattered, θ , the Compton equation:

$$E_{sc} = \frac{m_e c^2}{\frac{m_e c^2}{E} + 1 - \cos \theta} \quad \text{Eq. 2.3}$$

As was proved before, $m_e c^2 = 511 \text{ keV}$, and the incoming photon also has an energy of 511 keV . Therefore:

$$E_{sc} (\text{keV}) = \frac{511}{2 - \cos \theta} \quad \text{Eq. 2.4}$$

The maximum energy loss occurs when the scattering angle is 180° , i.e., the photon is back-scattered. In this case, the annihilation photon would have 170 keV .

However, the scattered photon might encounter a photoelectric process or another Compton scattering process, or leave the absorber without interaction. As the energy of the photon increases, the photoelectric process decreases and the Compton scattering process increases, until approximately 1.0 MeV [8, 15, 16].

Compton scattering takes a very important role in PET imaging. Further explanations will be presented in the next chapter.

2.3.3. PHOTON ATTENUATION

As the result of the interactions (absorption or scattering) between photons and matter, the intensity of the beam (stream of photons), which corresponds to the number of photons remaining in the beam, decreases as the beam passes through matter. This loss of photons is called attenuation, and can be described by a simple exponential relationship:

$$I_x = I_0 \exp(-\mu x) \quad \text{Eq. 2.5}$$

where I_0 is the 511 keV photon flux prior to the interaction, x is the thickness of the medium, I_x is the flux of photons that passes the attenuator without interaction and μ is the linear attenuation coefficient, it is a property of the medium and represents the probability per unit distance that an interaction will occur. The linear attenuation coefficient depends on the energy of the photons and on the average atomic number and thickness of the attenuator. As might be expected, the attenuation increases with the low energy of the photons or with the augmentation of the average atomic number or thickness of the attenuator [15, 17].

To be detected, the annihilation photons must pass through the body. In this path, as shown in Figure 2.4, the dominant form of interaction is Compton scattering. For this reason, the signal will be attenuated through the redirection of the annihilation photons. The angular correlation between the annihilation photons is randomized by the scattering process, so if the redirected photons still escape the body and are detected in the PET scanner, they will be incorrectly located. This results in a background of scattered events in the images [15].

The function of the PET scanner is to detect those 511 *keV* photons that escape the body without interacting. The detector should, therefore, have a high probability of stopping these photons, that is, a very dense material, with large values of μ .

2.4. Positron Emission Mammography

In a whole-body PET exam, the patient, after being injected with a radiopharmaceutical chosen accordingly to the exam, is placed inside a cylindrical scanner with crystals that detect the radiation emitted from inside the patient's body due to the radio decay. Although the current generation of PET systems have a spatial image resolution of approximately 3–4 *mm*, this still limits its ability to detect small lesions [6].

Sharing PET's basic principles, Positron Emission Mammography (PEM) is an organ-oriented functional imaging technique specifically designed to detect breast tumours. This dedicated equipment will introduce the potential for improving important parameters such as sensitivity and spatial resolution. Moreover, an increased sensitivity allows a lower injected dose and a shorter examination time [20].

The first step is choosing an appropriate radiotracer. In Table 2.2 are presented the most common positron emitter isotopes for whole-body PET.

Table 2.2: Some commonly used radioisotopes.

<i>Isotope</i>	<i>Half-life (min)</i>
¹¹ C	20.4
¹³ N	9.96
¹⁵ O	2.07
¹⁸ F	109.8

Due to their short half-life¹ ($t_{1/2}$), the use of ¹¹C, ¹³N or ¹⁵O would implicate the existence of a cyclotron near the facility where the scanner is located, thus the most viable choice is ¹⁸F – fluorine. Nevertheless, the isotope by itself will not be enough, it has to be coupled to a molecule, and to choose that molecule we need to know what we want to trace.

A tumour is an abnormal growth of cells that can be either benign or malignant. Even though only malignant tumours are defined as cancer, in both cases the higher metabolic activity of the swelling, compared to the surrounding tissue, creates excellent conditions for functional imaging. The changes in the cells' metabolism will widely increase their glucose consumption, hence, by substituting glucose for an analogue, such as deoxyglucose, the metabolism will be traced.

¹ The half-life is the average time in which the nuclei of one-half of a given population of atoms will undergo radioactive decay.

For all these reasons, the most common radioisotope for positron emission mammography is fluorine-18 (^{18}F) labelled to fluorodeoxyglucose to produce ^{18}F -FDG. This modified glucose molecule behaves like normal glucose, being actively transported into cells as their main source of energy, until glycolysis starts. Unable to continue along the glycolytic metabolism pathway for energy, it becomes trapped inside the cells, with a concentration proportional to its metabolism. Thus the tumours get highlighted compared to their surroundings.

Chapter 3.

The Clear-PEM Scanner

While in the previous chapter the physical basics of positron emission tomography in general were introduced, from this point on the Clear-PEM scanner's individual characteristics will be presented.

3.1. The scanner

The Clear-PEM detector is a dual planar positron emission mammography tomograph that is being developed by a consortium of several Portuguese institutions, within the framework of the international Crystal Clear Collaboration at CERN [5]. The scanner has two planar detectors that can rotate around the breast (Figure 3.1) and perform a complementary acquisition of the axillary region (Figure 3.2).

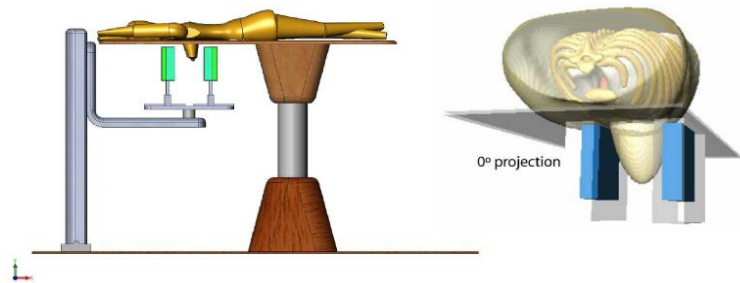


Figure 3.1: Clear-PEM breast acquisition [21].

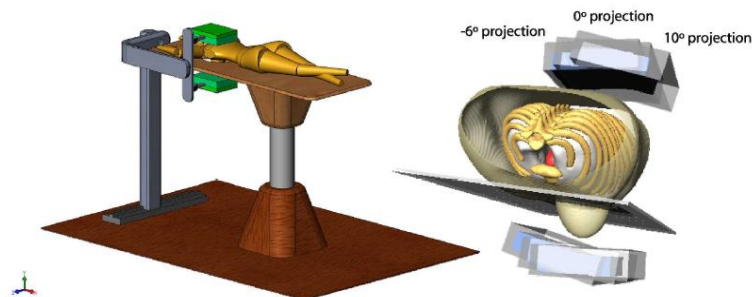


Figure 3.2: Clear-PEM axillary region acquisition [21].

During the procedure the patient is lying in prone position with the breast hanging through an aperture in an imaging table with the two detector heads positioned in each side of the breast. The detector heads can rotate around the breast in order to collect data at several angular orientations for tomographic reconstruction.

3.2. Radiation Detectors

After escaping the body the annihilation photons (ionising radiation) are still highly energetic. The detectors' function is to stop these photons and assess the total energy that they hold. They do so by converting the energy into a measurable electrical signal. The integral of this signal will be proportional to the total energy deposited in the detector by the radiation [8].

3.2.1. SCINTILLATORS AND AVALANCHE PHOTODIODES

There are several categories of detectors but, due to their good stopping efficiency and energy resolution, the scintillators are the most common in PET imaging. These detectors consist of an inorganic crystal (scintillator) which emits visible (scintillation) light photons after the interaction of radiation within the detector. Coupled to the crystal, a photo-detector is then used to detect and measure the number of scintillation photons emitted and convert them into an electrical current, in this case avalanche photodiodes (APD) were the choice. The number of scintillation photons (or intensity of light) is proportional to the energy deposited within the crystal. The use of APD arrays on both front and back surfaces of scintillators allows a precise identification of the detector element in which the interaction occurred and, by comparing the light that reached both APDs, to assess the depth of interaction (DOI) [8, 15].

Due to its high gamma absorption and fast decay time LYSO:Ce (Cerium-doped Lutetium Yttrium OrthoSilicate) was chosen as scintillator for the prototype. The crystals, each with $2 \times 2 \times 20 \text{ mm}^3$, are arranged in 4×8 matrices optically coupled on each side to 4×8 APD arrays ($1.6 \times 1.6 \text{ mm}^2$ pixel size) in a double-readout configuration. This constitutes one module. Each 24 modules are grouped (2×12) into one supermodule and each detector head is formed by assembling 4 supermodules side by side, as shown in Figure 3.3. The Clear-PEM scanner consists of two parallel detector heads covering a $17.3 \times 15.2 \text{ cm}^2$ FOV, coming to a total of 6144 LYSO:Ce crystals [22].

This geometry is rather flexible and by positioning the plates at different separation distances the detector can easily accommodate different breast shapes and sizes.

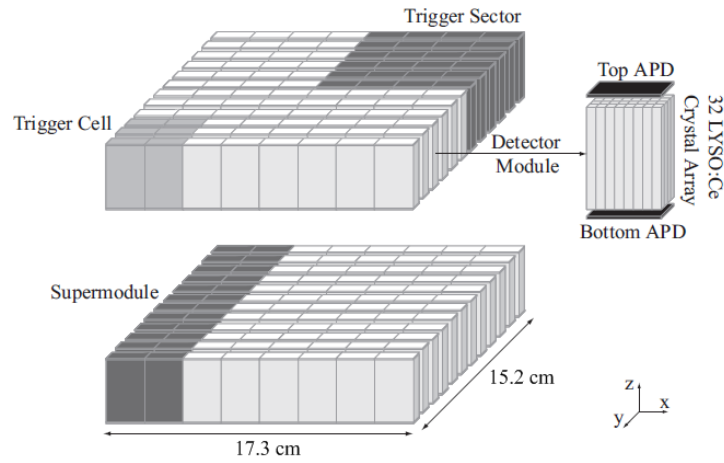


Figure 3.3: Schematic drawing of the Clear-PEM scanner [18].

3.2.2. COINCIDENCE DETECTION

These two heads are designed to detect and localize the origin of the simultaneous back-to-back annihilation photons, also known as coincidences. There are three types of coincidence events that can be measured: true, scattered and random.

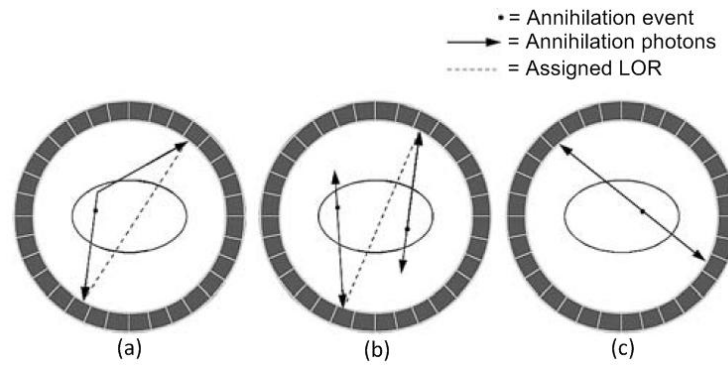


Figure 3.4: Types of coincidences detected in a PET imaging system: (a) Scattered coincidences; (b) Random coincidences; (c) True coincidences. Figure adapted from [23].

Scattered events (Figure 3.4 (a)) are measured when one or both annihilation photons interact in the body prior to detection and are scattered within the patient. This results in a mispositioning of the event. Random coincidences (Figure 3.4 (b)) occur if two separate decays take place close enough in time to look like a single decay to the system electronics; these events form a background in the data that needs to be subtracted. And finally, true coincidences (Figure 3.4 (c)) happen when both annihilation photons escape the body and are recorded simultaneously by a pair of detectors. Both true and scattered events are referred to as prompt events because they come from the decay of a single nucleus and, thus, the annihilation photons are detected almost simultaneously. The prompt rate is related linearly to the activity in the patient. However, the random rate increases as the

square of the activity in the patient and becomes more dominant at higher activity levels. The goal in PEM, as well as in PET imaging, is to be able to measure and reconstruct the distribution of true events while minimizing the scattered and random coincidences and correcting for the bias associated with the scattered and random coincidences [23].

The total number of coincident events acquired by a pair of detectors is related to the integral of the activity along the LOR that joins the two detectors. By assessing the integral of the activity along sets of LORs it is possible to obtain projection data that can be reconstructed and form an image of the distribution of radioactivity within the patient [3].

Only a small number of the events processed by each detector are in coincidence. The rate of events processed by each detector is often referred to as the single event rate for that detector, whereas the coincidence event rate includes true events, scattered events and random events. [23]

For some detectors, it is possible to measure the Time-of-Flight (TOF) of the photons: extremely fast scintillators with a good time resolution are used to assess the actual time difference (δt) between the detection of two coincident photons originating from the same annihilation process. Using the speed of light, c , and the precise values of the TOF of the photons, the distance from the annihilation point to each detector will be calculated and thus the exact point of the annihilation in the LOR defined. This method is then used to improve the signal-to-noise ratio (SNR) in image data, resulting in higher image quality, shorter imaging times or a lower dose to the patient [8, 24].

Chapter 4.

Data Acquisition and Image Reconstruction

This chapter will be used to describe the path that data undergoes since its acquisition by the Clear-PEM detectors until it becomes an image ready for analysis.

During the exam, a number of views are acquired at different positions given by the rotation of the detectors around the breast. Each view, or projection, will only give information about one plane, much like a picture. They all need to be combined and enter a series of procedures that will, in the end, generate a 3D image of the radiotracer's distribution inside the examined breast.

There is more than one way to transform the projections into a tomographic image, and as each step of the process is explained, all the solutions will be presented, but only the ones selected for this work will be fully explained. In this work, all datasets were rebinned (process which will be explained later) into 2D Lines of Response (LORs) using Single Slice Rebinning (SSRB) and grouped into linograms. For this reason, we will centre our attention on 2D image reconstruction methods.

Originally, all the software used was developed in C. With the development of the project came the need to have specific software designed for image visualization and data analysis, so all the image reconstruction algorithms were optimized to IDL data language [25] and embedded in the visualization software developed.

4.1. Organization of Acquired Data

There are two possible acquisition modes in PET: 2D and 3D. 2D PET is characterized by the usage of lead sheets separating the detector rings. These define the angular limits of possible LORs and lead to a division of the LORs by slice, each being reconstructed independently. Hence, a faster reconstruction process is achieved, since it just needs to consider a subset of all LORs to reconstruct each slice. However, despite the reduction in the number of scattered and random coincidences detected, the detection sensitivity is compromised, since the collimators also avoid the detection of many true coincidences. These conclusions led to the removal of the septa allowing coincidence events from all of the LORs among the detectors. And thus was created the 3D PET, the mode used by the Clear-PEM scanner.

The amount of data that emerges from these exams is quite large, requiring organization and parameterization, the first steps of the image reconstruction process.

Throughout the exam, events that meet both the energy and timing criteria are saved to disk in a binary raw data file. After each scanner acquisition, a list-mode file containing relevant information regarding the event, such as the activated crystals, the interaction coordinates (x, y, z), the deposited energy and a time stamp, is stored sequentially on disk and used directly for image reconstruction [26]. List mode data is advantageous for reconstruction and image correction studies, as the data for reconstruction can be selected from the original file, by creating a new one. Also, it is compact for the big sets of 3D data, and it is easy to convert to quite a few types of parameterization.

After this, a data parameterization will occur, in which the similar LORs will be grouped accordingly to their geometrical characteristics. The most commonly used parameterization in both 2D and 3D whole-body PET scanners, due to their cylindrical shape, is the sinogram [27, 28] – a histogram obtained with polar coordinates. For this kind of systems, the angular parameterization is an obvious choice, because treating each angular projection separately is advantageous for the reconstruction.

As we have seen, the Clear-PEM scanner has two planar detectors that rotate around the breast. For this kind of tomography, called limited angle tomography, the polar coordinates might not be the best choice, but perhaps a set of coordinates based on the planar nature of the acquisition geometry, which would also present advantages for the reconstruction process. Instead of corresponding to a sinusoidal curve, like in a sinogram, the LORs that pass through a fixed point in the object should correspond to a straight line. This kind of parameterization exists, is called linogram [29, 30] and was our choice for this work.

4.1.1. DATA REBINNING

As explained previously, the volume of data that emerges from 3D PET is quite large. In order to make up for the lack of computer power and to improve the reconstruction speed, a procedure called rebinning was created. The objective is to divide the 3D data into smaller 2D data sets. By doing so, instead of reconstructing all the data at the same time, each set will be reconstructed independently, significantly reducing computational time and allowing its use in clinical practice. Although rebinning methods are not specifically a reconstruction procedure, they are an important addition to the group of techniques that bear on three-dimensional image reconstruction problems [23].

Several approximate rebinning methods have been published over the years, firstly Single Slice rebinning (SSRB) [31] and Multi Slice rebinning (MSRB) [32], both fast but prone to imprecision. Later, methods based on the frequency-distance principle of the Fourier

transform – Fourier rebinning (FORE) algorithms [33] were presented, more accurate and more time consuming. Eventually, they originated an exact algorithm, with the Fourier transform principle together with some particularities of John's equation - FORE-J [28, 34, 35].

Although the FORE-J algorithm has been developed for the Clear-PEM scanner, it is yet to be corrected. This work was developed using only SSRB, so it will be presented in detail.

The **Single Slice Rebinning** (SSRB) algorithm [31] is very fast but leads to inaccurate solutions. Its main goal is to transform each oblique LOR in a LOR perpendicular to the rotation axis lying in the plane that crosses the original LOR in its midpoint [28] (see Figure 4.1). This method is accurate for sources near the scanner axis, since the rebinned LOR will still cross the emission point. Nevertheless, axial blurring and transaxial distortions increase with the distance from the axis of the scanner, and, at the same time, spatial resolution gets degraded.

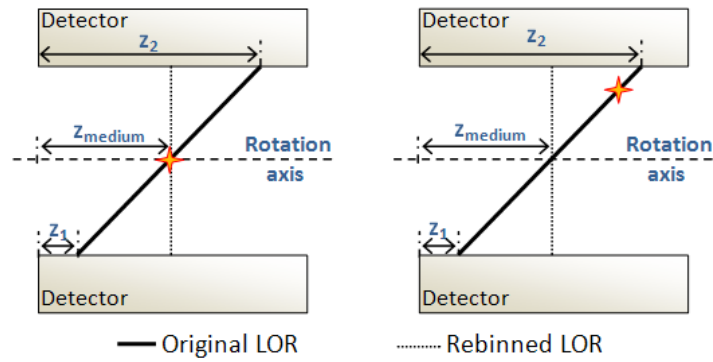


Figure 4.1: Single Slice Rebinning.

4.1.2. LINOGRAMS

In 1987, Edholm [29] proposed an alternative to the highly used sinogram by choosing new coordinates (u, v) to parameterize a LOR in limited angle tomography acquisitions. The linogram will be a plot of v as a function of u , with this coordinates defined by:

$$u = \frac{x_{d2} + x_{d1}}{2} \quad \text{Eq. 4.1}$$

$$v = \frac{x_{d2} - x_{d1}}{2} \quad \text{Eq. 4.2}$$

where x_{d1} and x_{d2} are the points of entrance of the LOR, respectively, in detector 1 and 2.

According to these definitions, in a linogram, each column, u , represents the interception coordinate between the LOR and the central plane of the FOV, and each line, v , is a function of the LOR's slope (see Figure 4.2).

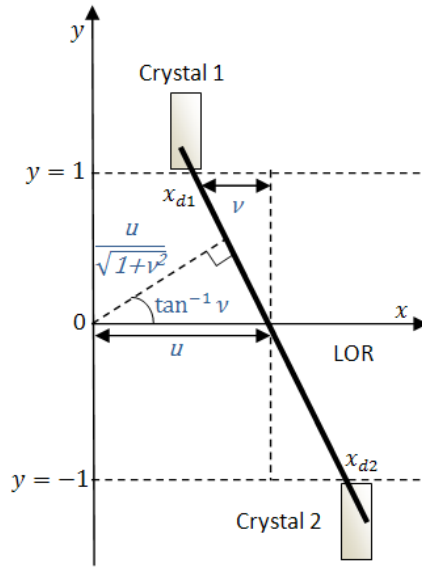


Figure 4.2: Definition of linogram coordinates. Figure adapted from [28].

Each line in a linogram represents a set of LORs that cross a certain pixel (x_0, y_0) , which means that they have to satisfy the following condition:

$$u = x + yv \quad [29] \quad \text{Eq. 4.3}$$

as proven in the example shown on Figure 4.3. Here one can see that for five activity sources, five straight lines are generated.

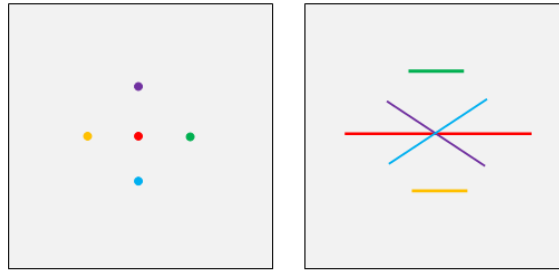


Figure 4.3: Linogram example. Figure adapted from [28].

The backprojection (see section 4.3) of all the LORs passing through a point in the image now corresponds to integration along a straight line in the linogram, which is a simpler interpolation problem than the used backprojection of sinograms [23].

Still, there is one limitation for the use of this parameterization: it is impossible to represent a LOR parallel to the x-axis, otherwise the v coordinate would be undefined. To solve this problem, the x-axis is now associated with the detectors and one linogram is created per projection. For each exam, is required a minimum of two projections, perpendicular to each other (90° degrees apart).

Usually, for cylindrical detectors, sinograms and linograms are represented as a 2D rectangular map. As a result of the well defined FOV of the detector, it is easy to understand the limits of the LORs acquisitions and determinate the shape of the detectable region. For LORs perpendicular to the detector ($v = 0$), all possible u values correspond to detectable LORs (Figure 4.4 (a)), whereas for LORs with the maximum slope (v_{max} or v_{min}) only LORs with $u = u_{medium}$ are detectable (Figure 4.4 (b)). Also LORs crossing the central plane of the FOV in its limits (u_{max} or u_{min}) are detectable only with $v = 0$ (Figure 4.4 (c)). Thus, all the detectable LORs are located within a rhombus (Figure 4.4 (d)), whose dimensions depend on the distance between the detectors [28].

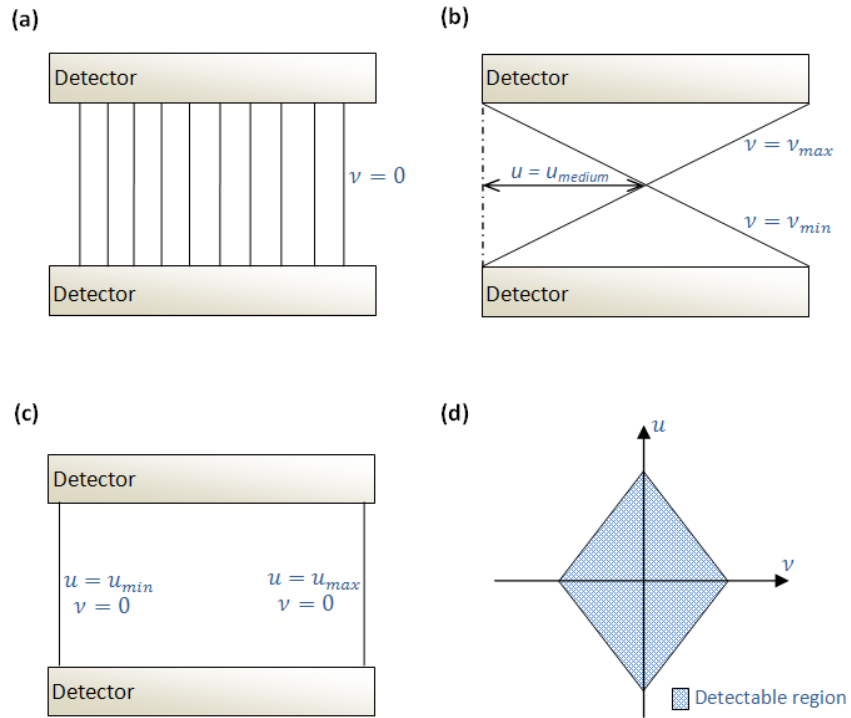


Figure 4.4: (a) Detectable LORs with $v=0$; (b) Detectable LORs with $v=v_{min}$ and $v=v_{max}$; (c) Detectable LORs with $u=u_{min}$ and $u=u_{max}$; (d) Detectable region of a linogram. Figure adapted from [28].

A generalization of the 2D linogram was presented in 2001 by Kinahan *et al* [36], introducing the concept of the planogram data format for fully-3D imaging.

4.2. Image Reconstruction

The purpose of tomographic image reconstruction is to take the data acquired by the scanner as projection views and transform it into an accurate three-dimensional representation of the patient, or in PEM's case, of the radiopharmaceutical distribution in the breast to obtain functional information. This essentially allows an inside look at the body in a completely noninvasive way. There are two basic approaches to image reconstruction: analytic and iterative, the latter being our choice for this work.

4.3. Analytic Image Reconstruction

The basis for most analytic reconstruction methods is linear superposition of backprojections, often known simply as backprojection. This algorithm is based on the mathematics of computed tomography (CT) that relates line integral measurements to the activity distribution in the object. Essentially, the counts from a detector pair are being projected back along the line from which they were originated. This process is repeated for all valid detector pairs in the PET system, and all the counts from all detector pairs are added, as schematized on Figure 4.5.

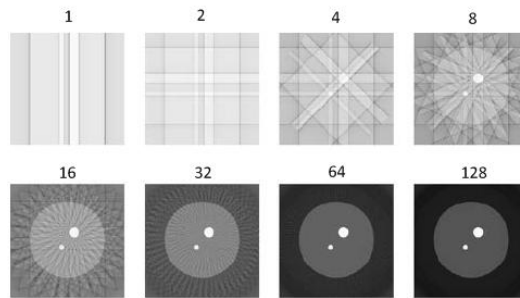


Figure 4.5: Backprojection. The image reconstruction quality increases with the number of projections [23].

The most frequently used method is the Filtered Backprojection (FBP) [15, 23, 37]. Not only it is fast, but intuitive and has a well known performance, thus becoming appealing for clinical practice. However, it has some downsides. The biggest one comes from the fact that we do not have continuous sampling of the object, but a finite number of projections, and as a result, a radial blurring effect is generated. Moreover, the impossibility of incorporating previous knowledge such as the structures in study, the geometry of the detector or even a model of emission into the algorithm, are some of the reasons that encourage the use of iterative methods instead.

4.4. Iterative Image Reconstruction

Due to long computational time, iterative image reconstruction methods [38] were pushed aside from clinical practice for years. Only more recently, with the enhancement of computer power, have these methods experienced significant progress, becoming faster and a valid option for clinical tomographic reconstruction.

The main goal of this method is to generate a close estimate of the distribution of the activity in the different planes of the image and to compare the projections of this estimate with the projections acquired. The algorithm starts with an initial estimate of the data to produce a set of transaxial slices. These slices are then used to create a second set of projection views, which are compared to the original ones acquired from the patient. The transaxial slices from the computer's estimate are then modified using the difference

between, or ratio of, the two sets of projection views. If everything proceeds efficiently, each sequence, or iteration, generates a new set of projection views that is more similar to the original ones. The process is complete when the difference between the projection views of the estimated data and the original data is below a pre-determined threshold [17].

Even though the final results take longer to achieve than in analytic methods, the estimates are progressively more accurate and, consequently, much closer to the real activity in the object. Furthermore, in the backprojection method, the value of one projection is assumed to be the integral along the respective LOR, forcing all the corrections to be applied before the reconstruction. As for the iterative methods, there is the possibility of applying corrections to the data during the reconstruction, or even incorporating anatomical information from previous MRI or CT studies of the patient [39]. Every iterative method follows the scheme on Figure 4.6.

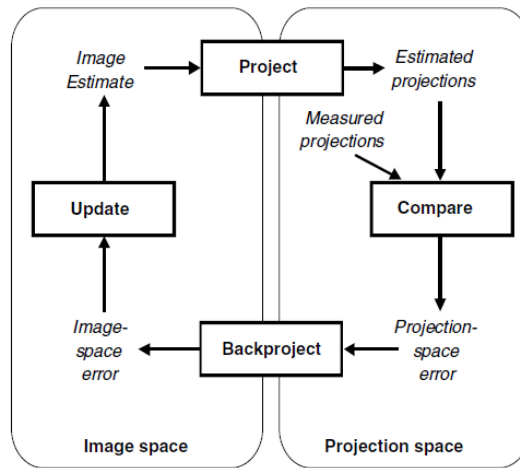


Figure 4.6: Iterative reconstruction process. Figure adapted from [23].

For the Clear-PEM scanner, three different 2D iterative image reconstruction algorithms have been applied: one algebraic – the Algebraic Reconstruction Technique (ART), and two statistical algorithms – the Maximum Likelihood - Expectation Maximization (ML-EM) and the Ordered Subsets - Expectation Maximization (OS-EM). For this work, only the OS-EM was used.

According to Fessler [40] the image reconstruction methods have five components:

1. a finite parameterization of the positron-annihilation distribution, i.e., the measurements taken (Y);
2. a system matrix (A) – a model of the emission and detection process that relates the activity distribution inside the organ (f) with the measurements taken (Y), for example:

$$Y = Af \quad \text{Eq. 4.4}$$

3. a statistical model for how the detector measurements vary around their expectations;
4. an objective function that is to be maximized to find the image estimate;
5. an algorithm, typically iterative, for maximizing the objective function, including specification of the initial estimate and stopping criterion.

Accordingly, for every iterative image reconstruction, the calculation of a system matrix \mathbf{A} is required. Each element of \mathbf{A} (denoted by a_{ij}) represents the contribution of the voxel j (element of \mathbf{f}) in the object to the bin i (element of \mathbf{Y}) in the projection, or, simplifying, each element of the matrix a_{ij} defines the probability of the emitted photons in a certain voxel j had originated a certain LOR i . It is in the specification of \mathbf{A} that the model of the projection process can become as simple or as complex as we require, because the intensity of a projection bin is a weighted sum of intensities of the image voxels [23].

4.4.1. SYSTEM MATRIX CALCULATION

The system matrix represents the physics and the geometry of the emission and detection processes, for that particular system. Hence, when the scanner has a fixed geometry, the system matrix may be calculated only once and stored to be used in all image reconstructions required. However, when the system of detection has a variable geometry, the system matrix must be recalculated every time the geometry is changed.

Independently of the method used to calculate the system matrix, at the end of the calculation, the probabilities need to be normalized. This normalization guarantees that the sum of the probabilities that corresponds to a certain coincidence is always equal to one if the LOR is detectable, or equal to zero if it is undetectable.

There were three methods used in this scanner: the pixel-driven, the ray-driven and the tube-driven method. Only the latter was used for this work, but a small presentation of all three will be made to make comprehension easier. This is a review of the work of Nuno Matela in [28].

4.4.1.1. The Pixel-Driven Method

In this method, each element of the system matrix is determined by the analysis of which LORs can be originated from each pixel. The v coordinate of all detectable LORs that cross a certain pixel j is calculated. Note that only the values of v within the limits of the detector plates will be considered. For each pair (j, v) the value of u is determined with:

$$u = \frac{v(\Delta z - 2z_0)}{\Delta z} + y_0 \quad \text{Eq. 4.5}$$

where y_0 and z_0 are the pixel j coordinates and Δz is the distance between the detector plates. Because the result of this equation is a real value of u , which does not always match the centre of the linogram bin, a correction is made by dividing the probability of occurring a LOR with a given direction, generated in this pixel, by the two nearest bins of u , taking into account the distance between the centre of each bin and the intersection coordinate. This distance returns an indication of how close u is from the centre of the two nearest bins.

4.4.1.2. The Ray-Driven Method

Opposite to the previous method, in the ray-driven method every LOR is analysed to determine from which pixel it could have been originated.

Based on the Siddon method [41], each element of the matrix is defined as the length of the segment of the LOR i inside pixel j . Firstly, the coordinates of the intersections between the LOR i and the vertical lines of the pixel lattice are determined analytically in LOR units (defined as fractions of the LOR's total length), and then arranged as a vector $\vec{\alpha}_y$. The procedure is repeated with the horizontal lines of the lattice, and the vector $\vec{\alpha}_z$ is created. The following step is the merge of the two vectors, where all the coordinates are sorted. The difference between two consecutive coordinates is calculated and the vector $\vec{\alpha}$ created.

The component α_j of this vector is defined as the probability that the LOR had been originated in a certain pixel that can be localized in the FOV by the coordinates m_j and n_j , calculated using the following equations and where y_1 is the coordinate in the lower detector.

$$m_j = \frac{y_1 + \Delta y \frac{\alpha_j + \alpha_{j-1}}{2}}{d} \quad \text{Eq. 4.6}$$

$$n_j = \frac{\Delta z (\alpha_j + \alpha_{j-1})}{2d} \quad \text{Eq. 4.7}$$

The procedure is repeated for all possible LORs and the results presented as a matrix.

4.4.1.3. The Tube-Driven Method

Unlike both previous methods, where each detected coincidence is described as a LOR, in the tube-driven method – an evolution of the ray-driven method – a tube of response (TOR) is considered instead, connecting the surfaces of the two activated crystals. This alternative approach was considered since the detectors are not small enough to allow a precise calculation of the point where each photon entered the crystal. This tube will include all the possible LORs between the two detectors. Hence, instead of calculating the

length of the several segments, the a_{ij} elements are determined by the exact calculation of the area of intersection between each TOR i and each pixel j . The area is calculated using the same procedure presented for the ray-driven method, but now only applied to the left limit of the tube, L , which has a base with the same width of the pixels. From this, there are only three possible types of intersection: a trapezium (Figure 4.7(a)), the entire pixel except one or two triangles (Figure 4.7(b)) or only one triangle (Figure 4.7(c)).

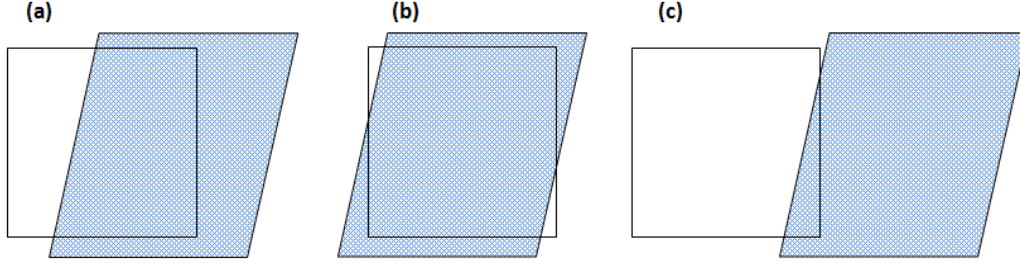


Figure 4.7: Possible intersections between a TOR and a pixel: (a) a trapezium, (b) the entire pixel except one or two triangles, or (c) one triangle.

For the exact calculations of the interaction areas involved in each case, Eq. 4.8, Eq. 4.9 and Eq. 4.10 should be used.

$$A_{(a)}(D, \theta) = h \left(\frac{h \sin \theta + l_{tub} - 2D}{2 \sin \theta} \right) \quad \text{Eq. 4.8}$$

$$A_{(b)}(D, \theta) = h^2 - \frac{2(f^2(\theta) - D^2)}{\sin(2\theta)} \quad \text{Eq. 4.9}$$

$$A_{(c)}(D, \theta) = \frac{(f(\theta) + l_{tub} - D)^2}{\sin(2\theta)} \quad \text{Eq. 4.10}$$

In these equations, $A(D, \theta)$ is the value of the area of intersection between the TOR and the pixel, D is the distance between the centre of the pixel and the central line of the TOR, l_{tub} is the length of the base of the TOR, h is the size of the pixel, θ is the angle between the TOR and an horizontal line and $f(\theta)$ is defined by Eq. 4.11.

$$f(\theta) = \frac{\sqrt{2}h}{2} \cos\left(\theta - \frac{\pi}{4}\right) - \frac{l_{tub}}{2} \quad \text{Eq. 4.11}$$

The set of variables for all the calculations is defined in Figure 4.8.

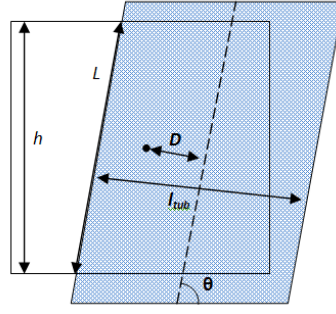


Figure 4.8: Variables used to calculate the area of intersection between the TOR and the pixel.

In all approaches probabilities were normalized to one for each value of j .

4.4.2. THE ALGEBRAIC RECONSTRUCTION TECHNIQUE (ART)

In our image model ($Y_i = A_i f$), each measurement, Y_i , a function of the activity distribution, is a hyperplane where the solution of f must lie. There are as many hyperplanes as projections and the solution of f must belong simultaneously to all, which means the solution will lie in the intersection of all hyperplanes. Still, this assumption will only be valid for noiseless data. Noise can be defined as random, unwanted signal that interferes with the processing or measurements of the desired signal [23].

When noise is present in the acquired data, the assumption that all hyperplanes intercept themselves in a single point is generally not true since each hyperplane will be slightly shifted from its original position. In this situation, we will probably have multiple intersections corresponding to partial solutions, i.e., solutions that satisfy part of the constraints but not all of them. This will introduce a problem to the iterative algorithm since it will not converge to a unique solution, switching cyclically between partial solutions. This problem is solved by the introduction of a relaxation parameter (λ) [28].

The algebraic reconstruction technique, or ART, was applied to medical image reconstruction for the first time by Herman [42], and is one of the possible methods to determine the intersection point of all hyperplanes.

In the ART algorithm to determine f_j , a linogram of an estimate is calculated and a subset (Y_i) of the estimation linograms is compared with the corresponding subset obtained from the measurements by calculating the algebraic difference. In each ART sub-iteration, the activity is updated in order to minimize the difference between these two sets [43].

The numerical expression that represents this procedure is:

$$f_j^{(k)} = f_j^{(k-1)} + \lambda^{(k)} \frac{Y_i - \sum_l a_{il} f_l^{(k-1)}}{\sum_l a_{il}^2} a_{ij} \quad \text{Eq. 4.12}$$

Or, in words, the a_{ij} is the model of emission and detection that corresponds to the probability that a detection Y_i had been originated in pixel j . The relaxation parameter must have a value between 0 and 1, in order to keep the result between the different hyperplanes. By doing so, an underrelaxation of the method will be applied, limiting the update process, which prevents the algorithm from entering in a loop.

High values of the relaxation coefficient, λ , allow fast convergence speed but also noisy reconstruction images, and on the contrary, low values allow smoother images but lower convergence speed. The choice of which to optimize is always made.

4.4.3. THE MAXIMUM LIKELIHOOD - EXPECTATION MAXIMIZATION (ML-EM)

The maximum likelihood – expectation maximization (ML-EM), developed by Dempster [44] and applied for image reconstruction for emission tomography by Shepp and Vardi [45], is often considered the source of the best image reconstruction algorithms. It is an iterative statistical algorithm based on the fact that the best model for the physics involved in the emission and detection of radioactive decay processes is the Poisson distribution.

Following the same principle as ART, the acquired data will be represented on a vector Y , whose element Y_i represents the number of coincidences detected along the direction defined by the LOR i . The number of photon pairs emitted in each voxel j is given by f_j .

The main idea of the ML-EM algorithm is to maximize a likelihood² function, which can be achieved using:

$$f_j^{(k)} = \frac{f_j^{(k-1)}}{\sum_{i'} a_{i'j}} \sum_i \frac{a_{ij} Y_i}{\sum_{j'} a_{ij'} f_{j'}^{(k-1)}} \quad \text{Eq. 4.13}$$

Nevertheless, this method has two major drawbacks: very slow convergence and it is unstable in the presence of noisy data.

4.4.4. THE ORDERED SUBSETS - EXPECTATION MAXIMIZATION (OS-EM)

The ordered subsets – expectation maximization (OS-EM) is usually understood as an accelerated version of ML-EM. Proposed by Hudson and Larkin [46], instead of using

² *Likelihood* is a general statistical measure that is maximized when the difference between the measured and estimated projections is minimized.

simultaneously all values of Y_i to update a new estimation of the activity distribution, the elements of the linogram are divided into subsets. Each reconstructed image update is then performed using only one subset (one sub-iteration)[43]. The process can be described by:

$$f_j^{(k)} = \frac{f_j^{(k-1)}}{\sum_{i' \in S(k)} a_{i'j}} \sum_{i \in S(k)} \frac{a_{ij} Y_i}{a_{ij} f_{j'}^{(k-1)}} \quad \text{Eq. 4.14}$$

where $S(k)$ is the subset to be used in k^{th} image update.

One OS-EM iteration, composed of n sub-iterations, takes approximately the same time as to iterate ML-EM once, yet it consists in n times more updates of the estimated activity distribution.

The problem with the noisy images in the ML-EM remains, but since more updates are performed in each iteration with the OS-EM algorithm than with the ML-EM, the image noises increases earlier with the first method, especially when a higher number of subsets are chosen. Consequently, the choice of the number of subsets must be a compromise between convergence speed and final image noise [28].

Chapter 5.

Sensitivity Correction

This is the first of three chapters that will present the core of this work. In order to clarify the methods used, all the contents will be presented in order of completion. This is a development of Nuno Matela's work [28], who had already applied some of these corrections but without optimization.

5.1. Sensitivity and Detector Gaps

The sensitivity of a PET scanner is defined as the counting efficiency of the system for a known amount and distribution of activity [15]. It is determined by two parameters: the scanner's geometry and the stopping efficiency of the detectors. For a fixed amount of time and with a fixed amount of radioactivity in the FOV, high-sensitivity PET scanners generally produce reconstructed images with improved SNR, due to a reduction in the effect of statistical fluctuations. Furthermore, a high stopping power, i.e., a high attenuation coefficient of the crystal, will reduce the distance the photons travel before depositing all their energy on the detector, also known as depth of interaction, hence reducing the parallax error³ in images [8].

As a result of different angles and lengths of intersection with the crystals, not all LORs will have the same probability of being detected. The probability of absorption of a γ photon by a detector crystal is given by:

$$P_{\gamma} = 1 - e^{-\mu l} \quad \text{Eq. 5.1}$$

where μ represents the attenuation coefficient of the crystal and l is the length of the photon trajectory inside the crystal. As a consequence, a LOR's probability is a result from the product of the probabilities of the two coincident photons that originated it, and is given by:

$$P_{LOR} = P_{\gamma_1} \times P_{\gamma_2} = (1 - e^{-\mu l_1}) \times (1 - e^{-\mu l_2}) \quad \text{Eq. 5.2}$$

³ Parallax error is the result from the uncertainty of the DOI: When a photon interacts within a detector and the depth of interaction is not recorded, it is assumed the annihilation event occurred along a line of response originating at the front of the detector, mis-positioning the event.

All the image reconstruction methods previously presented assume that there is a homogeneous acquisition of the radiation throughout the detectors, i.e., all the LORs have equal probability of being detected, which was just proven to be wrong. Moreover, the fact that the detector plates are composed of a series of small crystals, with frontend electronics, all assembled together instead of only one crystal that covers the whole surface, creates small gaps between the crystals where there is no detection. A representation of part of the detector's head can be seen on Figure 5.1, where the dimensions of said gaps are shown.

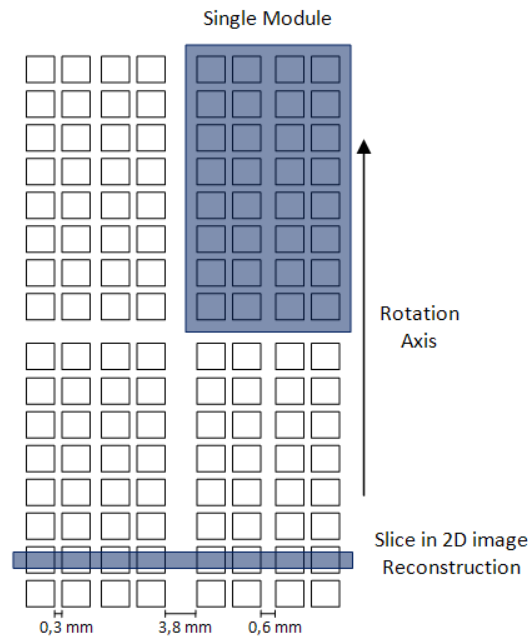


Figure 5.1: Representation of four Clear-PEM modules, with emphasis on the gaps between the crystals.

Resulting both from the different probabilities of LOR's detection and from the presence of detector gaps, there will be a different sampling in different regions of the FOV. This means that in two different regions of the FOV with the same activity the scanner might detect different amounts of radiation. One other reason contributing to this disparity is the number of LORs that can be detected for one event, depending on its position in the FOV. As exemplified in Figure 5.2, the central region of the FOV is covered by an elevated number of LORs, whereas the periphery is seen by only a few. This fact contributes largely to the variation of sampling throughout the FOV.

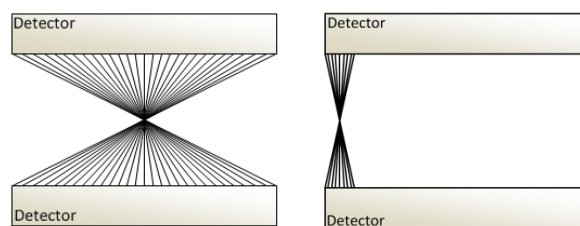


Figure 5.2: Different number of LORs is detected, depending on the position of the event.

In order to compensate for this lack of homogeneity in the sampling, some sensitivity corrections need to be applied to the acquired data.

In this work, two possible correction methods were studied: a method based on the planar source acquisition and the analytic method based on system matrix calculation.

5.2. Correction Based on the Planar Source Acquisition

To understand the regions where the sensitivity of the scanner was compromised, the first approach to the sensitivity correction was focused on the acquisition of a planar homogeneous phantom, parallel to the detectors surface. The fact that the phantom is completely homogeneous, but the data collected from the acquisition is not, gave a good indication of where the heterogeneities were.

Applying this information for data acquisition allowed dividing the measurements from the less sensitive areas in the planar phantom by a lower factor and the more sensitive regions by a higher factor, thus compensating the difference in the sampling.

In this pre-clinical phase, trial acquisitions were made first with a homogenous cylindrical phantom and later with patients. The data was used for image reconstruction and sensitivity correction studies.

5.2.1. PHANTOMS USED

5.2.1.1. Planar Source

The first acquisition studies in a pre-clinical environment took place in January of 2009, after the prototype was assembled at the IPO - Porto. For normalization studies, a ^{68}Ge planar source, a mainly positron emitter radionuclide, with an active region of $16 \times 18 \text{ cm}^2$ and an activity of 18.5 MBq , was acquired for 4 hours at 0° (parallel to the planar detectors). A picture of the phantom taken during acquisition can be seen in Figure 5.3.



Figure 5.3: Picture of the planar source during its acquisition in the Clear-PEM prototype.

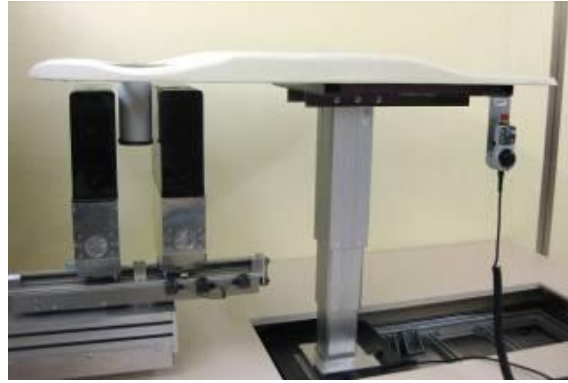
5.2.1.2. Cylindrical phantom

As a breast substitute for the first reconstruction studies, a ^{68}Ge cylindrical phantom was used. With a 105 mm diameter, 158 mm height and an activity of 37 MBq, four one hour-long acquisitions were made, each with a 45° shift (0°, 45°, 90°, -45°). Due to the cylinder dimensions, the two planar detectors were set 150 mm apart for the acquisition. A time window of 15 ns and an energy window of 350 – 700 keV were used (more on these will be explained in the following chapters).

Pictures of the phantom (Figure 5.4 (a)) and the phantom in the prototype during acquisition (Figure 5.4(b)) are shown below.



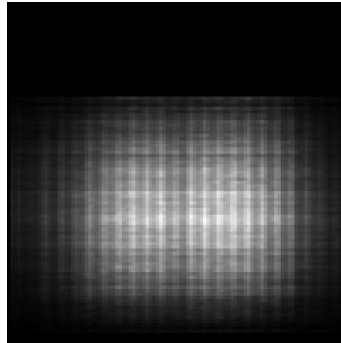
(a)



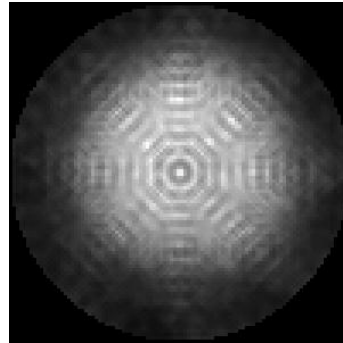
(b)

Figure 5.4: (a) ^{68}Ge cylindrical phantom. (b) Picture of the phantom inside the support used for the acquisition.

Figure 5.5 shows the result of the image reconstruction of the phantom without corrections.



(a)



(b)

Figure 5.5: Image reconstruction of the cylindrical phantom without sensitivity corrections in the (a) yz and (b) xy planes.

5.2.2. THRESHOLD DEFINITION

After the acquisitions, the data was organized in list-mode files and rebinned into linograms using the SSRB method.

At this point, the data entered a process of sensitivity correction, where, as it was said before, the number of LORs that is stored in a linogram bin (*lino_original*) is divided by a correction factor obtained from the planar acquisition (*lino_planar*). This factor is given

by the ratio between the measurement of the corresponding bin and the maximum value in the planar acquisition ($\max(lino_planar)$), as shown in Eq. 5.3. This way, the factor is completely adjusted to the range of values of each acquisition.

$$lino_corrected(u, v, w) = \frac{lino_original(u, v, w) \times \max(lino_planar)}{lino_planar(u, v, w)} \quad \text{Eq. 5.3}$$

However, when the value of the planar source is too low (due to acquisition times not long enough), this division can either be impossible (if the value is exactly zero) or result in an excessively high corrected value ($lino_corrected$). The result of the presence of these values in the reconstructed image is the existence of high intensity pixels, i.e., extremely bright pixels. In order to prevent this problem, a restriction was implemented in which all the bins that present low counts on planar acquisition are divided by a lower factor.

$$\text{if } lino_planar(u, v, w) > threshold \times \max(lino_planar) \quad \text{Eq. 5.4}$$

The denominator of the condition in study is then substituted by a threshold value that not only eliminates the presence of the detector gaps, but also reduces the appearance of the bright noise. This threshold is also multiplied by the maximum value of the planar acquisition, remaining commensurate with each acquisition.

$$lino_corrected(u, v, w) = \frac{lino_original(u, v, w)}{threshold} \quad \text{Eq. 5.5}$$

The threshold should be defined by the highest SNR that corrects the presence of gaps, since, theoretically the image with the highest SNR would be the most homogenous. However, if the defined threshold is too low, all values will pass the starting condition and enter Eq. 5.3, and as a result the gaps will not be corrected. In addition, the number of bright pixels will increase. On the other hand, if the threshold is too high, few will enter the condition, meaning that all the measurements will be divided by the threshold, creating a falsely homogenous image. The solution is to compromise by choosing the minimum possible value.

Additionally, to help reduce this noise, which is very common in the extremities of the linogram as a result of the low activity measured in these areas, due to the physical limits of the detectors, another correction was made. Following what was already implemented for the x coordinate, the first and last bins of each slice in the y direction were erased. Also, to avoid the reconstruction of slices with a small amount of counts, which

would inevitably come out as noise, a minimum was imposed for the number of counts per slice.

This algorithm was developed and implemented in IDL.

5.2.3. STUDIES IN THE CYLINDRICAL PHANTOM

In this work, one of the main concerns was the homogeneity of the image, so one of our goals was to find a threshold that maximized the signal-to-noise ratio (SNR), which is given by:

$$SNR = \frac{\text{Average}}{\text{Standard Deviation}} = \frac{\text{Average}}{\sqrt{\text{Variance}}} \quad \text{Eq. 5.6}$$

The variance and the standard deviation are good estimates of the image homogeneity, since the variance is the measure of the amount of variation of all scores for a variable.

The sensitivity correction was applied testing each one of the thresholds and creating a new linogram that was subsequently reconstructed using the OS-EM 2D algorithm, with 4 subsets and 10 iterations.

For the definition of the threshold many values were considered. The observation of the linograms as of the reconstructed images was very important, since it was taken to a maximum detail, trying to realize when the gaps would disappear.

Threshold analysis began with values of the order of magnitude of 10^{-4} . After the first tests, we soon realized that these were too small and were not contributing to improve the images' quality. Thus, we decided to proceed the study with thresholds of one order of magnitude higher (10^{-3}).

The research for the best value occurred in two different stages of the reconstruction process, first evaluating the result of image reconstruction and then taking a step backwards and analysing the linograms.

5.2.3.1. Reconstruction Assessment

After the image reconstruction, each image was studied with the help of *ROI Studio*, one of the applications of the image visualization and data analysis software *Quasimanager*, developed within the Clear-PEM project. A region of interest (ROI) was defined, allowing some statistical analysis, such as average, variance and maximum value. One ROI was drawn for each of the three orthogonal planes (yz, xz and xy) of the reconstructions, as represented in Figure 5.6, and these same ROIs were used for the different thresholds, to grant accurate comparisons between the results.

To facilitate the comprehension of the PEM results by physicians, the reconstructed images ought to be presented in an inverted grey scale, following the typical x-ray mammography colour scale. However, for some of the studies developed in this work, as for the presence of the bright noise, various images will be presented in a direct grey scale.

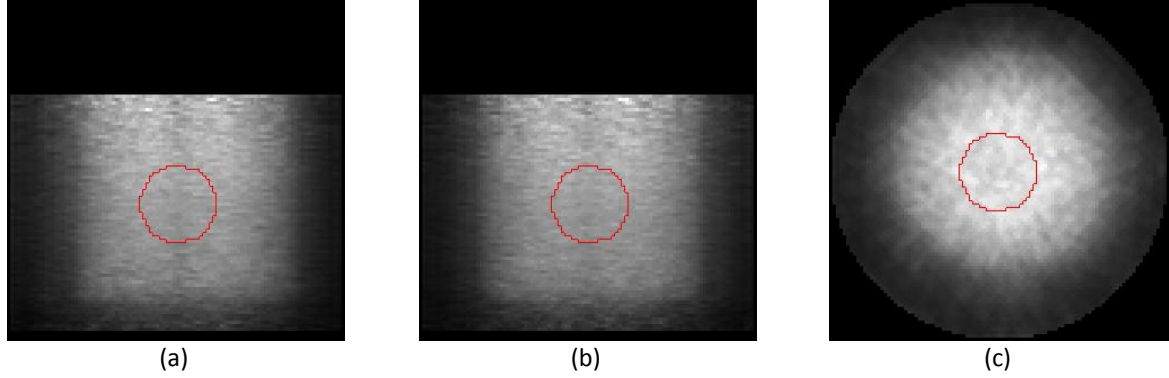


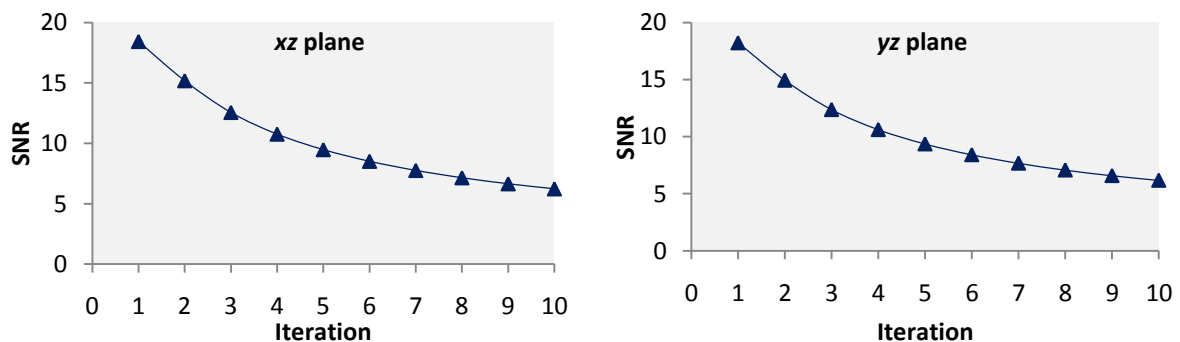
Figure 5.6: Representation of the ROIs used in the study for (a) yz , (b) xz and (c) xy views.

The software *Quasimanager* was of great utility to visualise the images and draw the ROIs, however it would not be practical to analyse all the ROIs, one by one. For that reason, the statistical data was extracted from the images with the help of scripts developed in IDL and organized into plots.

As a result of the similarities presented between the yz (Figure 5.6(a)) and the xz (Figure 5.6(b)) views, in some cases only the results of the first plane will be presented. In fact, some studies will only cover the xy view (Figure 5.6(c)).

Several studies were made with the collected data. The first step was applying the ROIs presented in Figure 5.6 to slice 50 of all iterations for all thresholds. The 50th slice was chosen for belonging to the centre of the FOV and hence having a high number of counts. The resultant information was plotted by threshold and also by iteration.

With the intent of choosing which iteration to study, we started by plotting the SNR values as a function of the iteration number. Due to the considerable amount of data and the similarities between the results, we opted to present only one of the threshold results, which represents the common behaviour (Figure 5.7).



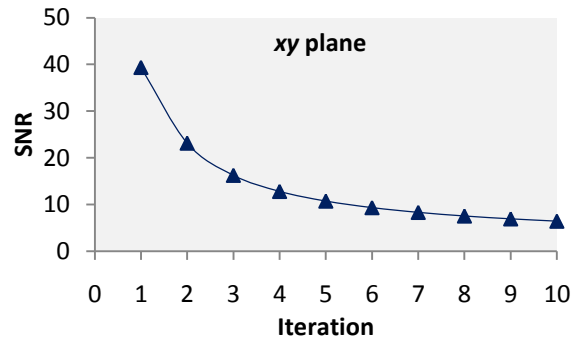


Figure 5.7: SNR values obtained for the 50th slice of the xz, yz and xy plane of the cylindrical phantom, with a 0.001 threshold, during 10 iterations.

As previously explained, the reconstructions with OS-EM tend to gain noise very fast. Since the rise of the noise is correlated with the decrease of the SNR values, the consistency of the shapes of the curves for all planes was expected. Additionally, since the maximum of the SNR is achieved on the first iteration, a compromise between the convergence and the image noise can be found by stopping the reconstruction in its early iterations (second or third) and have good results. For extra confirmation, we present the cylinder image reconstructed with the same sensitivity correction threshold, from the 1st to the 10th iteration, where it is visible the degradation of the image throughout the iterations as a result of the increasing noise. The iteration selected was the 3rd.

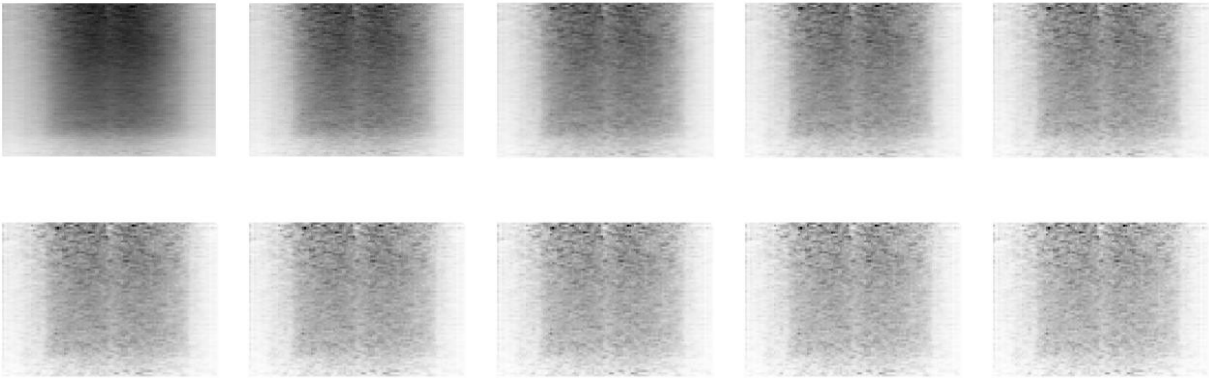


Figure 5.8: Images reconstructed with OS-EM 2D from the 1st to the 10th iteration, with the same sensitivity correction threshold.

The next step was comparing all the thresholds on the same iteration. New plots were made for the same slices studied before, but this time the goal was to find which threshold granted the highest SNR.

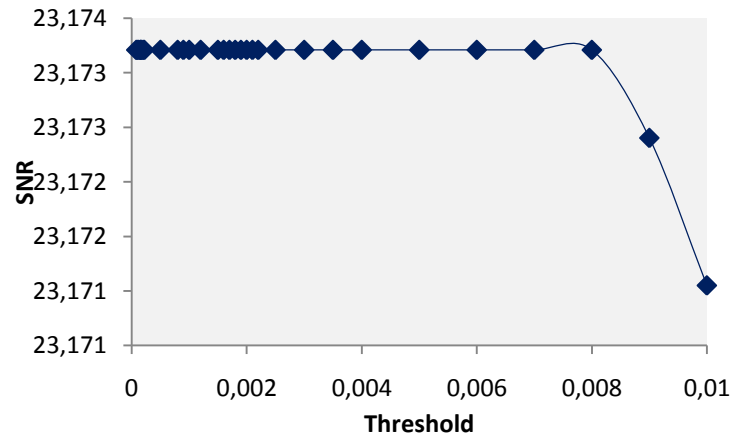


Figure 5.9: SNR values obtained for the 50th slice of the xy plane of the cylindrical phantom after 3 iterations.

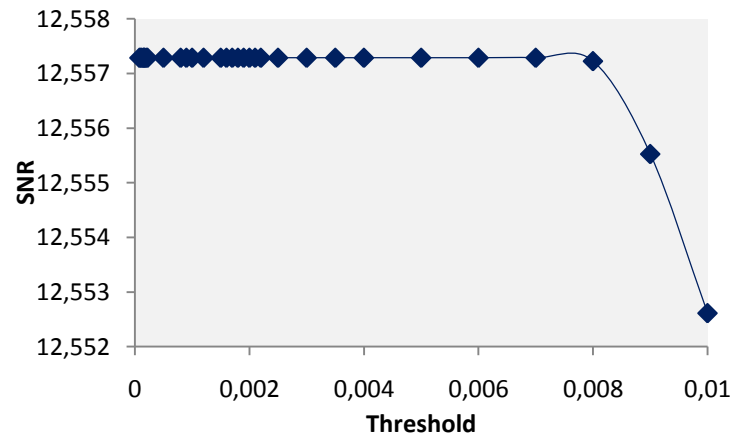


Figure 5.10: SNR values obtained for the 50th slice of the xz plane of the cylindrical phantom after 3 iterations.

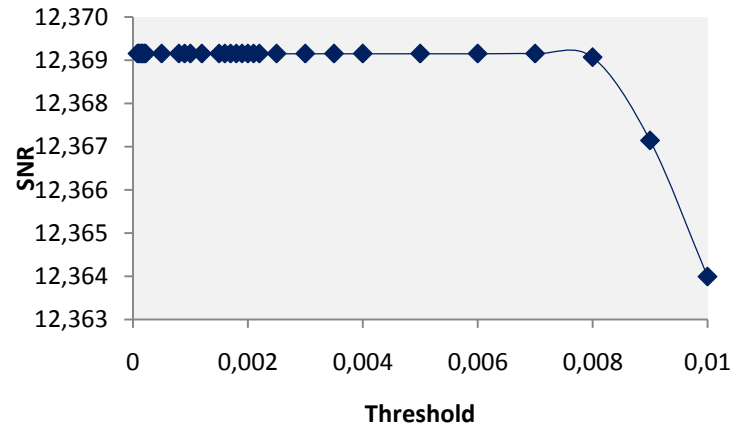


Figure 5.11: SNR values obtained for the 50th slice of the yz plane of the cylindrical phantom after 3 iterations.

All three plots are very similar, presenting constant SNR values for all the thresholds below 0.008. This means that, above this value, the noise will deteriorate the reconstruction results, and for this reason 0.008 was established as our upper limit for the threshold. The fact that these are central slices might have influenced our results, since the central slices are exposed to a much wider range of detectable LORs, thus presenting a much higher number of counts in this region of the FOV than in the periphery. So the next choice was to

try to find a more peripheral slice, which had less counts and thus some fluctuation on the SNR results. Most of the slices behaviour was similar to the presented on the previous plots, though slice 72 presented some variations and for that it was chosen.

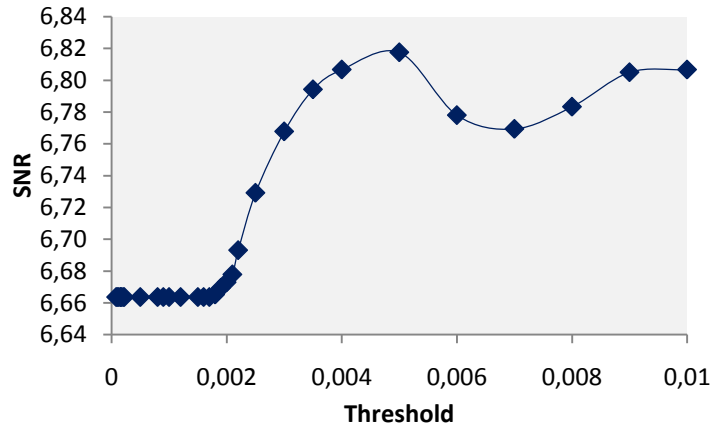


Figure 5.12: SNR values obtained for the 72nd slice of the xy plane of the cylindrical phantom after 3 iterations.

Two facts distinguish this plot from the previous: the first is the clear peak achieved for a 0.005 threshold, and the second is the significant difference in the scale of the SNR values. The fact that this is a noisier slice clarifies the decrease of the SNR. Not only it has more noise than the central slices, the fact that it is a lot closer to the top-end of the cylinder will result in less acquisition of activity, decreasing the number of counts and hence the SNR.

Still, a small consideration needs to be made. The fact that this top slice was one of the few that presented fluctuations, suggests the possibility of inconsistencies on the phantom itself. Since no study was done at the time, there is no way to confirm this chance.

5.2.3.2. Linogram Assessment

We proceeded for a different line of work and decided to study the presence of the gaps directly on the linograms, as can be seen on Figure 5.13.

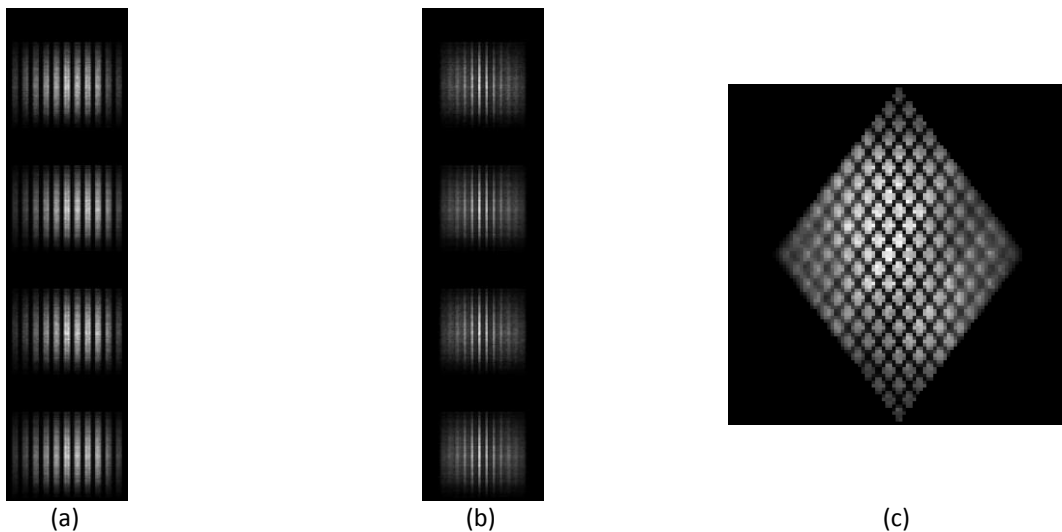


Figure 5.13: Linograms of the cylindrical phantom acquisition without sensitivity corrections for (a) yz , (b) xz and (c) xy planes.

Following the same principle used on the reconstructed images, we decided to study the SNR in ROIs of the data. However, this process has one drawback. The linogram files used for image reconstruction are the result of four simple linograms, one for each projection. As can be seen in Figure 5.13 (a) and (b), for the planes yz and xz the linograms are just brought together, without any kind of correlation, making it impossible for us to analyse that data. The fact that they are actually summed in the xy plane (Figure 5.13 (c)) permits the *ROI Studio* in *Quasimanager* to read the data and analyse it. A new ROI was designed (Figure 5.14) and, again with the help of IDL scripts, the data was processed and plotted.

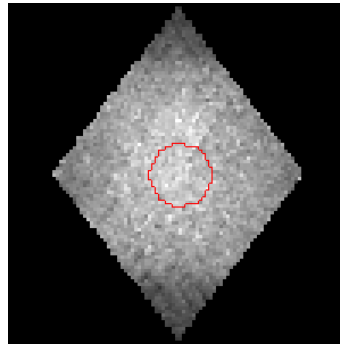


Figure 5.14: Representation of the ROI drawn in the linograms.

One in every ten slices were analysed, but the information retrieved was again inconclusive. Once more, for some slices the SNR value was constant for all the thresholds.

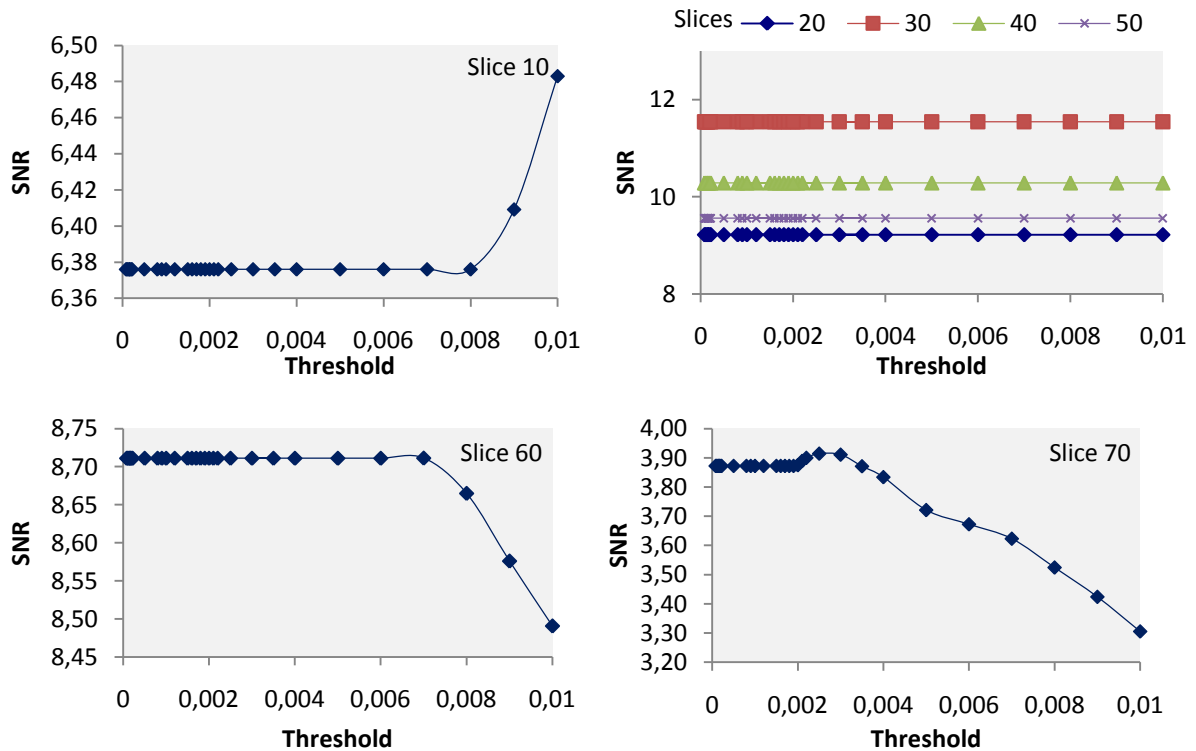


Figure 5.15: SNR values obtained for a ROI of the xy plane of the cylindrical phantom linogram.

For these results it is noticeable that the highest SNR was achieved on the 30th slice. The unusual behaviour of the 10th slice is the direct result of the small number of counts on the first slices. According to the results of the 60th and 70th slices, the upper limit of the threshold should be, respectively, 0.007 and 0.0025. Again, note that these are the noisiest slices. As for all the other slices (20th, 30th, 40th and 50th) the SNR came out as constant throughout the threshold variation, leading to consider yet another study.

One of the inconveniences of evaluating ROIs is that the presence of a small number of elements, such as the null pixels, vanishes within the others. A profile, on the other hand, only evaluates a line, hence is more sensible to fluctuations.

The last of the studies based on the planar acquisition is the profile assessment. Profiles were drawn in the linograms as shown in Figure 5.16.

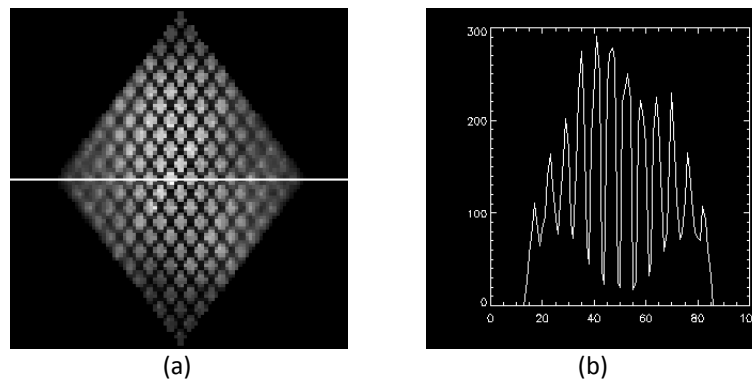


Figure 5.16: Representation of a profile analysis in an uncorrected linogram.

In Figure 5.16 (a) we can see the profile drawn in the centre slice of the linogram and in Figure 5.16 (b) the profile measured. Note that, especially on the centre, the presence of gaps is easily noticed, because the number of counts drops abruptly. By comparison with a corrected linogram, the difference is visible (see Figure 5.17).

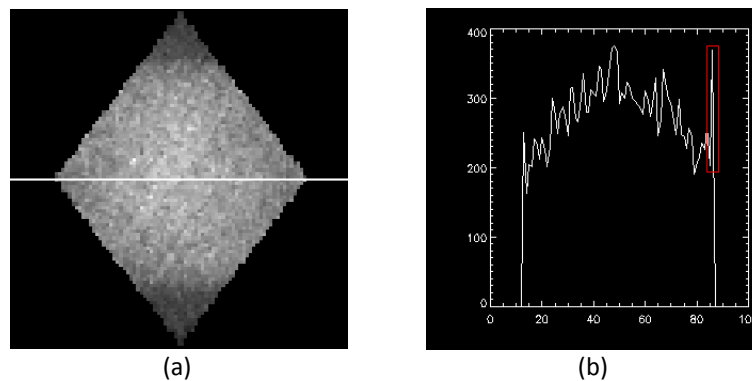


Figure 5.17: Representation of a profile analysis in a corrected linogram with a 0.002 threshold.

This profile (Figure 5.17 (b)) is also interesting because of the presence of a bright pixel. The peak on the right end of the profile shows that, probably, the threshold used was too low. That problem will be addressed further on in this chapter. Analogously to the ROI evaluation, the SNR was calculated considering the voxels crossed by the profile. The central profile of the linograms was evaluated for one in every ten slices.

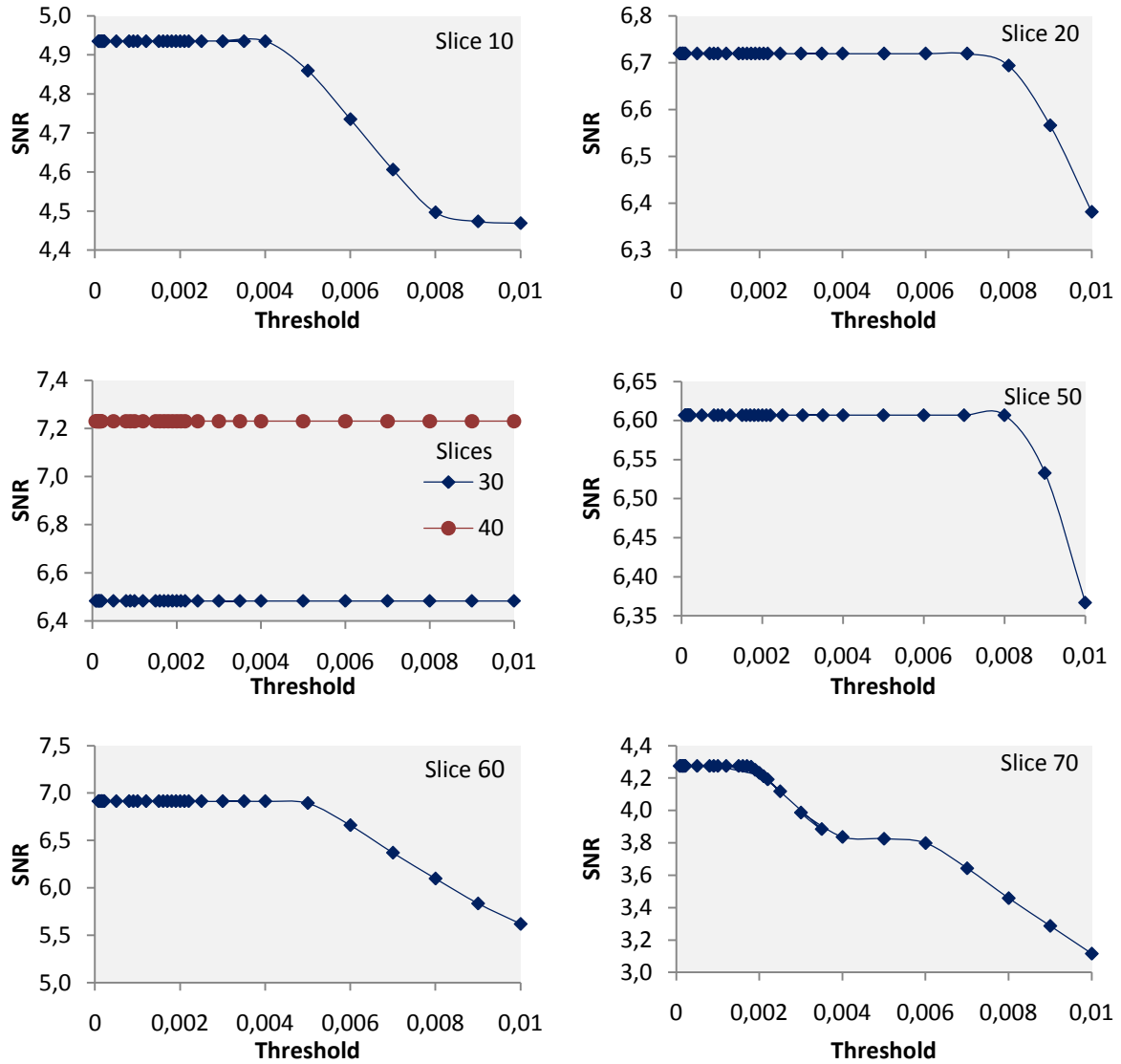


Figure 5.18: SNR values obtained for a profile of the xy plane of the cylindrical phantom linogram.

In this case, the slice with the highest SNR was the 40th. Again, the results obtained were inconclusive. Each slice presented a different threshold, except for the 30th and 40th slices, for which the SNR remained constant for all the thresholds. The lowest result, 0.0017, was acquired on the 70th slice, and the highest was 0.008, for the 50th slice. In between, we had 0.004, 0.005 and 0.007 thresholds for the 10th, 60th and 20th slices, respectively.

For being the most feasible, the profile analysis was later repeated for the data from a new acquisition of both phantoms.

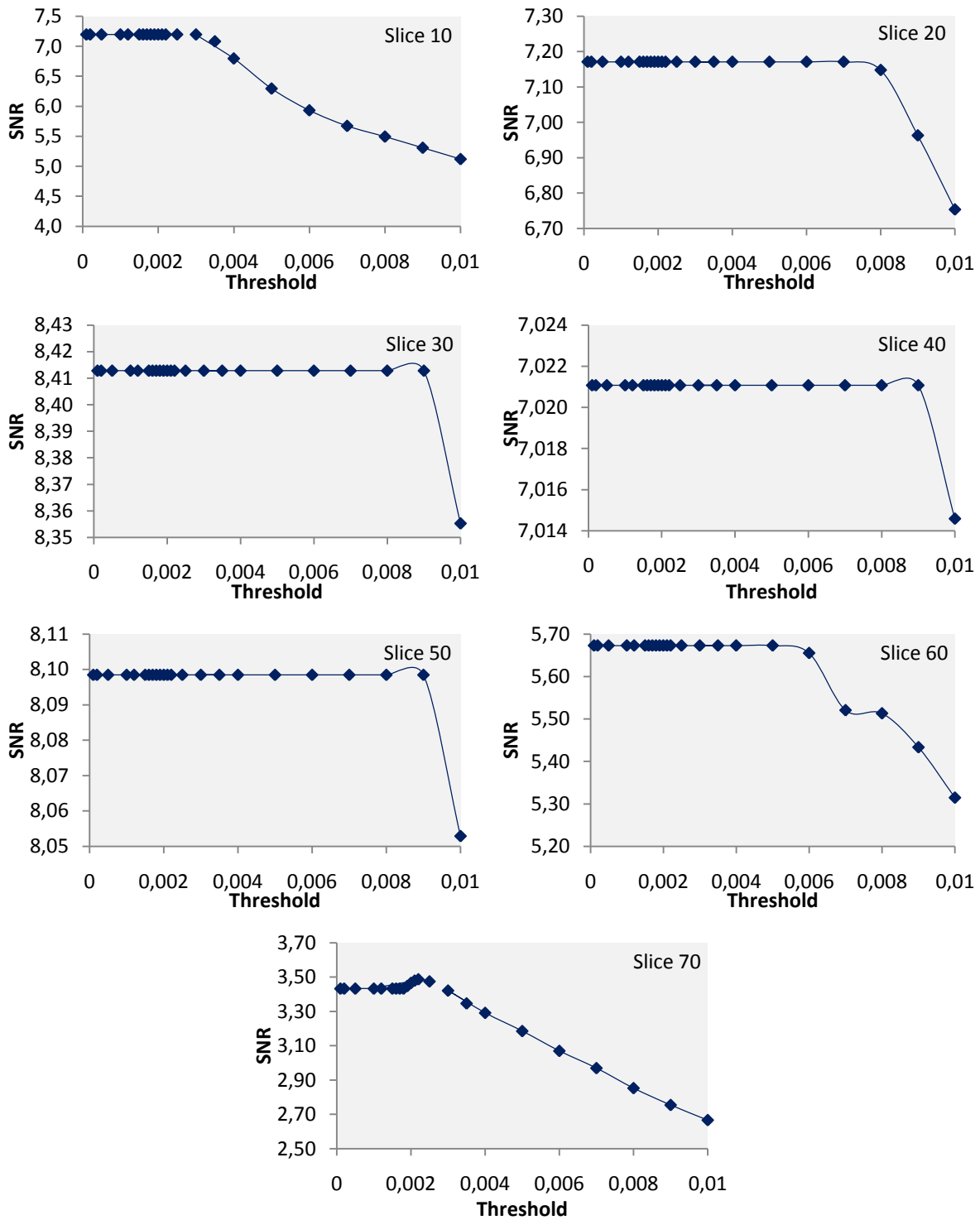


Figure 5.19: SNR values obtained for a profile of the xy plane of the cylindrical phantom linogram.

Once again the results are not clear and do not point to an obvious solution for our problem. Most of the slices present constant values for all thresholds smaller than 0,008. In slice 60 the value 0,005 shows up again. The fact that the thresholds for 10th and 70th slices are so close together (0,002 and 0,0022) could point towards a possible final value, however, the fact that they are rather small values might discourage their choice.

All the conclusions will be presented at the end of this chapter.

5.2.4. VALIDATION WITH CLINICAL DATA

During the course of this work, the first group of pre-clinical patients was examined. Five women, already injected with the radiopharmaceutical for a whole-body PET/CT exam, were asked to take place in our study.

The reconstructed images of the clinical patients were examined with the intent of pursuing the search for the best threshold, this time with breast tissue.

Unfortunately, the second clinical case had some problems during the acquisition, so we were left with four to examine.

For clinical patients 1 and 4, four 5 minutes long acquisitions were made, whereas patients 3 and 5 only had two perpendicular acquisitions, 5 minutes each. The detectors were 150 mm apart for all four exams. A time window of 8 ns and an energy window of 400 – 700 keV were used.

Following what was done for the cylinder, all the data was reconstructed with the OS-EM algorithm, with 4 subsets, and 3 iterations. To choose the best iteration, the standard deviation and the number of counts of the second and third iterations was analysed. With a lower standard deviation value, which stands for a less noisy image, and a slightly elevated number of counts, the second iteration became our iteration choice for the rest of the studies.

The reconstructed images are presented in Figure 5.20 and Figure 5.21.

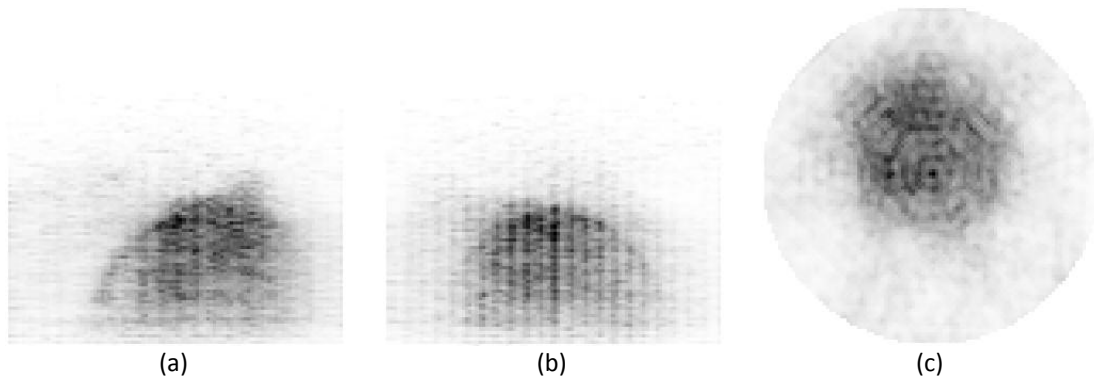


Figure 5.20: Image reconstruction of the first clinical case in the (a) yz , (b) xz and (c) xy planes, without sensitivity correction (reverse grey scale).

As can be seen in Figure 5.20, the gaps' presence is very noticeable even after the reconstruction. Yet, unlike the previous studies, the best plane to evaluate the clinical reconstructions is the yz plane (or transaxial plane), where we have a better perception of the shape of the breast.

The corrected reconstructions of the clinical cases are presented in Figure 5.21, for which some of the best results were chosen.

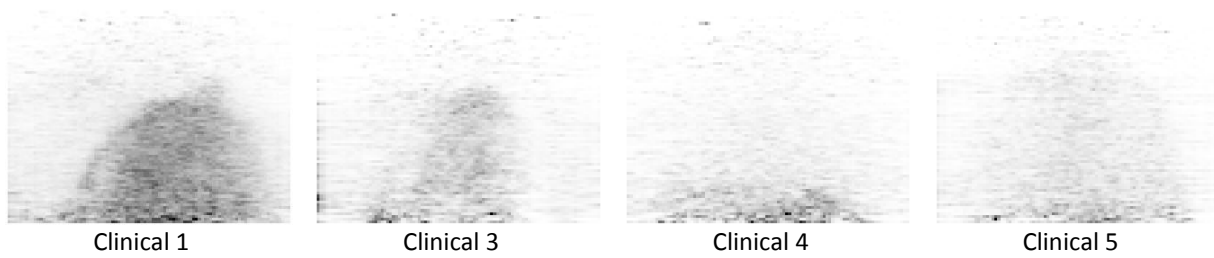


Figure 5.21: Reconstructed images of 4 of the first clinical cases with sensitivity correction (reverse grey scale).

The fact that clinical cases 3 and 5 only had two acquisition positions reflects on the low number of counts, easily perceived from the low visual contrast between the breast and the background. Then again, even with the four acquisitions, clinical 4 does not present a good reconstructed image, probably due to a lower uptake. Since clinical cases 1 and 3 presented the best images, this study was mainly based on these two patients.

With the previous studies we have already proven that the central slices present a regular behaviour, unlike the peripheral ones. Therefore, for this validation it is our goal to find the best threshold that preserves the information in the centre of the FOV while minimizing the presence of high intensity pixels.

Opposite to what was done for the ROI evaluation of the cylinder reconstruction, different ROIs were applied to each clinical case. This way we were able to select and assess the breast area and avoid the background. Additionally, two different types of ROIs were used: a central ROI, with the same goal of evaluating the SNR, and a rectangular one, on the bottom of the image, to quantify the presence of high intensity pixels.

The number of thresholds applied had already been reduced, according to some of the conclusions from the previous section.

5.2.4.1. Image Noise

Using the same method as on the previous section, central ROIs were marked with the aim of evaluating the SNR of the reconstructed image, as shown in Figure 5.22.

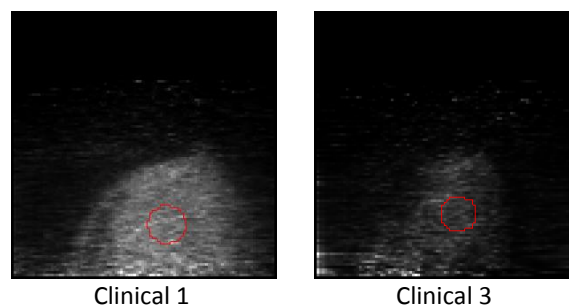


Figure 5.22: Central ROI marked on clinical cases 1 and 3.

At this point, another correction was implemented to the image: random correction. More on this will be explained in the following chapters.

Several slices were analysed, but only two will be presented for each patient, since they represent the general behaviour.

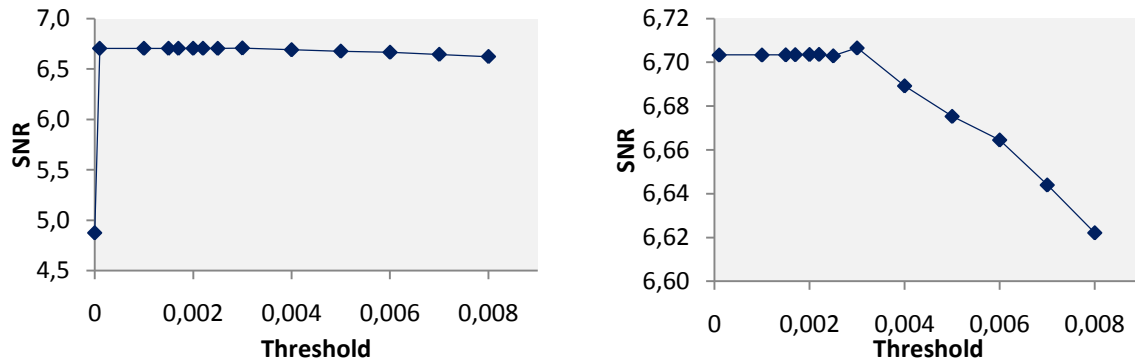


Figure 5.23: SNR values obtained with a central ROI for slice 44 of clinical case 1.

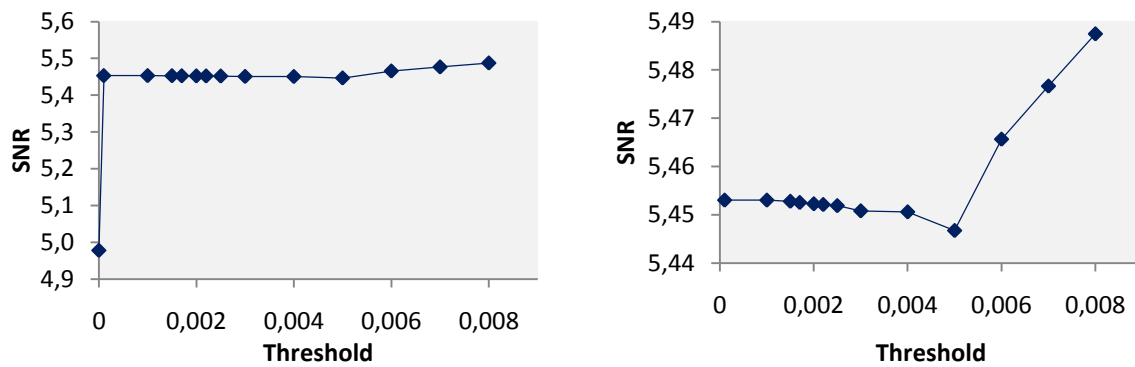


Figure 5.24: SNR values obtained with a central ROI for slice 53 of clinical case 1.

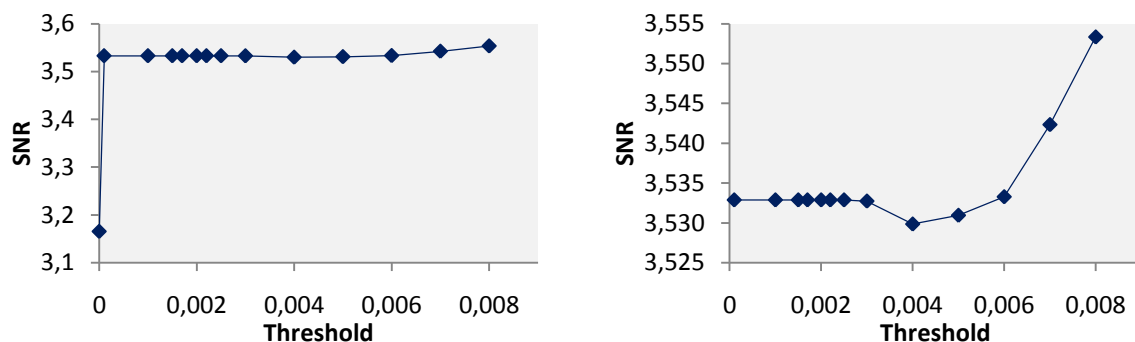


Figure 5.25: SNR values obtained with a central ROI for slice 41 of clinical case 3.

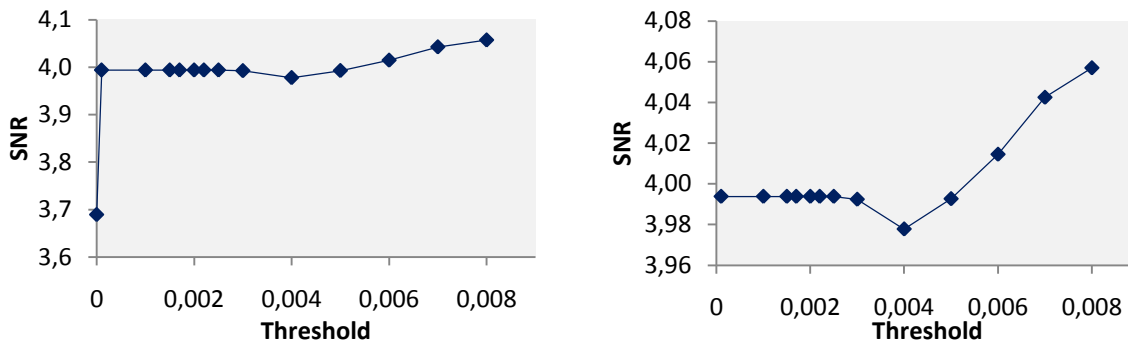


Figure 5.26: SNR values obtained with a central ROI for slice 52 of clinical case 3.

To emphasize the importance of this correction, the SNR values for the non-corrected image reconstruction were added to all the plots. A second plot with only the corrected values presents the results with more detail. The difference between the corrected and uncorrected values is fairly noticeable.

The first of the four plots, slice 44 of clinical 1, is the only one that presents a divergent behaviour. While all other three slices present their lowest SNR value for a 0.004 threshold and then start increasing, on the first case this recuperation does not exist, and the values all go downward. Contrary to the previous study, the best SNR values happen for the biggest thresholds.

Additionally, the fact that clinical case 3 only had two acquisition positions reflects clearly on these results, presenting a low SNR on the centre of the breast. This comparison between SNR values in different clinical cases is only viable since the ROIs applied to both clinical cases have the same size.

Once more, none of the threshold values had a response above the average.

5.2.4.2. Presence of High Intensity Pixels

As it was explained previously, one of the disadvantages of this method of sensitivity correction is the appearance of some high intensity pixels resulting from divisions by low factors. Since the bottom and lateral slices have a lower number of counts, they are more sensitive to the threshold division and prone to the appearance of these bright pixels, which will contribute to further deteriorate the image reconstruction. Not only might they lead to false detections, but the colour scale is seriously altered to accommodate this new value, changing image contrast and hence the real perception of the data. An example is presented in Figure 5.27.

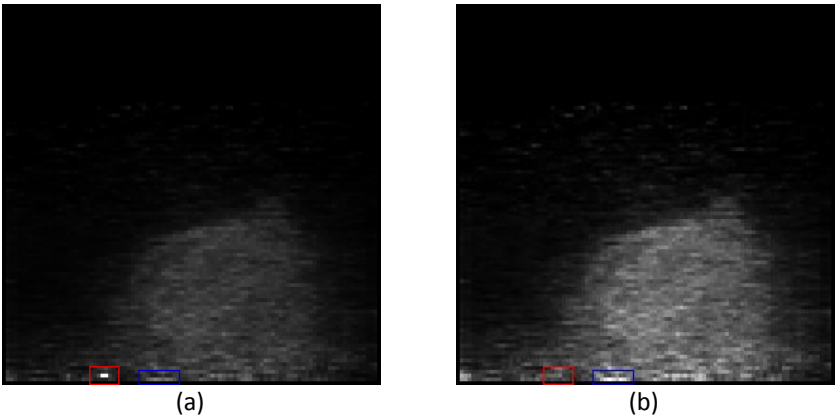


Figure 5.27: Image reconstruction of the same slice corrected with different thresholds.

As can be clearly seen, the image contrast was completely altered by the presence of the high intensity pixel on the red ROI. Even the bright pixels on the blue ROI experienced the same effect, yet presenting a higher value (Figure 5.27 (b)).

Their presence is here evaluated by the application of a rectangular ROI on the bottom of the image (see Figure 5.28). Instead of the usual SNR assessment, the maximum values present in the ROI will be studied.

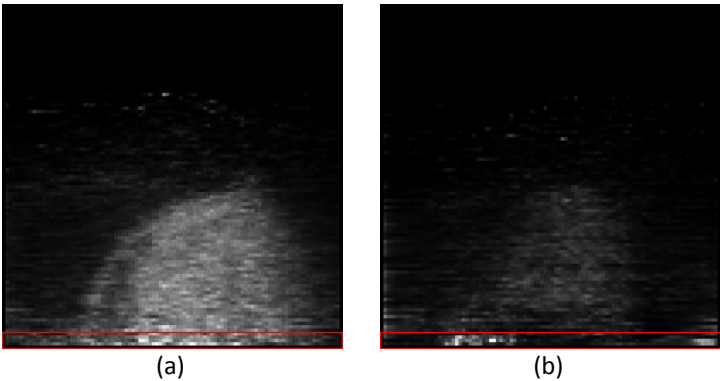
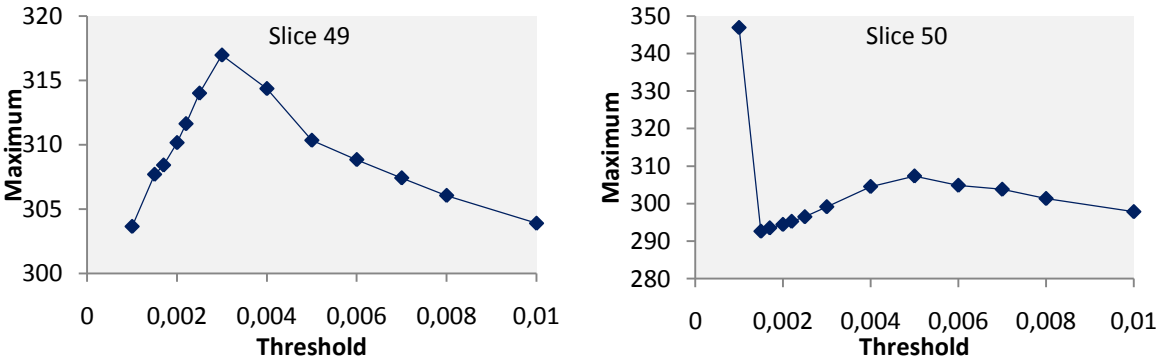


Figure 5.28: Rectangular ROI marked on clinical cases 1 a 3.

Once more, several slices were analysed but only a small representative number will be presented.



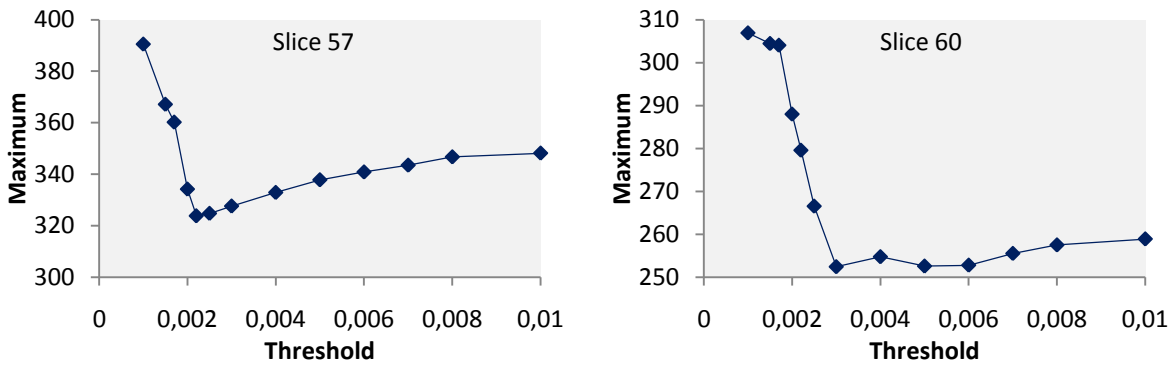


Figure 5.29: Maximum values obtained with a bottom rectangular ROI for clinical case 1.

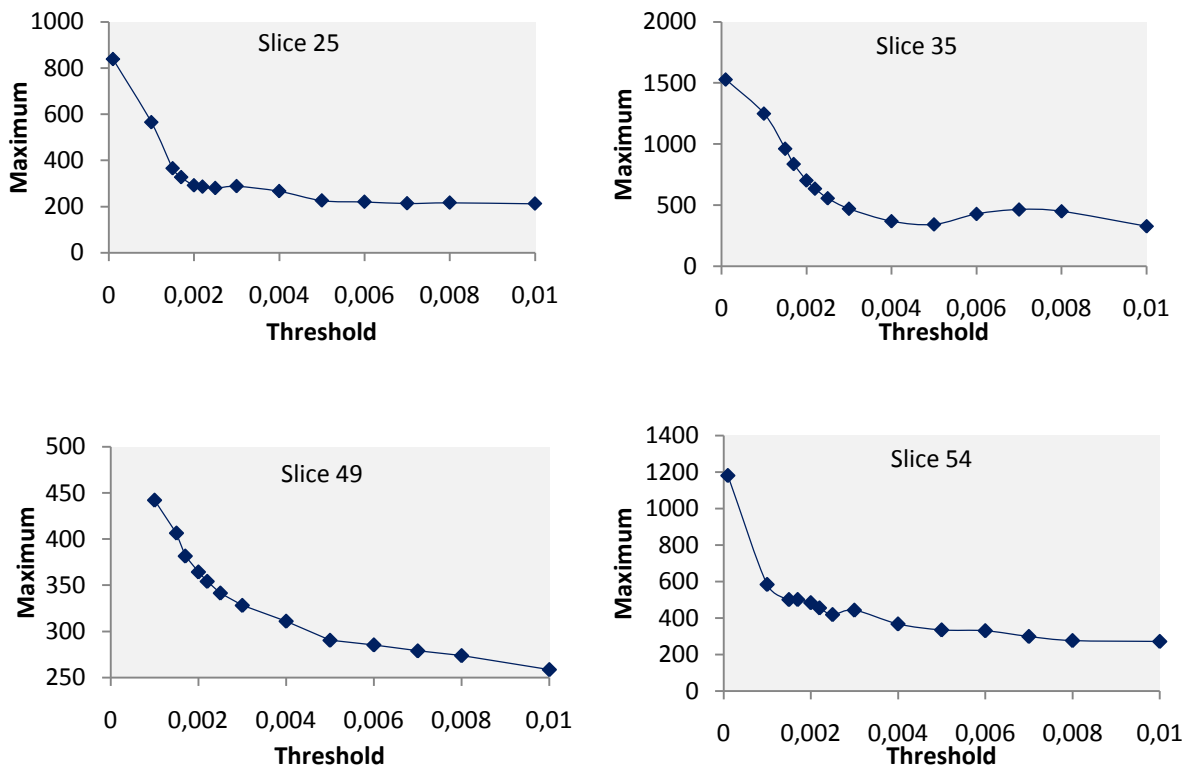


Figure 5.30: Maximum values obtained with a bottom rectangular ROI for clinical case 3.

This time we opted not to present the non-corrected values, since these were not divided by any threshold, hence they were rather low compared with the sensitivity corrected ones. Also, note that we decided not to display the maximum values for the lowest threshold (0.0001), since there was a significant discrepancy with the other values.

For clinical 1 there seem to be two different behaviours. In the first two cases, the values go up to a maximum and then start decreasing, and in the last two the opposite happens, with the values starting to go downwards to a minimum and then increasing again. The minimum value was obtained for the 0.0022 threshold on the third case and for 0.003

on the last case. Still, this last slice presents two more values quite close to the minimum for threshold values 0.005 and 0.006.

On the other side, in clinical 3 there always seems to be a very well defined behaviour, confirming our expectations that the maximum value decreases with the increase of the threshold. In three of the cases the values seem to decrease all the way until the maximum threshold, but on slice 35 the threshold value 0.005 presents the minimum value for the case.

5.2.5. DISCUSSION

In all the different studies, very few were the times where the results were consistent. The ROI analysis of the reconstructed images was clearly the method that presented the worst results, given that below 0.008 all the thresholds produced the same SNR value. This led to the definition of 0.008 as the highest possible threshold.

The next logic step was the examination of the linograms, recurring to the ROI approach. Even though the curve of the SNR started to descend slightly earlier, the outcome remained inconsistent. For a more detailed understanding of the linogram, profiles were used together with an attentive observation of the differences implemented by each threshold. This process was also inconclusive but provided some orientation for the following method.

Lastly, the validation with the clinical data brought, especially in terms of the assessment of bright pixels, some conclusions. The behavioural constancy of the curve, along with the appearance of a repeated value, led us towards a final threshold value: 0.005.

Given that it would be infeasible to study all the possible corrections at the same time, each study is done independently from the others and the result and conclusions taken are applied to the following studies. Consequently, from this point on, all the reconstructions performed in the remainder of this work will be corrected with a 0.005 threshold.

5.3. System Matrix Correction

The analytical modelling of detector gaps was the second method studied to address the sensitivity correction issue. As it was already stated, none of the reconstruction algorithms take into account the different probabilities of the LORs. With this method it would be possible to correct the presence of gaps during the image reconstruction process, by incorporating this information directly on the system matrix calculation.

The first step is to calculate the length of a certain LOR inside the crystals, discarding its path on the adjacent gaps. With Eq. 5.2, by combining the information from the two crystal matrices and knowing the attenuation coefficient of the crystal's material, it is

possible to determine the probability of a pair of photons to be absorbed. The merge of the probabilities of all possible LORs defines an analytical linogram, whose reliability was assessed by comparison with the planar source, and which was incorporated in the system matrix calculation. To better evaluate this method, some image reconstructions took place.

5.3.1. ANALYTICAL LINOGRAM

The software for modelling the detector gaps, *analytsensi.c*, had already been developed in C language by Nuno Matela [28]. However, by the time of completion of his work, the Clear-PEM prototype was not yet assembled, hence some corrections were in order. We will start with a brief presentation of the software developed, followed by the corrections made.

The method employed to measure the length of the LORs inside the crystals and exclude the gaps is exemplified in Figure 5.31.

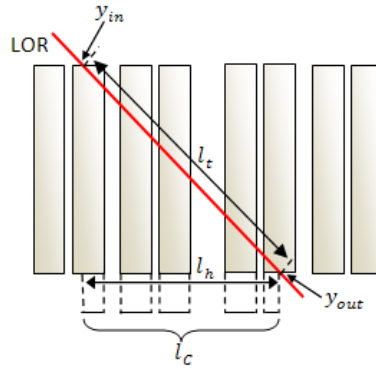


Figure 5.31: Variables definition for lengths of the LORs in a linogram.

Based on the linogram coordinates of each LOR, calculating the entrance and exit point of the LOR in the detector array is the first step, followed by the determination of the length of the LOR inside the detector array (l_t) and its projection over the detector array surface (l_h). Knowing that the z-axis and y-axis are, respectively, perpendicular and parallel to the detector, the entrance and exit points of a LOR in both detector arrays can be calculated by making z equal to the detector top and bottom z-coordinates in the equation that describes the LOR (Eq. 4.3). With the crystal's length in z direction defined as c_{len} , l_t and l_h are easily obtained by using:

$$l_t = \sqrt{c_{len}^2 + (y_{in} - y_{out})^2} \quad \text{Eq. 5.7}$$

$$l_h = |y_{in} - y_{out}| \quad \text{Eq. 5.8}$$

To differentiate the gaps from the crystals, the photon's entering and exit coordinates are used. Summing the length of the gaps between the LOR's entrance and exit,

and subtracting this value from the length of the LOR projected over the detector array surface, results in the part of the length of l_h that corresponds to detector crystals (l_c). Following the same standard, l_i is defined as the length of the LOR inside the detector array i , excluding the gaps. A simple relationship can be established between these lengths with Eq. 5.9.

$$\frac{l_i}{l_t} = \frac{l_c}{l_h} \quad \text{Eq. 5.9}$$

For calculating the width of the gaps, the array *crystcoor*[*i*][*j*], with two columns and 48 rows was created. The first column ($j = 0$), contains the coordinates of the left side of each crystal, and the second column ($j = 1$) the coordinates of the right side of each crystal. Then, a simple subtraction between the beginning of a crystal and the end of the previous one gives us the gap width.

$$gap_{width} = crystcoor[i, 0] - crystcoor[i - 1, 1] \quad \text{Eq. 5.10}$$

Using the same method, the width of a detector block is defined. A detector block is formed by a crystal and the following gap, and can be calculated with:

$$block_{width} = crystcoor[i, 0] - crystcoor[i - 1, 0] \quad \text{Eq. 5.11}$$

After obtaining the detector blocks, $block_{in}$ and $block_{out}$, in which the coordinates y_{in} and y_{out} are, respectively, located, it is possible to determine, through the difference of blocks (N), if the LOR's slope is positive ($N > 0$) or negative ($N < 0$).

$$N = block_{out} - block_{in} \quad \text{Eq. 5.12}$$

The width of the sum of all gaps between the two blocks can also be calculated, whichever is the width of each crystal. To do so, a loop with Eq. 5.13 is used to sum all the gaps' widths.

$$totalgap_{width} += crystcoor[i, 0] - crystcoor[i - 1, 1] \quad \text{Eq. 5.13}$$

However, one consideration needs to be made. The block in which the loop starts depends on whether the slope is positive or not, in order to always cover the crystals array from the left to the right.

For the calculation of l_i and l_c , four different situations, considering whether the LOR enters and exits the detector array in a crystal or a gap, need to be taken into account. More on this can be found in [28].

This method is repeated for all LORs and for both planar detectors, originating l_1 and l_2 values, needed for the linogram formation.

The first change applied to the existing code was correcting the positions of the crystals. The new starting coordinates of the crystals were added to the first column ($j = 0$) of the *crystcoor* array in the *analytsensi.c* file. The declaration of the crystals beginning position is followed by a loop that forces the second column ($j = 1$) to be the value on the first column plus 2 mm – the width of each crystal. The result of this alteration was an increased y_{max} value of 152.5 mm .

To calculate the entrance and exit points of the LORs in both detectors, it is important to consider the distance between the borders of the detectors and the crystals. This distance was defined as 63 mm and added to the calculation of y_{in} and y_{out} , making the equations simpler.

The final modification was the distance between detectors, or z_{max} . This correction has to be repeated every time the distance between the detectors is altered, given that it is one of the program's parameters. For this work it was changed to 150 mm .

After all the adjustments, the program creates a 100×100 array linogram, that we called *linogram.ima*, and that is presented in Figure 5.32.

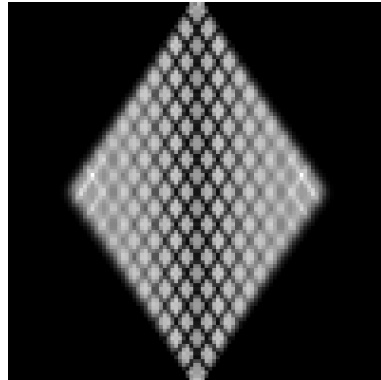


Figure 5.32: Representation of the analytic linogram created.

5.3.2. VALIDATION WITH PLANAR SOURCE

Before the incorporation in the system matrix calculation, the analytic linogram positioning needs to be validated by comparison with the planar source. Normally, because this is a two dimension array, it would be impossible to compare with the planar source linogram, which has three dimensions. To overcome this problem, a new linogram, with the same dimensions of the planar acquisitions, but with the same analytic linogram in every z-

dimension slice, was built with the help of a small IDL script. The linogram was normalized to the values of the planar acquisition for a better comparison.

The creation of this new linogram permitted the use of another *Quasimanager* application, which allows an automatic subtraction of two different volumes. By presenting a high number of counts, slice 27 was the chosen in the planar acquisition. The result is portrayed in Figure 5.33.

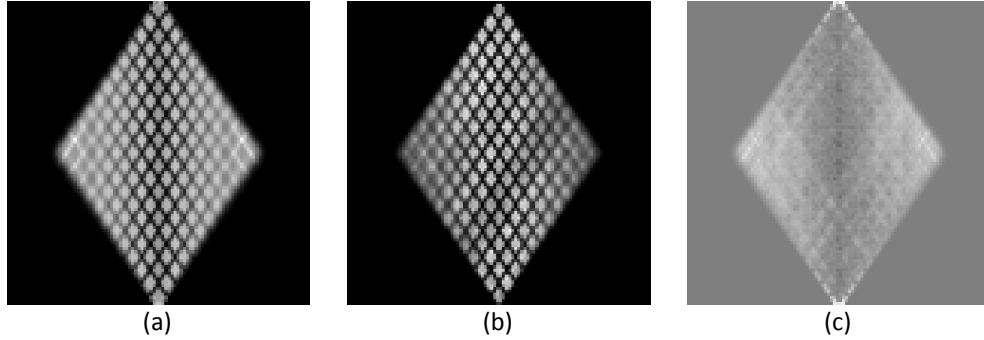


Figure 5.33: Result of difference (c) between the analytic linogram (a) and the planar source acquisition (b).

As can be seen, in the two linograms, the gaps are perfectly aligned, which means that, at least theoretically, the analytic model can be used to replace the planar acquisition. In spite of this, the big difference in the activity is noticeable, mainly due to the fact that the vertical gaps were not simulated.

5.3.3. INCORPORATION ON THE SYSTEM MATRIX CALCULATION

For the last step of this procedure, we went back to the analytic linogram created. The program in which the system matrix is calculated (see 4.4.1) was also developed in C language, and was edited to fit this correction.

The analytic linogram was normalized to a maximum of 1 and then stored in a new array (*lino_analyt*).

In a standard matrix calculation, an array, $mat[h + 10000 w]$ is created, where h stands for the LORs and w stands for the pixels. This array is an alternative to the 10000×10000 two-dimension matrix $[h, w]$, where the probabilities are recorded. Two other linograms are also produced: one that does not take any sensitivity corrections into account, and works as if the planar source acquired was completely homogenous ($lino[h]$), and one that follows Eq. 5.2 and calculates the matrix efficiency, i.e., it calculates the number of times each LOR is sampled, avoiding double sampling ($lino_2[h]$).

In a summarised way, we can say that, first, the matrix is corrected for the double sampling issue (see Eq. 5.14) and then, if $lino[h] > 0.1$, it will be divided by $lino[h]$. The additional correction that we added is presented in Eq. 5.15.

$$mat[h + 10000 \times w] = mat[h + 10000 \times w] \times lino_2[h] \quad \text{Eq. 5.14}$$

$$mat[h + 10000 \times w] = \frac{mat[h + 10000 \times w]}{lino[h] \times lino_analyt[h]} \quad \text{Eq. 5.15}$$

After this implementation, a regular reconstruction, on *Quasimanager*, can be processed, with the only concern that this new system matrix calculation is called instead of the older version.

After the reconstruction the regular analysis of image ROIs occurred. Some of the obtained results are revealed here.

Using the same circular ROI as before, three files will be compared: the cylinder, and clinical cases 1 and 3. For each of the three, one slice was chosen to be compared with an image reconstructed with the classic system matrix calculation and the sensitivity correction previously defined.

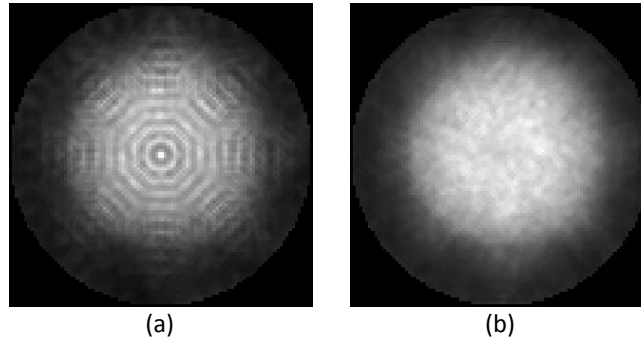


Figure 5.34: Cylinder reconstruction with (a) analytic linogram and (b) the planar source acquisition with a 0.005 threshold.

A simple observation of both results shows that the analytic method is not enough to achieve the same homogeneity as the sensitivity correction script. The same study was done for the clinical cases.

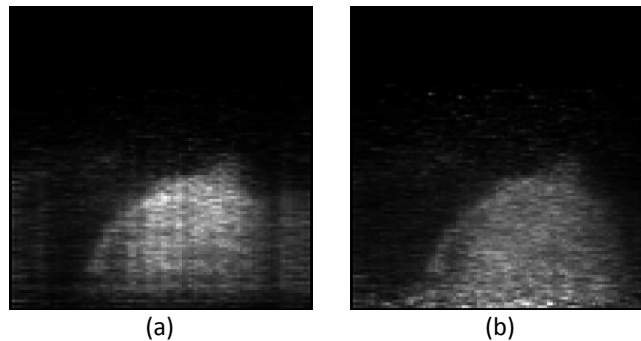


Figure 5.35: Image reconstruction of clinical 1 with (a) analytic linogram and (b) the planar source acquisition with a 0.005 threshold.

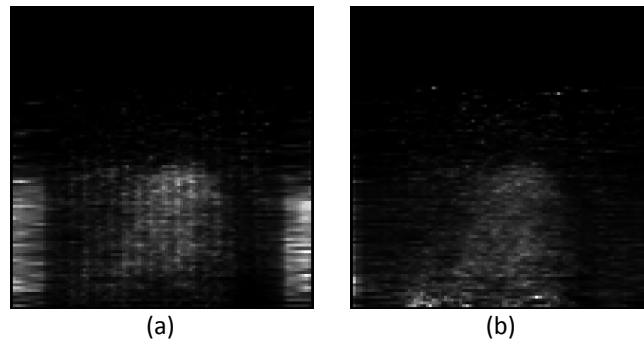


Figure 5.36: Image reconstruction of clinical 3 with (a) analytic linogram and (b) the planar source acquisition with a 0.005 threshold.

The SNR values obtained from the ROI analysis are presented in Table 5.1.

Table 5.1: Comparison between the SNR values obtained with the analytic linogram and the planar source acquisition with a 0.005 threshold.

	<i>Analytic Linogram</i>	<i>Defined Threshold</i>
Cylindrical Phantom	8.62	26.15
Clinical 1	4.63	19.05
Clinical 3	3.72	3.99

As expected, the SNR values for the correction defined through a threshold are higher than the analytical corrections.

Sustaining our previous conclusions, neither the image reconstructions presented, nor the results from the ROI assessment, show any advantage in preferring this method in detriment of the one previously studied. Not only the homogeneity decreased, but the image quality was globally reduced, with a smaller number of counts on the bottom slices, and a vast quantity of highly intense pixels.

Thus, we can conclude that this method is not the best way to achieve good results, hence we will continue to use the correction based on the planar source instead of this analytic correction.

Chapter 6.

Random Correction

The quality of a PET reconstructed image is largely affected by the presence of non-true coincidences. In this chapter, we will illustrate the work done to correct and minimize the presence of random events.

6.1. Timing Window

In PEM, as well as in PET, the simultaneous emission of the two photons, subsequent to the positron annihilation, can occur anywhere within the scanner's FOV. Ideally, both photons should be detected at the same time. However, the fact that the distance travelled by each photon before striking the detectors might not be the same and the fact that there is a time required to process an event before another event can be properly recorded (*dead time*) might compel a slight difference in their arrival time [8, 15]. For this reason, a timing window (2τ) is defined within which the detected events are considered coincidences. As a result, it is possible that two unrelated emitted single annihilation photons get associated as a valid coincidence, these are known as random events (see section 3.2.2). The fact that these events do not carry any spatial information about the activity distribution is a major drawback, ultimately contributing to an undesirable background in the final images, thus decreasing image contrast [15].

The rate of random coincidences (N_R) can be calculated by Eq. 6.1,

$$N_R = 2\tau \times N \times N = 2\tau \times N^2 \quad \text{Eq. 6.1}$$

where N stands for the photon detection rate in each detector (counts per second) and 2τ is the defined timing window. Knowing that the detection rate per detector is proportional to the activity present in the FOV (A), we get Eq. 6.2.

$$N_R = 2\tau \times A^2 \quad \text{Eq. 6.2}$$

We can conclude that the rate of random coincidences is proportional to the square of the activity in the FOV and directly proportional to the coincidence timing window. Consequently, a large timing window results in a sizeable random rate and in an augmented background bias [15]. Given this, a simple way to improve image contrast without compromising signal-to-noise ratio is to prefer a narrow timing window. The optimization of the time window was the object of study of this chapter. Nevertheless, it is important to

point out that the variation of the width of the timing window might affect directly the number of true coincidences measured, resulting in statistical fluctuations.

With the intention of further reducing the presence of random coincidences, a second timing window, with the same width but a delayed input, was implemented. On account of its delay, this new window only measures random events. The counts measured in the second window are a good estimate of the random coincidence rate and it can be subtracted from those measured in the original one, resulting in a random correction. However, it is important to point out that the random correction techniques result in a propagation of noise through the data set and so the image signal-to-noise ratio will be affected [3, 8].

One measurement that has been used to give some insight into the quality of the data is the noise equivalent count (NEC) rate [47]. Although this measure does not directly relate to final image quality, contrasting with the SNR, it does demonstrate the impact of random rates and scatter on the overall ability of the scanner to measure the true events count rate [23]. It is defined by:

$$NEC = \frac{Trues^2}{(Trues + Scatters) + f.k.Randoms} \quad \text{Eq. 6.3}$$

where f is the fraction of the sinogram width delimited by the phantom, usually 1, and k is a factor that depends on the method used for random correction, in our case 2. The NEC provides only a global measure of the signal-to-noise ratio because it is not sensitive to regional variations of the source distribution [15].

Some studies had already been made, prior to this work, to the acquired data, to study the impact of the variation of the timing window on the quality of the image. According to the NEC, the best timing window for our scanner is 4 ns.

6.2. Random Correction

Contrasting with what happened previously, the data used in this chapter was not solely corrected but also processed with the intent of determining the timing window that presents the best SNR and contrast results. The whole process of reconstruction (C language based) will be described.

As explained in Chapter 4, the data of each of the several projections (usually four) acquired per exam is stored in a binary raw data file, which is afterwards transformed in a list-mode file. Unlike the final list-mode files used for image reconstruction, these original files do not have any restrictions in either timing or energy windows, storing all the events in a 20 ns timing window and in an energy window of 200 to 700 keV.

For better results, as demonstrated, narrower windows are needed, hence the following step was creating new list-mode files with the chosen timing windows and a standard energy window of 400 to 700 *keV* for each acquisition. In this study, six different windows (3, 4, 5, 6, 7 and 8 *ns*) were applied and analysed with the main purpose of minimizing the presence of random coincidences but also of maximizing the true event rate. Additionally, to enable the second correction method, new list-mode files were created with the exact same specifications, yet with the delayed input. The subtraction does not take place until all the files are transformed into linograms and summed to create one final linogram per exam, which is the subsequent step.

At this point, in IDL development environment, the final linograms are assembled and both random and sensitivity correction are applied, setting the data ready for reconstruction. It is preferable that the same procedure is followed by the planar source, so that the different sampling in the FOV is properly rectified by the sensitivity correction method.

The routine ends with a standard OS-EM 2D reconstruction, with 4 subsets and 3 iterations. Nevertheless, with the intention of minimizing the presence of reconstruction induced noise, the 2nd iteration was chosen for all the following studies.

The difference between both reconstructed images – the regular data (Figure 6.1 (a)) and the random corrected data (Figure 6.1 (b)) – is presented below. Notice that with the removal of the random coincidences, the contrast of the image was increased, as well as the visual noise. The assessment of these two characteristics was the following action.

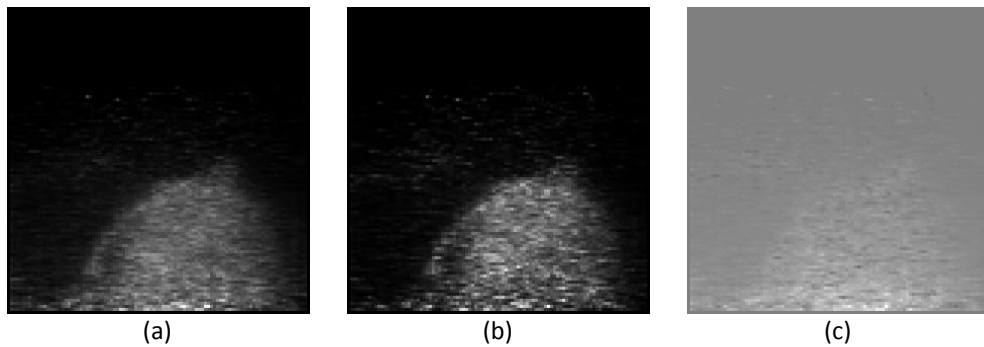


Figure 6.1: Result of difference (c) between the regular reconstruction (a) and the reconstruction of the random corrected data (b) with an 8 *ns* timing window.

With the intent of comprehending the implications of the variation of the timing window in the number of counts, we decided to present Table 6.1, where the total and the random count numbers for clinical case 1 are presented, and a relationship between them is established.

Table 6.1: Relationship between the total and the random count numbers.

<i>Timing Window (ns)</i>	<i>Total Counts</i>	<i>Random Counts</i>	<i>%</i>
3	1200508	414965	34.57%
4	1426892	544098	38.13%
5	1596016	667627	41.83%
6	1732292	783876	45.25%
7	1848573	892730	48.29%
8	1952463	994114	50.92%

Confirming our expectations, with the narrowing of the window, not only the total count number decreases, but also does the percentage of random events.

6.2.1. IMAGE CONTRAST

After the image reconstruction process, the six different timing windows were analysed in the three clinical cases with a method similar to the one employed in Chapter 5 for the study of regions of interest (ROIs) of the images. One of the main changes in this procedure is the use of two ROIs for each slice, instead of only one. The extra information allows not only the assessment of the contrast between different areas of the same image, but additionally, a different approach to the analysis of its SNR. To calculate the contrast values we used Eq. 6.4. More on the signal-to-noise ratio values will be presented in the following section.

$$Contrast = \frac{Avera\ ge_{breast} - Avera\ ge_{background}}{Avera\ ge_{breast} + Avera\ ge_{background}} \quad \text{Eq. 6.4}$$

Furthermore, unlike the previous method where several slices from the same clinical case were compared, one slice was selected from each clinical case and that same slice was the object of study throughout the rest of our work. Based on the observation of the reconstructed images, these slices were chosen for presenting a good visual profile of the breasts, as well as a good contrast with the background. Slices with numbers 43, 48, 44 and 49 were chosen, respectively, for clinical cases 1, 3, 4 and 5. It is important to point out that all the slices belong to the centre of the FOV, which is a result of a higher number of counts in this area. Despite being presented, clinical case number 4 does not present enough quality, hence it was not studied.

Two sets of differently shaped ROIs were drawn, a circular and a rectangular, each with a different purpose. We started by placing the first circular ROI approximately in the centre of the breast and the second one just beyond its border, assessing the background. As a consequence of breasts' different shapes and sizes, all the ROIs were positioned in different places, as shown in Figure 6.2.

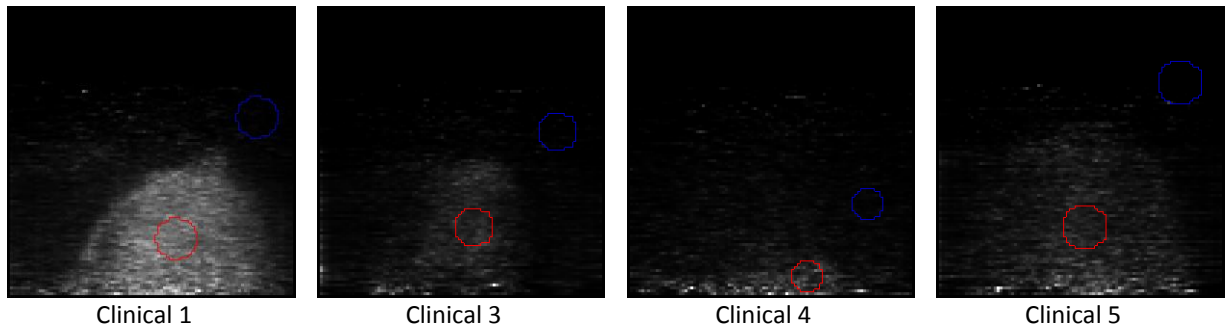


Figure 6.2: Circular ROIs marked on clinical cases 1, 3, 4 and 5.

The following step was positioning the rectangular ROIs, whose main goal was assessing the contrast between the centre and the bottom slices of the breast. In this particular case, the study of the bottom ROIs is very interesting, since this area is prone to the presence of random events originated in the torso. Again, the differences in the breasts originated different size and positioning ROIs (Figure 6.3).

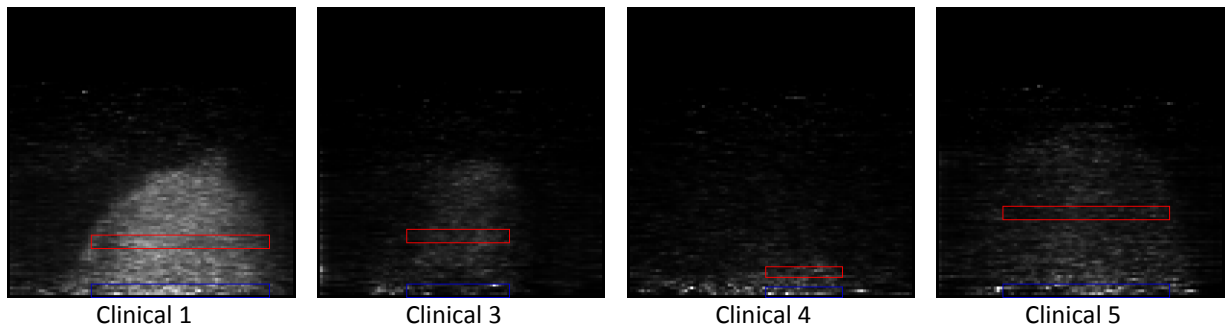


Figure 6.3: Rectangular ROIs marked on clinical cases 1, 3, 4 and 5.

Once more, the data was extracted from the images with the help of scripts developed in IDL.

The comparison between the timing windows regarding the contrast parameter was performed by plotting the contrast values as a function of the standard deviation in the central ROI. The standard deviation, as formerly stated, is an accurate measurement of the image noise, adding important information about the homogeneity of the breast in the reconstructed image. Thus, for this study, the best possible result would be a high contrast between the breast and the background and a low standard deviation of the central ROI. Concretely, we should be looking for a value located on the top left corner of the plot.

Due to the discrepancy of the contrast values of some timing windows and the rest of the values, a detail of the plots is sometimes presented.

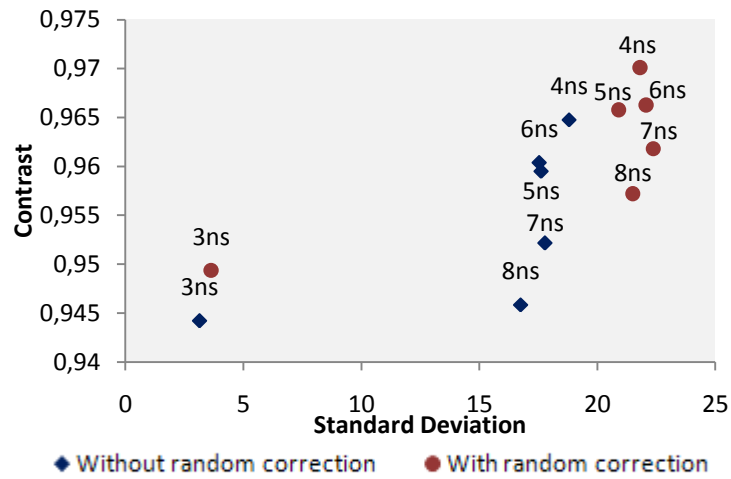


Figure 6.4: Contrast values obtained for Clinical 1 with a circular ROI.

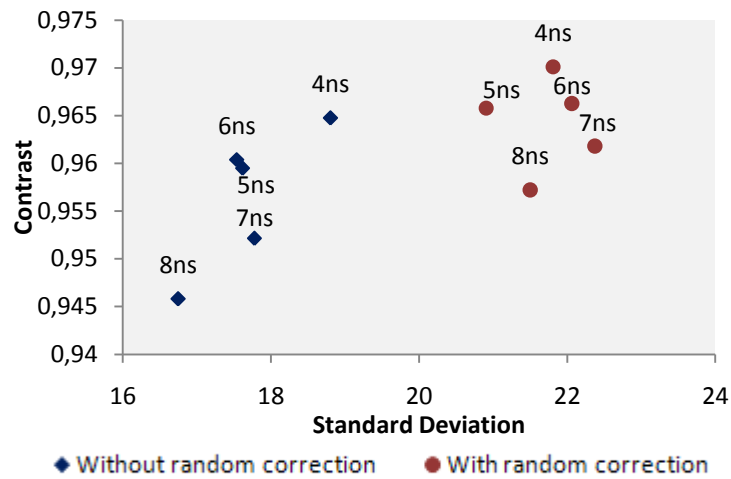


Figure 6.5: Detail of the contrast values obtained for Clinical 1 with a circular ROI.

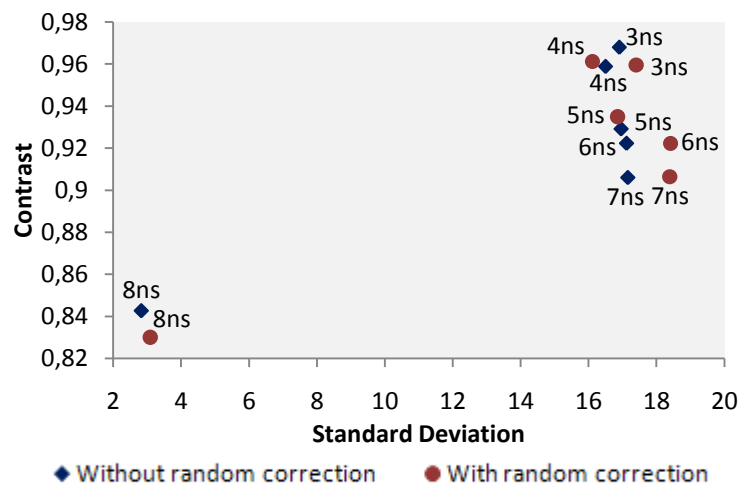


Figure 6.6: Contrast values obtained for Clinical 3 with a circular ROI.

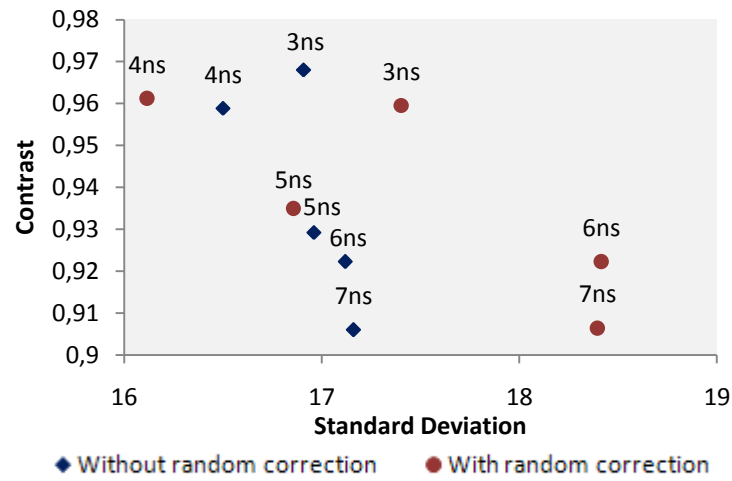


Figure 6.7: Detail of the contrast values obtained for Clinical 3 with a circular ROI.

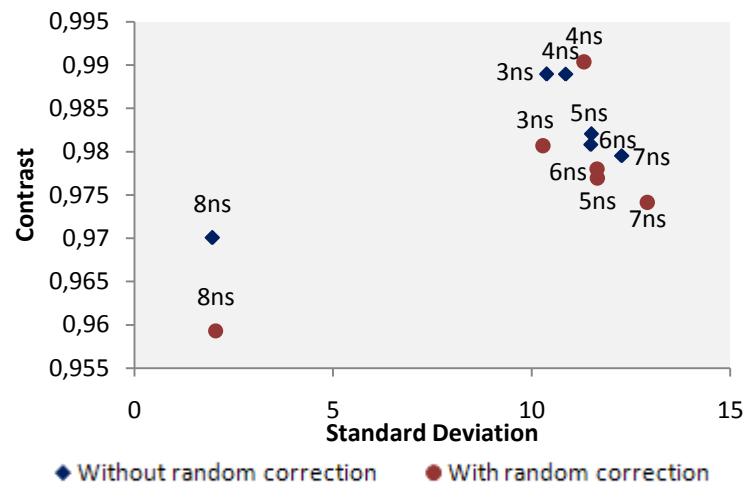


Figure 6.8: Contrast values obtained for Clinical 5 with a circular ROI.

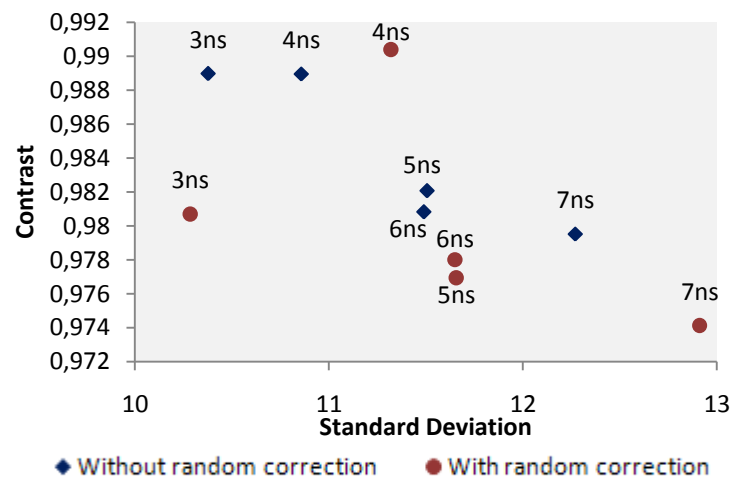


Figure 6.9: Detail of the contrast values obtained for Clinical 5 with a circular ROI.

In general, the best results of this first study were achieved for the narrowest timing windows, especially 4 ns. Recall that clinical cases number 1 and 3 presented the best results, with a higher number of counts, hence represent the most feasible results.

For data both with and without random correction, in clinical case 1 the higher contrast value occurs for a 4 ns timing window. Nevertheless, this good result is not flawless, for it presents a relatively high standard deviation as well. Moreover, the fact that the standard deviation values for the random corrected data are superior to the non-corrected was forecasted since the random correction itself results in noise propagation through the data.

In clinical case 3 the choice of the 4 ns timing window becomes more evident since, in addition to the good contrast, it also presents the lowest standard deviation.

For clinical case 5, timing windows of 3 and 4 ns still present the best options. However, the fact that the 3 ns window presented a somewhat odd behaviour in the first clinical case, we think that the 4 ns window might be the best alternative.

Throughout the clinical cases, some abnormal results were detected for 3 and 8 ns timing windows. The reasons behind this occurrence were unidentified.

Differing from the previous study, the analysis of the rectangular ROIs was intended for the evaluation of the contrast between two different regions of the breast. Hence, in this case a good result would be a low contrast between the two ROIs, since it would represent a homogeneous acquisition of the breast. A low standard deviation in the central ROI is still wanted. The contrast was calculated with Eq. 6.5.

$$Contrast = \frac{|Average_{central\ ROI} - Average_{bottom\ ROI}|}{Average_{central\ ROI} + Average_{bottom\ ROI}} \quad Eq. 6.5$$

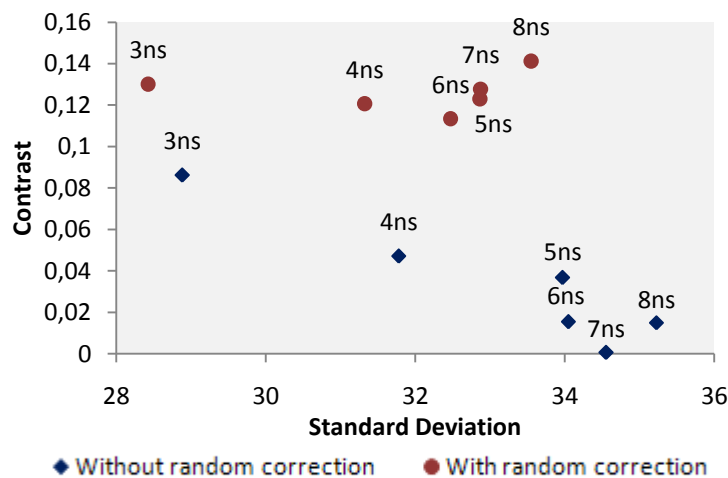


Figure 6.10: Contrast values obtained for Clinical 1 with a rectangular ROI.

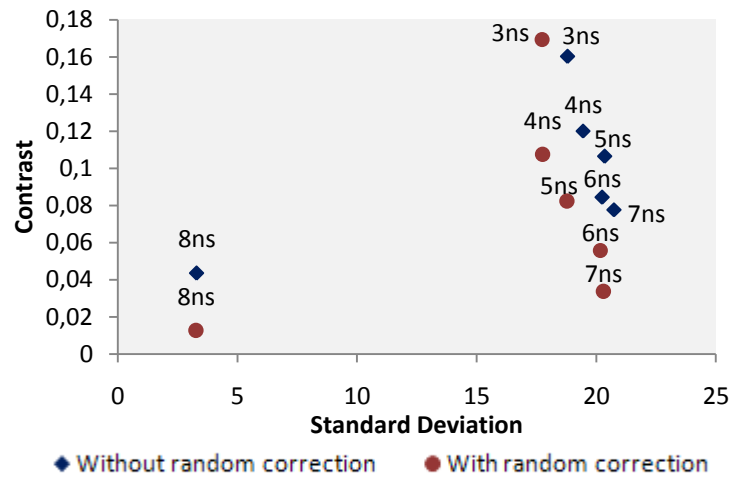


Figure 6.11: Contrast values obtained for Clinical 3 with a rectangular ROI.

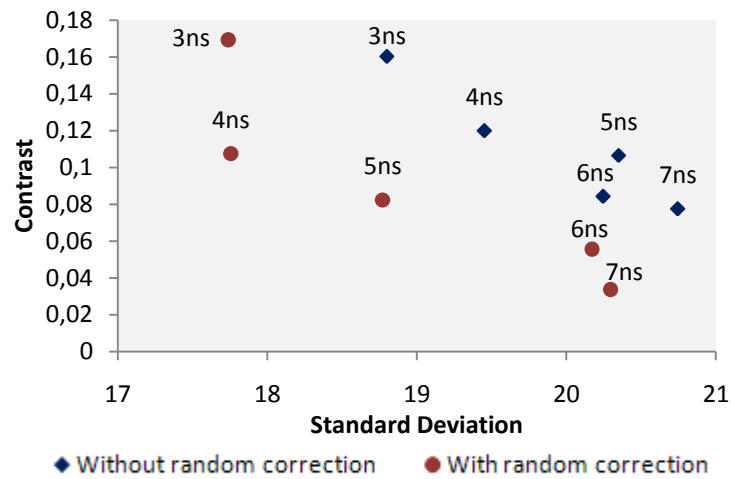


Figure 6.12: Detail of the contrast values obtained for Clinical 3 with a rectangular ROI.

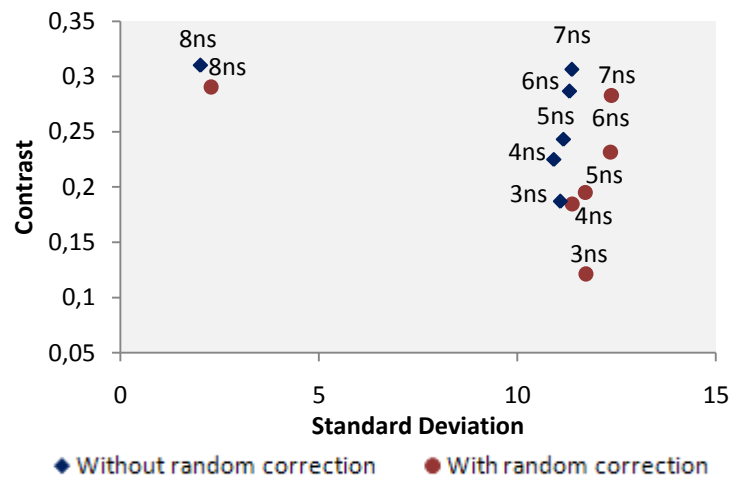


Figure 6.13: Contrast values obtained for Clinical 5 with a rectangular ROI.

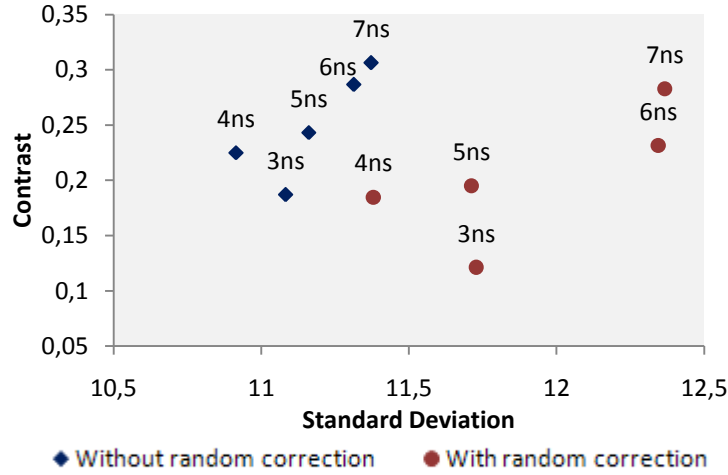


Figure 6.14: Detail of the contrast values obtained for Clinical 5 with a rectangular ROI.

For this study, the results are not as consensual as for the previous one, yet values 6 and 7 *ns* seem to be the most common. Then again, they still present a high standard deviation, which is was expected.

Even though in clinical case 3 the 8 *ns* timing window presented an optimal result, the unconformity with the rest of the results led us to believe that it was not feasible.

Lastly, for case 5 the best result was for a window of 3 *ns*, but it also had a high standard deviation.

6.2.2. IMAGE NOISE

To improve our confidence in the choice of the right timing window, two more studies took place, the first of which being the signal-to-noise ratio evaluation between the two ROIs. Given that this is an evaluation of two different ROIs, the calculation of the SNR experienced a small alteration, developing into Eq. 6.6:

$$SNR = \frac{Average_{breast} - Average_{background}}{Standard Deviation_{breast}} \quad \text{Eq. 6.6}$$

Circular ROIs were analysed and the SNR values were plotted as a function of the timing window.

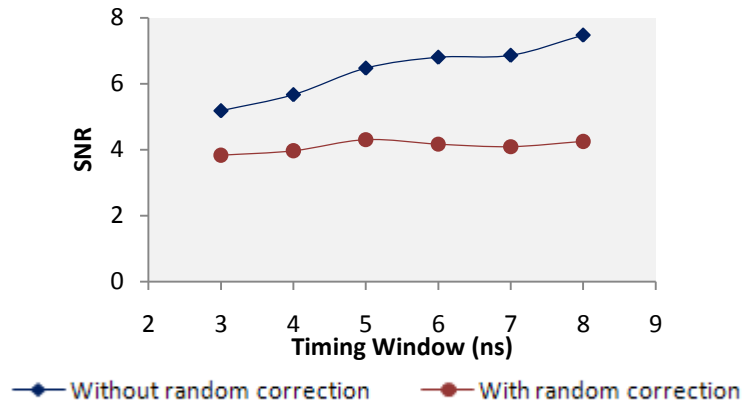


Figure 6.15: SNR values obtained with a circular ROI for clinical case 1.

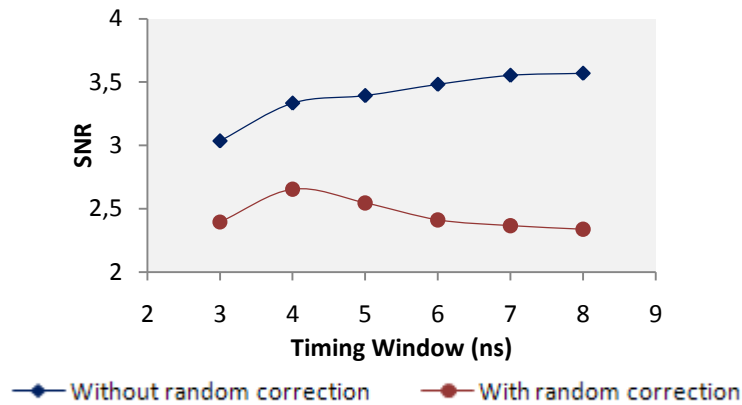


Figure 6.16: SNR values obtained with a circular ROI for clinical case 3.

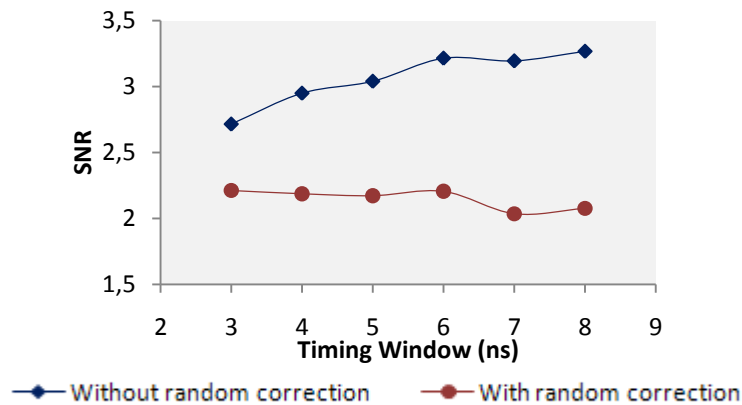


Figure 6.17: SNR values obtained with a circular ROI for clinical case 5.

The results are consistent with what was expected, since it is once again proven that the random correction increases the noise in the data. This comes from the fact that the number of random counts is subtracted from the number of total prompts, substantially decreasing the final value.

The most noticeable fact is that all three cases show a similar pattern, in which the SNR values of the non-corrected data increase with the timing window and the random corrected data values are relatively stable but present some peaks. Clinical case 1 has a peak

on 5 ns , whereas clinical case 3 has its maximum at 4 ns . Contrasting with the preceding cases, clinical 5 values decrease with the timing window.

Note that, again, clinical case 1 presents the best results by having the highest SNR values, and it is followed by clinical case 3.

6.2.3. PRESENCE OF HIGH INTENSITY PIXELS

The following, and last, study related to random correction is the assessment of the presence of high intensity pixels on the bottom slices of the breast. As has been somewhat explained, the low number of counts on the bottom slices of the FOV is affected by the sensitivity correction and reflects as extremely bright pixels that disrupt the final image contrast. In addition, the effect of the random events on this region of the breast is amplified by the proximity with the torso, as can be seen in Figure 6.3. This study allowed us to find the timing window that is less affected by these phenomena. Bottom rectangular ROIs were analysed and the maximum values plotted as a function of the timing window.

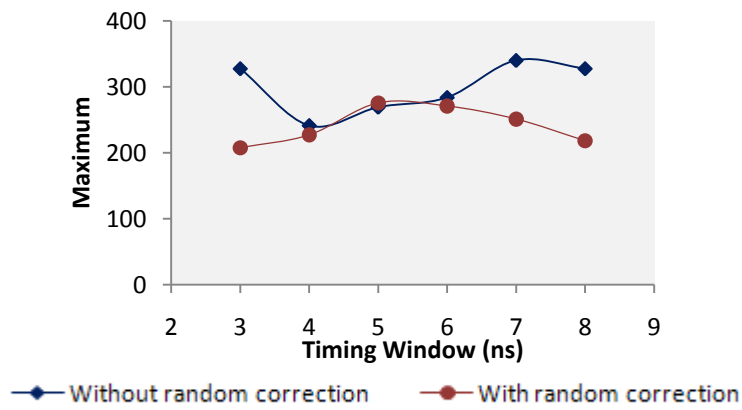


Figure 6.18: Maximum values obtained with a bottom rectangular ROI for clinical case 1.

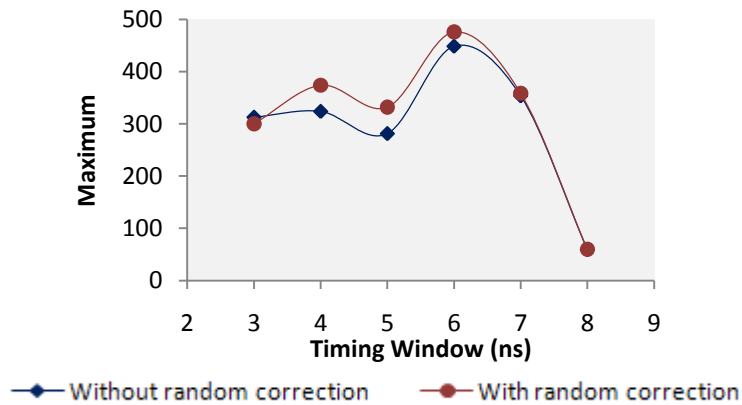


Figure 6.19: Maximum values obtained with a bottom rectangular ROI for clinical case 3.

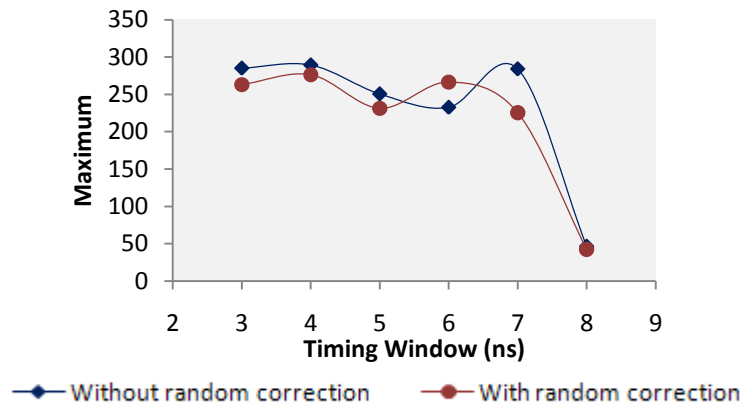


Figure 6.20: Maximum values obtained with a bottom rectangular ROI for clinical case 5.

There is no clear similarity between the three clinical cases results. Clinical cases 3 and 5 do present a very low maximum for the 8 ns timing window, but again these were the two cases which showed an odd behaviour on the first study, and were removed for a better analysis of the plot.

From an overall look, it is possible to say that, again, the narrowest windows present the best results, especially for clinical case 1 where they have considerably lower values than the other windows.

Also interesting is the fact that, in two of the three cases, the random corrected data presented lower values, meaning that it also helps to correct high intensity pixels.

6.2.4. DISCUSSION

The review of all the studies led us to conclude that, for enabling a good contrast while, at the same time not damaging the images with noise, a timing window of 4 ns is a good choice. It fits the main requirement, which was to be a narrow window, it is effective in reducing the rate of random coincidences, and it meets the result of the NEC study previously done.

Apart from the slight increase of noise in the images, the random correction based on the subtraction of the second timing window also seems to be a good option, since it does contribute to the image contrast as well as for reducing the presence of high intensity pixels.

Chapter 7.

Scattered Correction

The last stage in our process of improving image contrast and reducing noise was the correction of scattered coincidences, which will be addressed in this chapter.

7.1. Energy Window

PET is based on the principle of coincidence detection of the two 511 *keV* photons arising from positron annihilation, as was already explained in Chapter 2. However, the two coincident photons can belong to three different kinds of events: true, random and scattered. One of the goals for this work was to maximize true coincidences whilst correcting the presence of random and scattered events, which only contribute to degrading the quality of the data.

Scatter correction is probably the most difficult correction required in PET, since scatter coincidences are also originated on single annihilation events. They are indistinguishable from true events except on the basis of energy, given that they undergo Compton scattering in the patient's body, experiencing the loss of a substantial fraction of their initial energy [15]. As a result, the scattered coincidences lead to incorrectly positioned LORs and therefore misrepresent the true activity distribution within the FOV, worsening the image contrast [8].

To assure the detection of all the events on a 511 *keV* range, as well as restricting the detection of scatters, an energy window is implemented.

The difficulty in separating scattered from true events is increased by the fact that a significant fraction of the true 511 *keV* photons will only deposit a portion of their energy within the detector volume. Albeit being true events, they are detected in the same energy range as scattered events. Thus, if the system would only accept events within a narrow energy window, the overall detection efficiency of the system would be very poor [15].

A compromise between the number of scattered and true coincidences needs to be found through the definition of a lower limit of detection for the energy window [23].

7.2. Scattered Correction

After the review on random correction on the previous chapter, we present the studies for scattered correction. Most of the procedures used in this chapter were already fully explained on the previous one.

Following the same process used before the reconstruction of the different timing window images, but this time for the energy, six different windows (200, 250, 300, 350, 400 and 450 *keV* – 700 *keV*) were applied to the data and then analysed. In addition to the clinical cases, the acquisition of a point source phantom was evaluated. In both cases, the timing window defined on the previous chapter (4*ns*) was applied. However, on the point source phantom reconstruction, the random correction was not used, as a result of the low number of counts obtained with the phantom.

In conformity with the prior study, the OS-EM 2D reconstruction, with 4 subsets and 3 iterations was also used, with the 2nd iteration being the final choice.

7.2.1. IMAGE CONTRAST

The first study of the energy window was similar to the one applied on the previous chapter.

We started by selecting the same slices on each of the three clinical cases (1, 3 and 5) we had already used for the timing window studies, which were 43, 48 and 49 respectively. Being a contrast analysis, this study required the comparison of two different ROIs, one on the breast and one on the background. To maintain a concordance in the analysis, the same ROIs, represented in Figure 6.2, were employed. The contrast was then calculated with Eq. 6.4 and plotted as a function of the standard deviation of the central ROI.

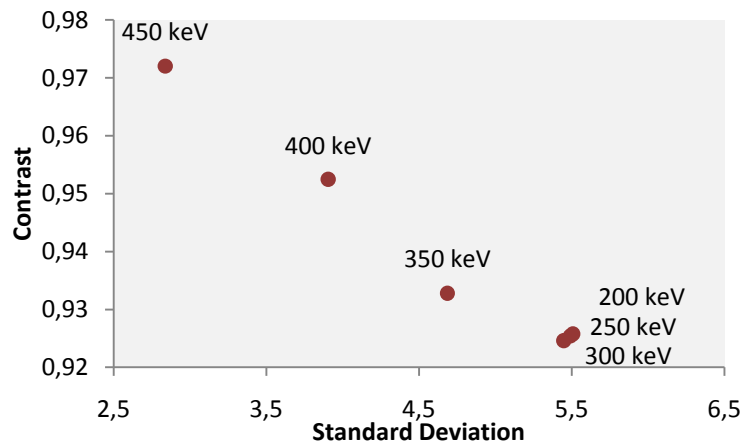


Figure 7.1: Contrast values obtained for Clinical 1 with a circular ROI.

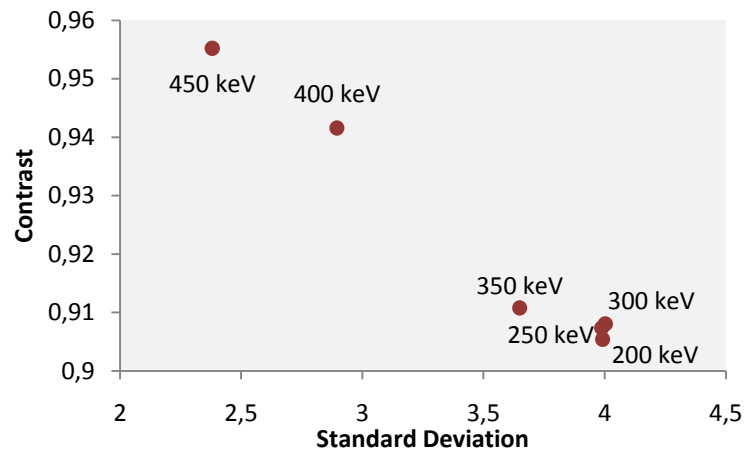


Figure 7.2: Contrast values obtained for Clinical 3 with a circular ROI.

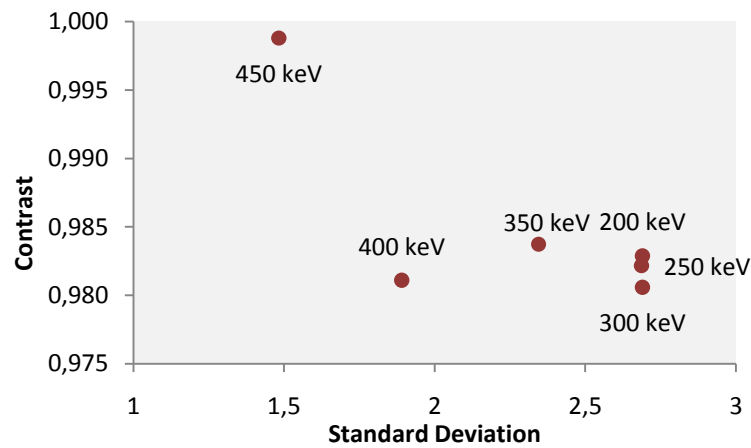


Figure 7.3: Contrast values obtained for Clinical 5 with a circular ROI.

In an evaluation of the contrast between breast and background, as was already explained, the best possible result is a high contrast, which means that the different structures are easily identifiable, and low standard deviation, meaning a reduced amount of noise.

All three cases present very similar plots and a matching best result for the 450 keV energy window. The fact that the narrowest window presents higher contrast results from a decrease of the scattered coincidences in the background of the image. Analogously, this window presents a low standard deviation value since the number of scattered events on the breast also decreased, reducing the associated noise. Wider windows will comprise a larger number of scattered events and, therefore, a diminished contrast.

7.2.2. IMAGE NOISE

Continuing the assessment of the obtained images, the subsequent step was the evaluation of the breast's homogeneity in the same conditions. This time the images were

subjected to the same circular ROIs, using Eq. 6.6 to calculate the SNR and plot it as a function of the energy window. Again, we are in the search of a higher SNR value, which stands for a less noisy image.

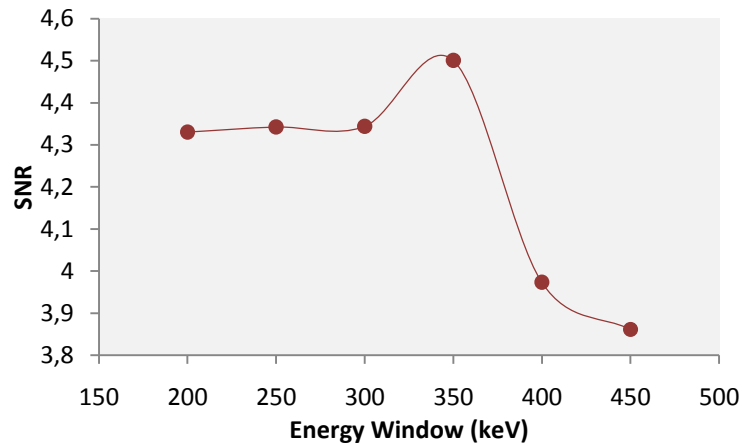


Figure 7.4: SNR values obtained with a circular ROI for clinical case 1.

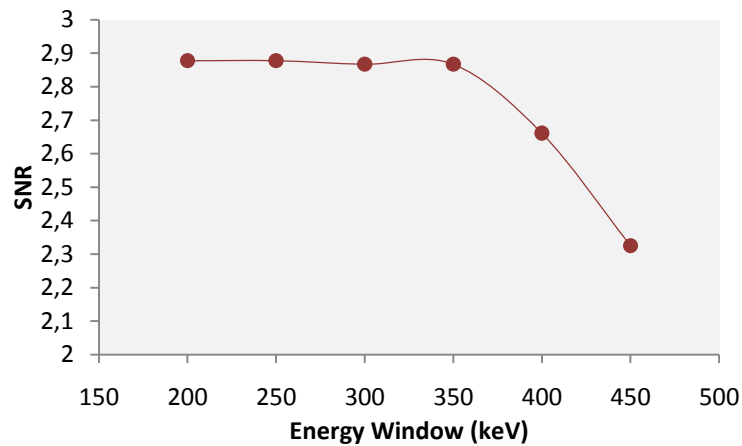


Figure 7.5: SNR values obtained with a circular ROI for clinical case 3.

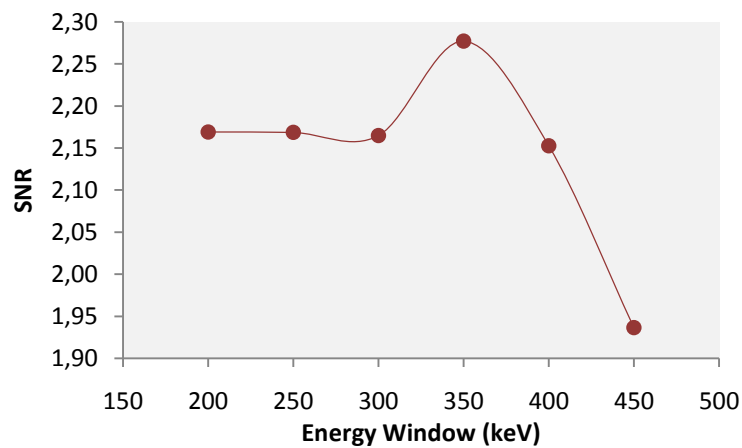


Figure 7.6: SNR values obtained with a circular ROI for clinical case 5.

Once more, the coherence between the results is a good indicator of which might be the best window option. In all three cases, the 350 – 700 *keV* window shows a big advantage compared to the other cases, presenting itself as the best solution. However, the good performance in this study is somewhat tainted for its low contrast result.

As expected, the narrowest window (450 *keV*) displays a very low SNR value. This fact, which is also visible in the 400 *keV* window but on a less significant way, was expected and is the result of the removal of too many true coincidences, decreasing the signal that ends up being overwhelmed by the noise. To confirm this fact, we present the total number of counts per energy window for clinical case 1 on Table 7.1.

Table 7.1: Total count numbers with the variation of energy window.

<i>Energy Window (keV)</i>	<i>Total Counts</i>
200	2279291
250	2278226
300	2267405
350	2018533
400	1426892
450	933452

The difference between the widest and the narrowest windows is, approximately, 59%, which proves that, along with the scattered events, many true coincidences were removed, diminishing the statistical data, and hence amplifying the presence noise.

7.2.3. SPATIAL RESOLUTION STUDIES

The last study developed for this work was the evaluation of spatial resolution using a point source phantom.

7.2.2.1. Point Source Phantom

The use of the simplest form of phantom, the point source, is very useful for the assessment of the spatial resolution of the data. With a ^{22}Na point source, with 1 *mm* diameter and 40 *mCi*, placed in the centre of the middle transaxial plane (plane *yz*), four five minute-long acquisitions were made with 90°, 135°, 180° and 225° positioning.

Like in the previous cases, the data was reconstructed for the all the energy windows in study. A detail cropped from the reconstructed images is presented in Figure 7.7, all with the same zoom.

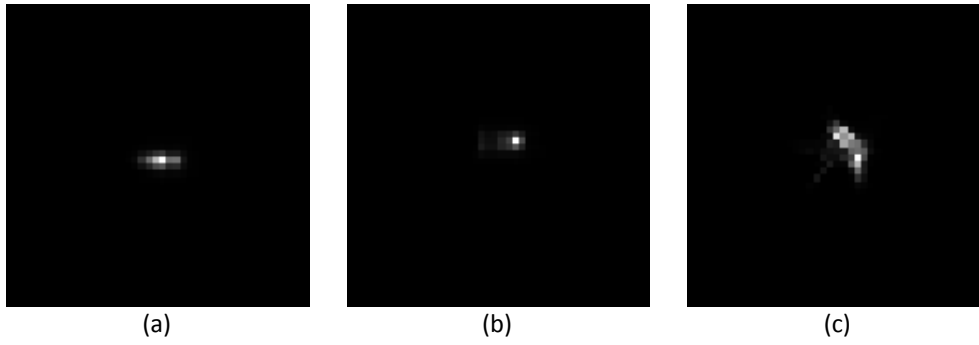


Figure 7.7: Image detail of the reconstruction of the point source phantom without corrections in the (a) yz, (b) xz and (c) xy planes.

The slices in which the point source is visible are 55, 51 and 38, on planes yz, xz and xy., respectively.

It is possible to see in Figure 7.7 (c) that the reconstruction of the plane xy has been compromised, since the reconstructed phantom does not look homogeneous like in Figure 7.7 (a) and (b). To try to understand the origin of the problem, we registered the number of counts on each of the acquisition positions. These are presented in Table 7.2.

Table 7.2: Number of counts per acquisition position of the point source phantom.

<i>Acquisition Position</i>	<i>Number of Counts</i>
90°	147397
135°	195941
180°	210139
225°	196719

In fact, it seems like the 90° acquisition should have lasted longer, since it holds, approximately, less 26% of the number of counts than the average for the other acquisitions. This fact influenced the data and its reconstruction by adding some blurring to the image.

7.2.2.2. FWHM

The spatial resolution was calculated for three orthogonal directions as the Full Width at Half Maximum (FWHM) of a Gaussian curve that was fitted to an activity profile obtained along the three orthogonal axes (x, y and z). The FWHM is often used to characterize a distribution that is Gaussian or nearly Gaussian and involves measuring the width of the distribution at the point where it reaches half the maximum amplitude [15].

The curve fits were performed using the functionalities of *Quasimanager* and are, along with the chosen profiles, illustrated in Figure 7.8, Figure 7.9 and Figure 7.10.

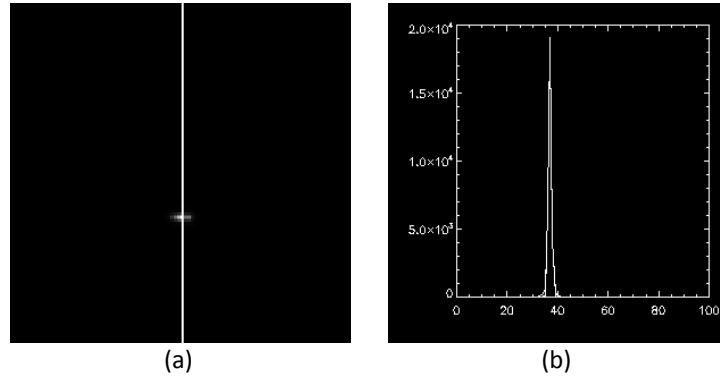


Figure 7.8: Profile (a) and Gaussian curve fit (b) for the yz plane of the point source.

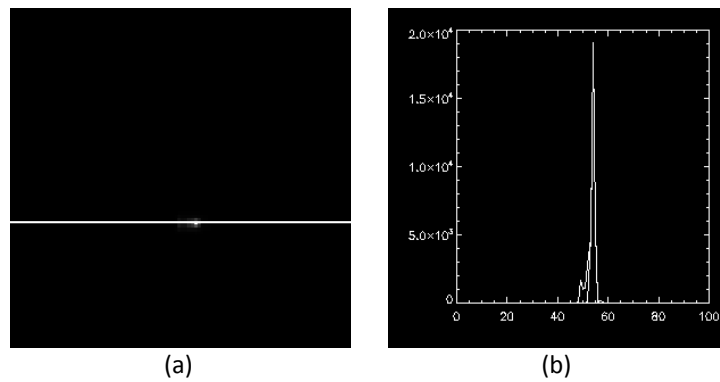


Figure 7.9: Profile (a) and Gaussian curve fit (b) for the xz plane of the point source.

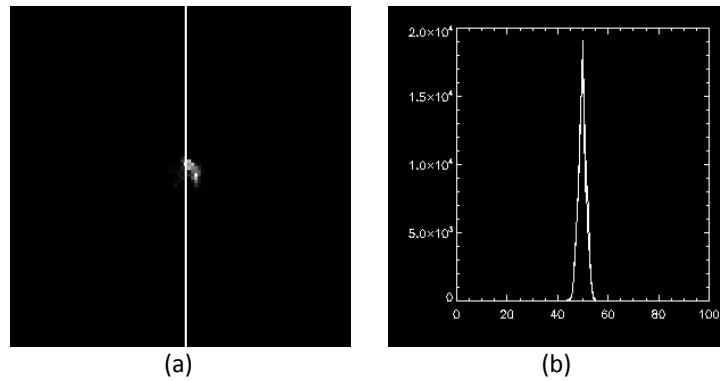


Figure 7.10: Profile (a) and Gaussian curve fit (b) for the xy plane of the point source.

The process was repeated for all the energy windows and the spatial resolution results were plotted as a function of the iteration number.

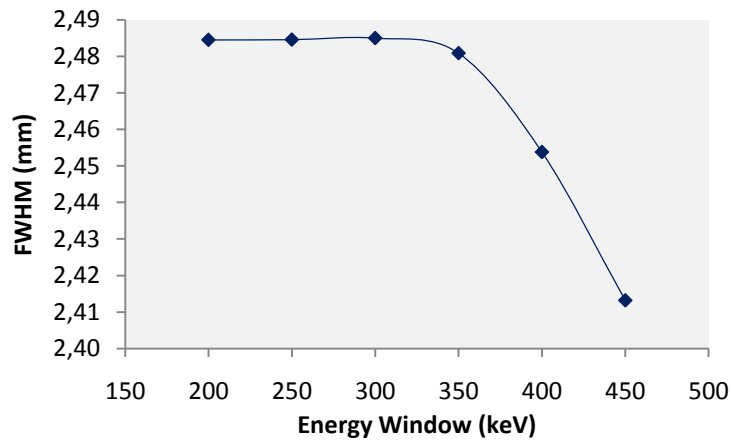


Figure 7.11: FWHM values for the point source phantom in plane yz.

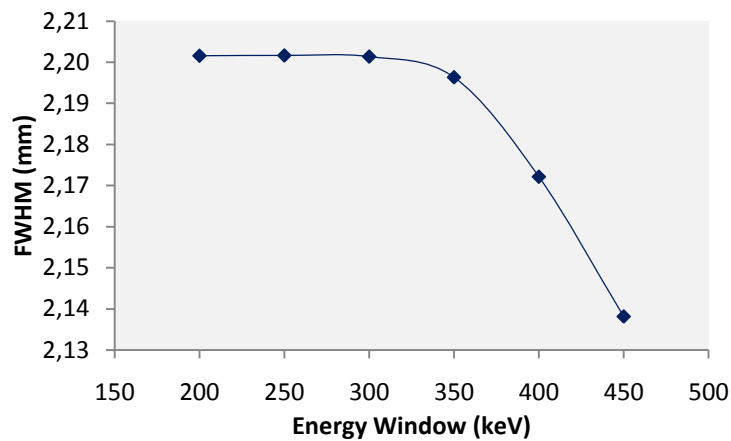


Figure 7.12: FWHM values for the point source phantom in plane xz.

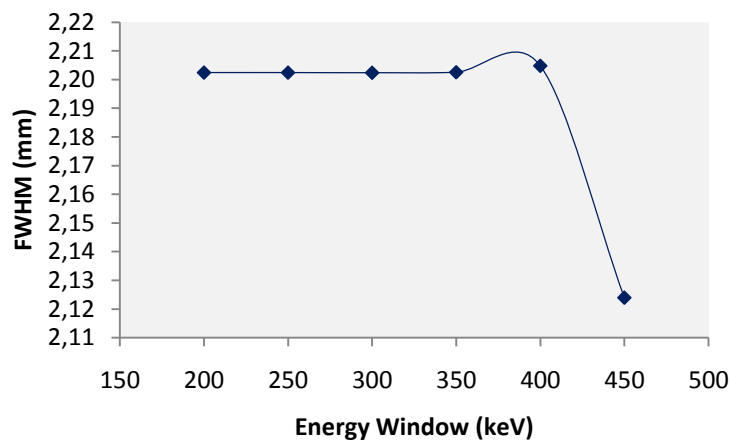


Figure 7.13: FWHM values for the point source phantom in plane xy.

Once again, we have concordance between the results. In this case, the FWHM values are approximately constant until 350 keV at which time they show an abrupt fall until 450 – 700 keV, the narrowest window, which provides the best spatial resolution.

7.2.4. DISCUSSION

After all the studies, it was necessary to analyse the data and choose the best possible energy window. From all energy windows, the 450 – 700 *keV* was the one which presented the best result in two of the three tests (Contrast and Spatial Resolution). However, in the SNR assessment it presented the worst result of all the windows, with the best being the 350 – 700 *keV* window.

For these reasons, we opted for the 400 – 700 *keV* energy window. Even though it was not the best result in any of the studies, we had to compromise and chose the value in between the two best results.

To conclude our work, we decided to compare the reconstruction and correction methods used prior to this work with the conclusions we have achieved. We followed both procedures, and used the OS-EM 2D reconstruction, with 4 subsets and 3 iterations to reconstruct the clinical case 1, whose images are presented below.

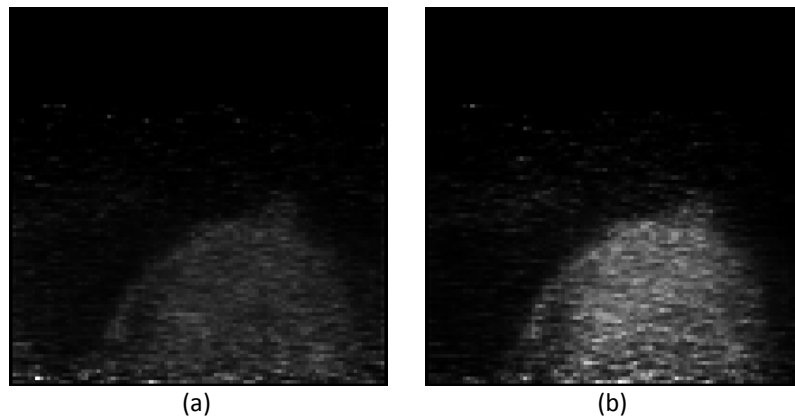


Figure 7.14: Clinical case 1 reconstructed with the procedures (a) prior to this work and (b) defined in this work.

The most noticeable difference is the increase of the contrast, making the breast's limits now easier to identify. In addition, some of the noise of the background was reduced, along with the bright pixels outside of the breast, although they are still present on the bottom slices of the breast.

Chapter 8.

Main Discussion and Conclusions

The parameters defined in this work, for the reconstruction and processing of the data obtained with the prototype Clear-PEM, improved the image quality in many ways. Not only was the sensitivity of the images enhanced, but also the contrast between the breast and the background was improved and the noise lessened.

The major problems of the uncorrected data were the different sampling across the field of view and the effect of the presence of gaps between the scanner's crystals in the images. For the implemented correction method, based on the comparison of the acquired data with a normalization planar source, we defined a threshold below which the planar source values were considered to belong either to a gap or to a less sensible area, thus being in need of correction. These values were then corrected through a division by the threshold, proportional to the planar source's maximum value, that incremented them to a value similar to their original one. However, when the pixel value was too low, the division resulted in an excessive increase, and these pixels started to present an excessive intensity.

This method presents four challenges: correcting the presence of the crystal's gaps, increasing the signal-to-noise ratio and image contrast, and reducing the number and value of the high intensity pixels. The influence of several possible thresholds was studied on the acquired data. The first conclusion set that the maximum plausible value for the threshold was 0.008, yet it could not be too small either, since it would increase the number and intensity of the bright pixels. All four issues were addressed by choosing a 0.005 threshold.

Some efforts were made with the intent of incorporating a sensitivity correction technique in the system matrix calculation, based on the analytical modelling of detector gaps. The outcome proved that the result was insufficient, since the correction did not take the different sampling of the FOV into account.

Additionally, two more corrections were studied: random and scattered corrections. The main goal in each of these corrections was to reduce the impact of non-true events on the image, such as noise, contrast and spatial resolution.

In the first case, for random correction, we decided to study the variation of the timing window. For six different windows, the image contrast and noise and the presence of highly intense pixels were assessed. It was proven that the narrower the window, the less

random events are recorded, hence, there is less background noise in the image and an increase of the contrast between the breast and the background. Despite this, if the window is too narrow, the number of counts will be lessened and some true events will be ignored, leading to a reduced SNR. On the other side, if the timing window is too wide, a larger quantity of random events will be recorded. The high intensity pixels are also influenced by this variation, since the most affected area is the bottom of the breast, mainly because a large number of random events come from the torso. After all the studies, it was proven that the best choice is a 4 *ns* timing window.

For the scattered correction, a similar method was chosen. The photons that experience the Compton effect are scattered from their path, losing energy along the way. By narrowing the energy window down the scattered events will not be recorded as coincidences. Once more, the variations were applied to the clinical cases and plotted for study. A direct result from the narrowing of the window, is the enhancement of the contrast, since less scattered events will be mis-positioned on the background, worsening the definition of the breast's limits. As a consequence, the number of true coincidences will also be lessened, resulting in a lower SNR. This is why the energy window cannot be too restricted. Since the Compton effect has an important consequence on the spatial resolution, an additional analysis to the spatial resolution was developed. As it was expected, a narrow window will improve the spatial resolution, since less scattered events are degrading the data. In the end, a compromise was made between the two best results and a 400 – 700 *keV* energy window was chosen.

It is from the combination of a set of parameters that the image quality can be improved. In our case, the adjustment of these small parameters made a significant and considerable difference on the images' results, improving their contrast and decreasing the noise, not only in comparison with the procedure in use prior to this work but especially when comparing to the reconstructions without any correction.

The conclusions of this work are already being implemented in other studies, such as the enhancement of the spatial resolution as a result of the variation of the thickness of the slices and the consequent alteration on the voxel dimension, and an analysis of the LORs positioning.

The scanner is under a constant process of improvement, so it remains important to evaluate more cases.

It is possible to declare that the goals we set to achieve were accomplished.

Bibliography

- [1] World Health Organization, <http://www.who.int/cancer/en/> [September, 19th 2009].
- [2] American Cancer Society, <http://www.cancer.org> [September, 19th 2009].
- [3] Sharp, P.F., H.G. Gemmell, and A.D. Murray, *Practical nuclear medicine*. 2005: Springer Verlag.
- [4] Townsend, D.W. and S.R. Cherry, *Combining anatomy and function: the path to true image fusion*. *European Radiology*, 2001. **11**(10): p. 1968-74.
- [5] Abreu, M.C., et al., *Design and Evaluation of the Clear-PEM Scanner for Positron Emission Mammography*. *IEEE Transactions on Nuclear Science*, 2006. **53**(1): p. 71-77.
- [6] Wallace, A.M., et al., *Breast imaging: a surgeon's prospective*. *Nuclear Medicine and Biology*, 2005. **32**(7): p. 781-792.
- [7] Thompson, C.J., et al., *Feasibility study for positron emission mammography*. *Medical Physics*, 1994. **21**(4): p. 529-38.
- [8] Valk, P.E., et al., *Positron emission tomography: basic science and clinical practice*. 2003: Springer Verlag.
- [9] Guerreiro, C., et al., *Component-based normalization correction for the Clear-PEM Positron Emission Mammography system*. 2009.
- [10] Madsen, M.T., *Recent Advances in SPECT Imaging*. *Journal of Nuclear Medicine*, 2007. **48**(4): p. 661-73.
- [11] Newman, S.P. and I.R. Wilding, *Gamma scintigraphy: an in vivo technique for assessing the equivalence of inhaled products*. *International Journal of Pharmaceutics*, 1998. **170**(1): p. 1-9.
- [12] Newman, S.P. and I.R. Wilding, *Imaging techniques for assessing drug delivery in man*. *Pharmaceutical Science & Technology Today*, 1999. **2**(5): p. 181-189.
- [13] Alavi, A. and S. Basu, *Planar and SPECT imaging in the era of PET and PET-CT: can it survive the test of time?* *European Journal of Nuclear Medicine and Molecular Imaging*, 2008. **35**(8): p. 1554-1559.
- [14] Smith, I.C. and F.J. Gilbert, *Role of positron emission tomography in the management of breast cancer*. *Breast*, 1999. **8**(6): p. 303-10.
- [15] Phelps, M.E., *PET: physics, instrumentation, and scanners*. 2006: Springer Verlag.
- [16] Saha, G.B., *Basics of PET imaging: physics, chemistry, and regulations*. 2005: Springer.
- [17] Powsner, R.A. and E.R. Powsner, *Essential nuclear medicine physics*. 2006: Blackwell Pub.
- [18] Trindade, A., et al. *Breast Cancer Imaging Studies by Monte Carlo Simulation with Clear-PEM*. in *2005 IEEE Nuclear Science Symposium - Conference Record, Vols 1-3*. 2005.
- [19] Townsend, D.W., *Positron emission tomography/computed tomography*. *Seminars in Nuclear Medicine*, 2008. **38**(3): p. 152-166.

- [20] Lecoq, P. and J. Varela, *Clear-PEM, a dedicated PET camera for mammography*. Nuclear Instruments & Methods in Physics Research Section A - Accelerators Spectrometers Detectors and Associated Equipment, 2002. **486**(1-2): p. 1-6.
- [21] Santos, A.I., et al., *Design and evaluation of the clear-PEM detector for positron emission mammography*, in *2004 IEEE Nuclear Science Symposium Conference Record, Vols 1-7*. 2004. p. 3805-3809.
- [22] Amaral, P., et al., *Performance and quality control of Clear-PEM detector modules*. Nuclear Instruments & Methods in Physics Research Section A - Accelerators Spectrometers Detectors and Associated Equipment, 2007. **580**(2): p. 1123-1126.
- [23] Wernick, M.N. and J.N. Aarsvold, *Emission tomography: the fundamentals of PET and SPECT*. 2004: Academic Press.
- [24] Lucignani, G., *Time-of-flight PET and PET/MRI: recurrent dreams or actual realities?* European Journal of Nuclear Medicine and Molecular Imaging, 2006. **33**(8): p. 969-971.
- [25] Oliveira, N., et al., *Optimization of 2D image reconstruction for positron emission mammography using IDL*. Computers in Biology and Medicine, 2009. **39**(2): p. 119-129.
- [26] Martins, M.V., *3D Image Reconstruction for a Dual Plate Positron Emission Tomograph: Application to Mammography*, PhD dissertation, Universidade de Lisboa - Faculdade de Ciências, Lisboa, 2008.
- [27] Fahey, F.H., *Data acquisition in PET imaging*. Journal of Nuclear Medicine Technology, 2002. **30**(2): p. 39-49.
- [28] Matela, N., *2D Iterative Image Reconstruction for a Dual Planar Detector for Positron Emission Mammography*, PhD dissertation, Universidade de Lisboa - Faculdade de Ciências, Lisboa, 2008.
- [29] Edholm, P.R. and G.T. Herman, *Linograms in Image-Reconstruction from Projections*. IEEE Transactions on Medical Imaging, 1987. **6**(4): p. 301-307.
- [30] Hamill, J., C. Michel, and P. Kinahan, *Fast PET EM reconstruction from linograms*. IEEE Transactions on Nuclear Science, 2003. **50**(5): p. 1630-1635.
- [31] Daube-Witherspoon, M.E. and G. Muehllehner, *Treatment of Axial Data in 3-Dimensional PET*. Journal of Nuclear Medicine, 1987. **28**(11): p. 1717-1724.
- [32] Lewitt, R.M., G. Muehllehner, and J.S. Karp, *Three-dimensional image reconstruction for PET by multi-slice rebinning and axial image filtering*. Physics in Medicine and Biology, 1994. **39**(3): p. 321-339.
- [33] Defrise, M., et al., *Exact and approximate rebinning algorithms for 3-D PET data*. IEEE Transactions on Medical Imaging, 1997. **16**(2): p. 145-158.
- [34] Defrise, M. and X.A. Liu, *A fast rebinning algorithm for 3D positron emission tomography using John's equation*. Inverse Problems, 1999. **15**(4): p. 1047-1065.
- [35] Liu, X., et al., *Exact rebinning methods for three-dimensional PET*. IEEE Transactions on Medical Imaging, 1999. **18**(8): p. 657-664.
- [36] Kinahan, P.E., et al., *Fully 3D iterative reconstruction of planogram data*, in *3D2001 - 6th International Meeting on Fully Three-Dimensional Image Reconstruction in Radiology and Nuclear Medicine*. 2001.
- [37] Bracewell, R.N., *The Fourier Transform and its Applications*. 3rd ed. 2000: McGraw-Hill International Editions.
- [38] Qi, J. and R.M. Leahy, *Iterative reconstruction techniques in emission computed tomography*. Physics in Medicine and Biology, 2006. **51**(15): p. R541-R578.

- [39] Ferreira, N.C., *Contribuição para a quantificação em Tomografia por Emissão de Positrões no modo 3D*, PhD dissertation, Faculdade de Medicina da Universidade de Coimbra, Coimbra, 2001.
- [40] Fessler, J.A., *Penalized Weighted Least-Squares Image-Reconstruction for Positron Emission Tomography*. IEEE Transactions on Medical Imaging, 1994. **13**(2): p. 290-300.
- [41] Siddon, R.L., *Fast calculation of the exact radiological path for a three-dimensional CT array*. Medical Physics, 1985. **12**(2): p. 252-5.
- [42] Herman, G.T., *Image Reconstruction from Projections: The Fundamentals of Computerized Tomography*. 1980, Academic Press, New York.
- [43] Matela, N., et al., *Comparison of Different Image Reconstruction Strategies in Clear-PEM*, in *CIMED 05 - Second International Conference on Computational Intelligence in Medicine and Healthcare, Conference Records*. 2005, IEE.
- [44] Dempster, A.P., N.M. Laird, and D.B. Rubin, *Maximum Likelihood from Incomplete Data Via Em Algorithm*. Journal of the Royal Statistical Society Series B-Methodological, 1977. **39**(1): p. 1-38.
- [45] Shepp, L.A. and Y. Vardi, *Maximum Likelihood Reconstruction for Emission Tomography*. IEEE Transactions on Medical Imaging, 1982. **MI-1**(2): p. 113-122.
- [46] Hudson, H.M. and R.S. Larkin, *Accelerated Image-Reconstruction Using Ordered Subsets of Projection Data*. IEEE Transactions on Medical Imaging, 1994. **13**(4): p. 601-609.
- [47] Strother, S.C., M.E. Casey, and E.J. Hoffman, *Measuring PET Scanner Sensitivity - Relating Countrates to Image Signal-to-Noise Ratios Using Noise Equivalent Counts*. IEEE Transactions on Nuclear Science, 1990. **37**(2): p. 783-788.

Appendix

A.1. – Sensitivity Correction

linosensicor.pro

```
PRO linosensicor, PLANARFILE = planarfile, LINO_ORI_FILE = lino_ori_file, LINO_COR_FILE =  
lino_cor_file, ACQPOS = acqpos, DETECTDIST = detectdist, REBINNING = rebinning  
  
close, /all  
time=systime(1)  
  
xdim = 100  
ydim = 100  
zdim = 101  
  
lino_ori = dblarr(xdim, ydim, acqpos*zdim)  
lino_planar = dblarr(xdim, ydim, zdim)  
lino_cor = dblarr(xdim, ydim, acqpos*zdim)  
  
openr, 20, lino_ori_file  
readu, 20, lino_ori  
close, 20  
  
openr, 20, planarfile  
readu, 20, lino_planar  
close, 20  
maxlino = max(lino_planar)  
print, "maxlino=", maxlino  
  
for pos=0, acqpos-1 do begin  
  for l=0, xdim-1 do begin  
    for j=0, ydim-1 do begin  
      for k=0, zdim-1 do begin  
        if lino_planar(l,j,k) gt 0.005*maxlino then begin  
          lino_cor(l,j,k+pos*zdim)=lino_ori(l,j,k+pos*zdim)*maxlino/lino_planar(l,j,k)  
        endif else lino_cor(l,j,k+pos*zdim)=lino_ori(l,j,k+pos*zdim)/0.005  
      endfor ;k  
    endfor ;j  
  endfor ;l  
endfor ;pos
```

```

for k=0, acqpos*zdim-1 do begin
  for j=0, ydim-1 do begin
    perfil = where(lino_cor(*,j,k) GT 0.0001, CT)
    if CT NE 0 THEN BEGIN
      lino_cor[perfil[0],j,k]=0
      lino_cor[perfil[ct-1], j,k]=0
    ENDIF
  ENDFOR
ENDFOR

for k=0, acqpos*zdim-1 do begin
  for l=0, xdim-1 do begin
    perfil = where(lino_cor(l,*,k) GT 0.0001, CT)
    if CT NE 0 THEN BEGIN
      lino_cor[l,perfil[0],k]=0
      lino_cor[l,perfil[ct-1],k]=0
    ENDIF
  ENDFOR
ENDFOR

for k=0, zdim-1 do begin
  maxplano=MAX(lino_planar[*,*,k])
  if maxplano LT 60 THEN BEGIN
    for pos=0, acqpos-1 do begin
      lino_cor[*,*,k+pos*zdim]=0
    endfor
  endif
endfor

openw, 20, lino_cor_file + '.ima'
writeu, 20, lino_cor
close, 20

quasimakelog, OUTPUT = lino_cor_file, /ISLINO, ACQPOS = acqpos, $
DETECTDIST = detectdist, REBINNING = rebinning,$
X = 100, Y = 100, Z = 101*acqpos, $
DATATYPE = 'double', PARENT = base
duracao=sysitime(1)-time

print, 'duração=', duracao
END

```


A.2. – Random Correction

linorandomcor.pro

```

PRO linorandomcor, LINO_PROMPT_FILE = lino_prompt_file, LINO_RANDOM_FILE =
lino_random_file, LINO_COR_FILE = lino_cor_file, ACQPOS = acqpos, DETECTDIST = detectdist,
REBINNING = rebinning

time=systime(1)
close, /all

xdim = 100
ydim = 100
zdim = 101

lino_prompt =  dblarr(xdim, ydim, acqpos*zdim)
lino_random =  dblarr(xdim, ydim, acqpos*zdim)
lino_cor =      dblarr(xdim, ydim, acqpos*zdim)

openr, 20, lino_prompt_file
readu, 20, lino_prompt
close, 20

openr, 20, lino_random_file
readu, 20, lino_random
close, 20

lino_cor = lino_prompt - lino_random

ind = where(lino_cor LT 0.0, CT)
if CT NE 0 THEN BEGIN
    lino_cor[ind]=0
endif

openw, 20, lino_cor_file + '.ima'
writeu, 20, lino_cor
close, 20

quasimakelog, OUTPUT = lino_cor_file, /ISLINO, ACQPOS = acqpos, $
DETECTDIST = detectdist, REBINNING = rebinning, $
X = 100, Y = 100, Z = 101*acqpos, $
DATATYPE = 'double', PARENT = base

duracao=systime(1)-time
print, 'duracao=', duracao
END

```